Long-term fault slip rates, distributed deformation rates, and forecast of seismicity in the western United States from joint fitting of community geologic, geodetic, and stress-direction datasets

Peter Bird
Department of Earth and Space Sciences
University of California
Los Angeles, CA 90095-1567
pbird@ess.ucla.edu

ABSTRACT. The long-term-average velocity field of the western United States and adjacent offshore regions is computed with a kinematic finite-element code. Community datasets used include fault traces and geologic offset rates, geodetic velocities, principal stress directions, and Euler poles; each datum is qualified by a meaningful formal uncertainty. There is an irreducible minimum amount of distributed anelastic deformation, which accommodates 1/3 of Pacific-North America relative motion in California. Much of this is probably due to slip on faults not included in the model. All datasets are fit at a common RMS level of 1.8 datum standard deviations. Experiments with alternate weights, fault sets, and Euler poles define a suite of acceptable community models. In a pseudo-prospective test of these community models, fault offset rates are compared to 126 additional published rates not used in the computation: 44% are consistent; another 48% have discrepancies under 1 mm/a, and 8% have larger discrepancies indicating remaining problems. Updated models are then computed including these additional data. Novel predictions include: dextral slip at 2~3 mm/a in the Brothers fault zone, two alternative solutions for the Mendocino triple junction, slower slip on some trains of the San Andreas fault than in recent hazard models, and clockwise rotation of some small domains in the Eastern California shear zone and eastern Transverse Ranges. The preferred kinematic model is converted to a long-term seismicity forecast by assigning each fault and finite element the conversion parameters (coupled thickness, corner magnitude, and spectral slope) previously determined for the most comparable type of plate boundary. This long-term seismicity forecast is retrospectively compared to instrumental seismicity, which was not used in its construction. The western U.S. has been 50% below its long-term-average seismicity during 1977-2008, primarily because of (temporary) inactivity of the Cascadia subduction zone and San Andreas fault system.

1. Motivation

There are at least two reasons to pursue a unified kinematic model of ongoing deformation in each of the world's orogens: (1) Dynamic theory and modeling (which involve rheology, stress-equilibrium, and driving forces) will be more nearly correct when they develop from a good kinematic description of what is actually happening. (2) Any complete kinematic model can be converted to a long-term seismicity forecast, from which seismic hazard maps and seismic risk statistics can be computed for guidance of public policy and personal choices.

This paper contributes to both goals. By computing minimum rates of distributed anelastic deformation (between model fault traces), I will show that this distributed deformation accommodates a significant fraction of relative plate motion in California, and that kinematic or

dynamic models with purely-elastic microplates separated by a small number of plate-boundary faults are not appropriate. By converting the preferred model to a long-term seismicity forecast which is independent of historical seismicity, I highlight regions in which future seismicity will probably be greater than historical seismicity. A subsidiary goal is to illustrate a process for mapping of long-term seismicity which is rule-based, objective, and transparent, while providing a mechanism for frequent and inexpensive updates as new data become available.

2. Modeling Algorithms, Contrasted with Predecessors

The computational framework for this paper is a set of three codes, each of which has been presented previously with full mathematical detail. Here is a brief qualitative description of each, followed by some distinctions between each program and the methods used by other researchers.

2.1. Program Slippery

The computation of uncertainty in the long-term geologic offset rate from a single offset feature, and also the uncertainty in multi-feature combined offset rates for a particular fault train, is contained in program Slippery.f90 presented by *Bird* [2007], who included the source code in a digital appendix. Each offset distance is classified as one or more of 6 types, depending on the geometry of measurement: R (right-lateral trace-parallel heave), L (left-lateral trace-parallel heave), D (divergent trace-perpendicular heave), P (convergent trace-perpendicular heave), N (normal-sense throw), or T (thrust-sense throw). Oblique offsets are decomposed into two components and treated as two data. The uncertainty in the offset distance measured at the fault trace is represented by a probability density function (PDF) which is typically Gaussian (except in cases of upper and/or lower limits). Uncertainty in the far-field offset is increased by consideration of plausible changes in regional elastic strain, based on amounts of ground-breaking seismic slip which have been observed on other faults of the same type. The age of the offset feature is also represented by a PDF, which may have several different forms depending on whether the age is directly measured or bracketed, and on whether the dating method has problems of inheritance. The PDFs for offset distance and offset age are combined by an integral formula to obtain the PDF for the long-term (far-field) offset rate. From this PDF it is easy to select the median rate (at cumulative probability 0.5), and the lower and upper 95%-confidence limits (at cumulative probabilities of 0.025 and 0.975, respectively). The formal standard deviation is also computed, even though this PDF is not typically Gaussian.

Offset rates from individual offset features can be combined when they lie on the same fault train. (A fault train is a contiguous piece of the trace of a fault system along which our knowledge of fault geometry permits the null hypothesis of uniformity of one component of long-term offset rate.) First, the program estimates the chance that each individual rate is incorrect, unrepresentative, or inapplicable to neotectonics, using an empirical formula developed in *Bird* [2007]. Then, the PDFs of individual rates are combined by a formula which considers all weighted combinations of potentially-reliable rates to determine the PDF for the combined offset rate. Again, median rate and 95%-confidence limits are easily obtained from this PDF. The formal standard deviation is also computed, even though this PDF is not typically Gaussian.

While similar calculations involving PDFs have been made by a few authors in studies of single faults, most authors have been content to divide a lower limit on offset at the fault trace by

an upper limit on age (and vice versa) to obtain a range of rates for each offset feature. They have rarely considered the complication of plausible elastic strain changes in any systematic way.

Previous regional seismic hazard studies [*e.g., 2007 Working Group on California Earthquake Probabilities,* 2008; hereinafter abbreviated as *2007 WGCEP*, 2008] have typically decided fault slip rates by deliberation in a committee of experts. While the fastest (and most dangerous) faults received very careful consideration, many slow-moving faults have been assigned uncertainties by rule-of-thumb (*e.g.*, ±25% or ±50% of the selected offset rate), which are almost always too small. Also, these committees have considered additional factors such as kinematic compatibility, plate tectonics, geodetic velocities, paleoseismicity, and historical seismicity when choosing their preferred slip rates. For brevity, I will refer to these as "consensus composite rates." Consensus composite rates are not appropriate as inputs to NeoKinema (described below), in which these non-geologic factors are also considered and automatically balanced against offset rates which should be purely geologic (even if this leaves them highly uncertain).

2.2. Program NeoKinema

The merger of geologic offset rates, geodetic velocities, and principal stress directions to estimate the long-term velocity field is accomplished with kinematic finite-element code NeoKinema.f90, which was used by *Bird & Liu* [2007], *Liu & Bird* [2008], and *Rucker* [2008]. The equations underlying the program were developed in Supplemental Material S1 (sm001.pdf) of *Liu & Bird* [2008]. Source code was listed as their Supplemental Material S2 (sm002.zip), but note that this previously-published version (v.2.1, 2007.08.14) is no longer the latest, as described below.

The model domain is the area within a closed curve on the Earth's spherical surface. The domain is divided into many spherical-triangle finite-elements [*Kong & Bird*, 1995], with nodes at their corners (**Figure 1**). The degrees of freedom are two at each node: Southward component of long-term-average velocity, and Eastward component of long-term-average velocity. Therefore, differentiation of velocity within each triangle yields the long-term-average 2-D (horizontal plane) strain rate tensor, which is anelastic by definition. The remaining components of the 3-D anelastic strain rate tensor are derived from conservation of volume and verticality of one principal axis. It is not necessary to model vertical velocity components explicitly.

The general formalism for solving for nodal horizontal velocity components is to optimize a weighted-least-squares objective function by finding its stationary point in multi-dimensional velocity-component space with a system of linear equations. Nonlinearities are handled by iteration of the solution (typically 20 times). Velocity boundary conditions are usually applied all around the edges of the models, which should ideally lie within relatively rigid parts of the surrounding plates.

Geodetic benchmarks are treated as internal point constraints on the velocity field (with associated uncertainties). However, geodetic velocities are first "corrected" to remove local elastic bending due to temporary locking of the seismogenic portion of (most) faults, using the current model estimates of the fault slip rates, locking depths assigned *a priori*, and analytic solutions for rectangular dislocations in a uniform elastic half-space. This requires iteration.

Faults with positive target offset rates contribute to the target strain rates of all elements they cut through. Uncertainty in fault offset rate contributes to anisotropic compliance of all elements that a fault cuts through. An unlimited number of faults can cut through any element, as long as no node lies exactly on a fault trace. However, better accuracy is expected when fast-slipping faults are outlined by narrow quadrilaterals formed of pairs of elongated triangular elements (Fig. 1). Input fault offset rate components can be either heave rates or throw rates. Throw rates are converted into heave rates using assumed fault dips [Table 5 in *Bird & Kagan,* 2004]. All dip-slip faults are permitted to slip somewhat obliquely (but restrained by a control parameter) for more realistic flexibility of the fault network. This also requires iteration of the solution.

In elements with no mapped fault traces ("continuum elements") the horizontal principal directions of the long-term anelastic strain rate are constrained by horizontal principal stress directions, which are interpolated from data of the World Stress Map into every finite element by the clustered-data method of *Bird & Li* [1996]. Unfaulted elements also have a target strain-rate of zero, with an assigned uncertainty. This uncertainty [parameter μ of Appendix S1 of *Liu & Bird*, 2008] is obtained in bootstrap fashion by iteration of the entire solution.

The objective function of NeoKinema is a nondimensional functional of both dimensional model predictions (p) and corresponding dimensional data values (r), normalized by dimensional covariance matrix ($\tilde{C}$) or by individual datum standard deviations (σ):

$$\Pi \equiv -\left(\vec{p}-\vec{r}\right)^{\mathrm{T}}\left[\tilde{C}_{\mathrm{GPS}}^{-1}\right]\left(\vec{p}-\vec{r}\right)-\frac{1}{L_0}\sum_{m=1}^{M}\int_{\mathrm{length}}\frac{\left(p_m-r_m\right)^2}{\sigma_m^2}\mathrm{d}\ell-\frac{1}{A_0}\sum_{n=1}^{3}\iint_{\mathrm{area}}\frac{\left(p_n-r_n\right)^2}{\sigma_n^2}\mathrm{d}a \qquad (1)$$

where the first term is a quadratic form involving the great vector of all geodetic velocity components and its covariance matrix $\tilde{C}_{\mathrm{GPS}}$, the second term concerns the M long-term fault offset-rates r_m with their uncertainties σ_m, and the third term concerns the constraints on sizes and orientations of distributed anelastic deformation-rate tensors (in 2-D, with 3 independent components) in between the mapped faults. Note that this objective function gives a result that is (approximately) independent of the sizes of the finite elements into which the length and area integrals are subdivided.

This objective function includes two "tuning" parameters: (1) trace length for unit weight of long-term offset-rate data, L_0 ; and (2) area receiving unit weight in continuum stiffness and isotropy constraints, A_0. (Both are relative to constant unit weight of point-based geodetic data.) Adjustment of these two values controls the relative quality of the fits to geodetic data (best fit with large L_0 and large A_0), geologic data (best fit with small L_0 and large A_0), and continuum constraints (including both minimization of strain-rate and orientation of strain-rate; best fit with large L_0 and small A_0).

The quality of any particular model is described by 3 dimensionless misfit measures, each of which is a root-mean-square norm (N_2) of a vector of nondimensionalized misfits to data:

$$N_2^{\mathrm{geodetic}} \equiv \sqrt{\frac{1}{2B}\sum_{b=1}^{B}\left(\vec{p}_b-\vec{r}_b\right)^{\mathrm{T}}\left[\tilde{C}_b^{-1}\right]\left(\vec{p}_b-\vec{r}_b\right)} \qquad (2)$$

4

where B is the number of geodetic benchmarks and this error measure at each benchmark involves only the local (2×2) covariance of its 2 horizontal components $\tilde{C}_b$; and

$$N_2^{\text{stress}} \equiv \sqrt{\frac{1}{\sum a_i} \sum_{i=1}^{elements} a_i \left(\frac{p_i - r_i}{\sigma_i}\right)^2} \qquad (3)$$

where the a_i are the areas of the finite elements, and the predictions and data are both transformed versions of the azimuth of the most-compressive principal horizontal strain-rate. One important objective in modeling is to bring these measures below ~2, and as close as possible to 1. (Fits with $N_2 < 1$ could be considered overconstrained; there would be some risk of fitting the high-frequency noise in the data as well as its useful low-frequency signals.)

In previous projects we used a parallel measure of the misfit to long-term geologic offset rates, weighted only by trace-lengths (and inversely by datum variances). However, this measure gave potentially misleading results by suggesting a better fit than had actually been achieved. This is due to the very nonuniform populations of fault offset rates. Somewhat like earthquake moments in a seismic catalog, they span many orders of magnitude (*e.g.,* 4.6 orders, from 0.001 mm/a to 40 mm/a, in this project). Also like earthquakes, the small rates are far more numerous than the large rates, which occur on only a few first-order fault trains (San Andreas, Mendocino, Cascadia, *etc.*). Finally, there is a tendency for many datum standard deviations to be the same order-of-magnitude as the rate (at least for relatively well-constrained rates). A weighted-least-squares algorithm like NeoKinema will always fit those data best which have the smallest standard deviations. So, NeoKinema routinely matches with great precision all of those slow offset rates which also have small standard deviations. An inappropriate misfit measure can make this look like a successful fit to all offset rates, when in fact the fit to the rates of first-order faults may be unacceptable. After some experimentation, I programmed a better misfit measure in which, prior to the N_2 (RMS) norm operation, the dimensionless misfits are each weighted by the seismic potency rate of their associated fault. (Seismic potency rate is the product of seismogenic fault area and slip rate.) For stability of this measure, I use the greater of the model or datum slip-rate to determine this relative weight within the misfit measure. This new misfit measure is called the "potency" misfit:

$$N_2^{\text{potency}} \equiv \sqrt{\frac{1}{\sum\sum \ell_{im} w_m h_{im}^{\text{sup}}} \sum_{i=1}^{elements} \sum_{m=1}^{M} \ell_{im} w_m h_{im}^{\text{sup}} \left(\frac{p_{im} - r_m}{\sigma_m}\right)^2} \qquad (4)$$

where ℓ_{im} is the trace-length of fault m in element i, w_m is the down-dip width of the seismogenic portion of fault m, and h_{im}^{sup} is the greater of the model heave-rate or datum heave-rate. In practice, I find that criterion $N_2^{\text{geologic}} < 2$ implies a reasonably good fit to offset-rates on first-order faults as well as minor faults.

Many previous authors have presented other algorithms for estimating neotectonic velocities (either interseismic or long-term) from various mixtures of geologic (or consensus composite) fault offset rates and geodetic velocities. In **Table 1**, I present a comparison of this model to 12 other kinematic models of/within/including the western U.S. that have been published in the last 15 years. The competing code most similar to NeoKinema in its ability to incorporate diverse input data is that progressively developed by *Haines & Holt* [1993], *Haines*

et al. [1998], *Shen-Tu et al.* [1999] and *Flesch et al.* [2007]. However, their code does not provide posterior/output fault offset rates which have been adjusted from their prior/input values. Also, NeoKinema has the advantage over many other kinematic codes that it uses stress-direction information to constrain the model crustal flow outside of fault zones and increase its dynamic plausibility; this has the practical effect of permitting many small finite elements to be used for better spatial resolution of fault interactions.

The modeling of the western U.S. presented here is most similar to that of *Bird & Liu* [2007], who used a previous version of NeoKinema. The use of revised misfit measure (equation 4) is the primary change in the algorithm. Other differences in application are that I (1) incorporate faults in the southern Gorda region of the Juan de Fuca plate, and in the Rio Grande rift; (2) use new geologic and geodetic compilations with reliable uncertainties; and (3) perform more tests of model sensitivity to Euler poles, fault sets, weighting factors, and new data. These differences will each be developed in following sections of this paper.

2.3. Program Long_Term_Seismicity

Program Long_Term_Seismicity.f90 is a realization of the set of hypotheses known as the SHIFT model (an acronym for Seismic Hazard Inferred From Tectonics) [*Bird & Liu*, 2007]. The primary hypotheses are that: (1) The long-term seismic moment rate of any tectonic fault, or any large volume of anelastically deforming lithosphere, is approximately that computed using the coupled seismogenic thickness of the most comparable type of plate boundary. (2) The long-term epicenter production of any tectonic fault, or any large volume of anelastically deforming lithosphere, is approximately that computed from its moment rate using the frequency-magnitude distribution of the most comparable type of plate boundary. The seismicity coefficients (coupled seismogenic lithosphere thickness $\langle cz \rangle$, corner magnitude m_c, and asymptotic spectral slope β of the tapered Gutenberg-Richter frequency/magnitude relation) of each type of plate boundary were determined by *Bird & Kagan* [2004] and listed in their Table 5. Decision rules for assigning faults and finite elements to the "most comparable" type of plate boundary are contained in Tables 1 & 2 of *Bird & Liu* [2007].

The primary difference between this method and that of recent seismic hazard forecasts for California [*e.g., 2007 WGCEP,* 2008] and the western U.S. [*e.g., Frankel et al.,* 1996, 2002; *Petersen et al.,* 2008] is that I never assume that faults have either periodic or characteristic earthquakes, and I do not assume that earthquake magnitude is limited by mapped fault length or inferred fault area. Instead, I propose that (with low probability) an earthquake beginning on a short fault, or in an area between mapped faults, can grow to large size by linking up mapped faults and/or existing-but-unmapped faults, and occasionally by creating new fault area [*Black,* 2008]. The practical result of this difference in assumptions can be seen by comparing the RELM seismicity forecasts mapped by *Field* [2007], especially his Figures 3.1 and 3.2 compared to 3.9. Another difference is that my method does not use historical seismicity or inferred paleoseismicity of the region in any direct way. Recent seismicity is an important consideration in short-term forecasting, but I consider that seismic catalogs (whether historic or instrumental) are too short, and paleoseismic catalogs presently too incomplete, to provide a sound basis for long-term seismicity projections.

2.4. Availability of Codes

Source code for program Slippery was in *Bird* [2007]. Fortran 90 source codes for NeoKinema (v.2.2, 2008.01.30) and Long_Term_Seismicity are attached to this publication as supplemental materials: **NeoKinema.f90** and **Long_Term_Seismicity.f90**. All source codes used in this project are also available from the author at: http://peterbird.name, where one may also find useful accessory programs, including OrbWin for creation of 2-D spherical-Earth F-E grids, OrbNumber for renumbering nodes to reduce bandwith of linear systems, and either NeoKineMap or FiniteMap for graphical display of input and output datasets.

3. Community Datasets and Other Inputs

Most of the calculations presented in this paper are based on datasets created by others in long-standing collaborative groups, including the Working Group[s] on California Earthquake Probabilities, Southern California Earthquake Center, USGS National Seismic Hazard teams, Plate Boundary Observatory geodecists, and World Stress Map team. Therefore, they are referred to here as "community models" (although I retain responsibility for any errors in computation).

3.1. Traces of active and potentially-active faults

Traces of active and potentially-active faults in the western U.S. and adjacent offshore regions were compiled from 5 sources:

Fault traces in California (and its continental borderland) are from Fault Model 2.1 or 2.2 of the Working Group on California Earthquake Probabilities (**Figure 2**). As explained in *2007 WGCEP* [2008], these resulted from the merger of (1) the Community Fault Model [*Plesch et al.,* 2007] created by the Southern California Earthquake Center, with (2) traces in northern California adopted or created by *WGCEP* [2003]. Fault Models 2.1 and 2.2 are mutually exclusive alternatives which differ primarily in the shapes and topologies of certain fault traces in the southern margin of the Transverse Ranges, from the Santa Barbara Channel eastward to the Puente Hills of California. They have 243 and 248 traces, respectively. A community Internet application named SCEC-VDO (Southern California Earthquake Center-Virtual Display of Objects) may be used to display these faults in 3-D. The Fault Models contain estimated locking depth ranges, which in southern California are largely from *Nazareth & Hauksson* [2004]. (Consensus composite slip rates are also included in the Fault Models, but were not used in this project.) NeoKinema fault numbers (*e.g.*, "F4170", used in Table 4 and in the supplemental files attached to this paper) were assigned by adding 4000 to WGCEP fault numbers. Two faults which are common to both Fault Models have internally inconsistent data which make it unclear whether they were intended to be oblique-slip thrusts or purely strike-slip faults: the San Andreas (San Gorgonio Pass-Garnet Hill) train has dip of 58°NE and rake of 180°, while the Santa Rosa Island fault has dip of 90° and rake of 30°. In each case, I covered both possibilities by making the fault purely strike-slip in one model, and treating it as an oblique thrust in the other model.

Fault traces in other western states include all those used in computations for the 2002 National Seismic Hazard Maps [*Haller et al.,* 2002].

I included additional potentially-active faults outside California from my own compilation of the geologic literature [Table 1 of *Bird,* 2007], including faults with known

Neogene activity which lack documented overlap formations. This was based on the consideration that active faults of modest slip rate (*e.g.,* 0.1 mm/a) and typical slip-per-event (*e.g.,* 4 m) may have experienced last movement in the late Pleistocene (*e.g.*, 40 ka), but their scarps may have been obscured by later Pleistocene erosion and/or sedimentation. Many of these faults were identified by authors of regional survey papers about the Basin and Range province or the Rio Grande rift [*e.g., Stewart,* 1978, 1998; *Tweto*, 1979; *dePolo*, 1998], while others were identified during dissertation or other mapping projects reported in the literature. I digitized these additional traces from various sources including state geologic maps, online maps of the USGS Quaternary Fault and Fold Database, and large-scale maps in dissertations and journals. Where a normal fault has a mapped surface trace in Quaternary deposits along only part of a basin/range topographic scarp, I typically assumed that an underlying fault extends along the entire scarp. Likewise, I often combined groups of minor faults into a single "fault system" trace, appropriate for small-scale modeling, where the gaps are small enough to be jumped by earthquake ruptures [*Wesnousky*, 2006; *Black*, 2008]. Faults of less than 10 km length which could not be integrated with other nearby traces into a longer fault system were not included.

Traces of the Cascadia subduction zone and the speading centers and transform faults along the Gorda Ridge are from the PB2002 plate boundary model of *Bird* [2003].

The 545 fault traces within the Gorda orogen part of the Juan de Fuca plate are from *Chaytor et al.* [2004], who mapped them using high-resolution swath bathymetry and seismic reflection profiling. These are a combination of reactivated normal faults originally created at the Gorda Rise, and newer faults which cross-cut the seafloor-spreading fabric. Faults of ambiguous slip were assumed to be left-lateral.

All of these 1479 traces (Figure 2) are contained in file **fGCN_merged_WGCEPFM2p2_200810.dig** which is part of the supplemental material for this paper. The NeoKinema convention is that fault traces are digitized left-to-right when looking in the downdip direction; vertical strike-slip faults are typically digitized from NW to SE or from SW to NE, but there are some exceptions.

3.2. Long-term geologic offset rates on faults

One distinguishing feature of this model is that it uses no consensus composite slip rates for faults on land, but only geologic offset rates based on dated offset geologic features. The computation of the probability density function (PDF) for the combined long-term offset rate of any fault train with program Slippery.f90 was described briefly in section 2.1, and fully in *Bird* [2007].

The offset rates and uncertainties input to NeoKinema are the median rate and the formal standard deviation, respectively, from the combined-rate lines of Tables 1 and 2 of *Bird* [2007]. Rates for California fault trains come from Table 2, which was based on the PaleoSites database addition to the USGS Quaternary Fault and Fold Database, created through the efforts of the Working Group on California Earthquake Probabilities. While this database is not yet available on-line, it has been reviewed by 3 WGCEP members, as well as by the author and a coworker. Rates for faults in other western states come from Table 1 of *Bird* [2007], which was based on the author's personal compilation from the literature. This was reviewed only during the publication process, and the chances of errors and omissions are correspondingly higher.

The total number of geologic offset rates is 572, while the number of fault trains in the model is 1479. Fortunately, NeoKinema is able to work with faults that have very uncertain rates, and to estimate their rates from the merger of geodetic, plate-tectonic, stress-orientation, and strain-compatibility considerations. In order for this to work properly, the faults with no documented offset features should be assigned large uncertainties in offset rates, with some rational basis. Such faults are here assigned a generic rate PDF, median rate, and (large) standard deviation based on the composite PDF for all faults of that type (R, L, N, D, T, or P) in the western U.S. which do have dated offset features. For example, a normal fault (N) with no offset datum is assigned a median throw rate of 0.183 mm/a with a standard deviation of 0.343 mm/a. A right-lateral strike-slip fault (R) with no offset datum is assigned a median heave rate of 6.18 mm/a with a standard deviation of 12.6 mm/a. These large uncertainties permit the fault to slip much faster or slower than the nominal rate, to remain locked, or even to slip in the opposite sense from the nominal rate.

In most parts of the NeoKinema calculation it is not important whether a fault slips seismically or aseismically. However, this makes a difference when correcting geodetic velocities of benchmarks near a fault for temporary fault locking, as no correction is needed for faults which creep steadily. In the input data file, certain California faults are designated as creeping by a logical flag: Calaveras (Central, South), Concord, Green Valley (North, South), Hayward (North, South), Hunting Creek-Berryessa, Maacama-Garberville, and San Andreas (creeping segment). It is not known whether other faults outside California might also be creeping, but the distinction is less important when the heave rate of the fault is comparable to or less than the uncertainty in GPS velocity.

Target rates and uncertainties for spreading segments (offsets of type D) and adjacent transforms (offsets of type L, R) on the Gorda Ridge are from magnetic anomaly bands, according to the data compilation of *DeMets et al.* [1990], corrected for the magnetic timescale revision of *DeMets et al.* [1994], and interpolated where necessary using latitude as the independent variable. The Cascadia subduction zone (the only offset of type S) is assigned a nominal rate of 39.5 mm/a [*Bird*, 2003] with a relatively large standard deviation of 7.5 mm/a to allow for unknown amounts of deformation in the overriding lithosphere.

Faults in the oceanic lithosphere of the Gorda orogen [*Chaytor et al.*, 2004] are probably a distinct population from continental normal and transform faults, with different distribution(s) of rates. Unfortunately, only a single offset has been identified: a long sinistral fault has known minimum slip rate of (1.5~1.7 km)/(<2 Ma), implying a minimum rate of (0.75~0.85) mm/a. There is not enough information to employ program Slippery. Rather arbitrarily, I reduced the multiple activity classes of *Chaytor et al.* to only two: "active fault" with target rate of 0 mm/a and standard deviation of 1 mm/a, and "potentially-active fault" with target rate of 0 mm/a and standard deviation of 0.3 mm/a. Given this great uncertainty, it would be very valuable to obtain selected seafloor velocities by geodetic means within the Gorda orogen.

All 1536 offset rates with their uncertainties are compiled in file **fGCN_merged_WGCEPFM2p2_200810.nki** which is part of the supplemental material for this paper. The number of rate entries is greater than the number of fault trains because some fault trains are known to have oblique slip, which is described by a strike-slip entry (offset type L or R) plus a separate dip-slip entry (N or D for extension; alternatively T or P for shortening).

9

3.3. Interseismic velocities of benchmarks from GPS

Velocities of benchmarks in California are from a new combined solution of GPS data completed by Zhengkang Shen, Bob King, Min Wang, and Duncan Agnew in June 2006 for the Working Group on California Earthquake Probabilities. A preliminary (November 2005) version of this solution is available from the WGCEP site at: http://wgcep.org/. It is a statewide solution based on analysis of the original data (SCEC and Berkeley reprocessed regional survey mode daily solutions, and SOPAC processing of the continuous sites), rather than adjustments of other investigators' velocity fields. Coseismic effects of the Joshua Tree, Landers, Northridge, Hector Mine, and San Simeon earthquakes have been estimated and excluded from the velocity modeling. Data showing immediate short-term (a few months to a year or so) postseismic deformation were also excluded. This solution includes 1226 benchmarks and a covariance matrix.

To provide coverage of other western states, I used the Plate Boundary Observatory joint GPS solution of 2007.09.19 from http://pboweb.unavco.org/. This is the network velocity field derived from final combined solutions generated by the Analysis Center Coordinator at MIT. Only individual-site uncertainty ellipses are available for this solution. I selected sites from this model in four steps: (1) deletion of stations with velocity standard deviations exceeding 3 mm/a (which eliminates most stations with short occupation history and/or nonlinear movement history); (2) deletion of all benchmarks in Yellowstone National Park, which may be affected by magma chamber deflation; (3) deletion of 3 benchmarks (P075 in NV, P683 in ID, P692 in OR) which have anomalous velocities suggesting possible fault-creep or non-tectonic processes; and (4) deletion of all benchmarks in California, which is already covered by the WGCEP solution described above. This left 307 benchmarks, 193 of which are within the domain of the NeoKinema model.

This composite GPS velocity field of 1419 benchmarks is plotted in **Figure 3**. Both component solutions are expressed in the reference frame of stable (eastern) North America. Certainly there must have been small procedural differences in the definitions of this reference frame by the two groups of geodecists, and this could result in artificial velocity shear across the inland borders of California. However, no discontinuities are apparent (except across active faults of the Walker Lane), and it is likely that any such discrepancy is less than 1 mm/a.

Before using this velocity field in NeoKinema, all benchmarks located less than 2 km from faults with slip rates over 1 mm/a were deleted, because at smaller distances F-E grid GCN8p9.feg interpolates and smears the fault discontinuities in long-term velocity, making it erroneous to compare grid velocity with corrected (long-term) geodetic velocity. This editing step removed 212 or 209 benchmarks, depending on whether WGCEP Fault Model 2.1 or 2.2 was used. Thus, 1207 or 1210 benchmarks were actually used in each NeoKinema solution.

3.4. Most-compressive horizontal stress azimuths

For study of *Bird & Liu* [2007], most-compressive horizontal principal stress directions were downloaded from the World Stress Map Project [*Reinecker et al.*, 2004]. About 963 data fell inside the Gorda-California-Nevada orogen, and an additional 1105 data were outside its margins but close enough (<22° of great-circle arc) to be used for the interpolation of principal stress directions. The same dataset is used here. The NeoKinema input file **s_Gorda-Cal-Nev.nki** is part of the supplemental information attached to this paper.

The uncertainties reported by WSM for each azimuth are highly generalized and somewhat arbitrary. Each datum has a letter-coded quality class, and approximate angular uncertainties are stated for each quality class for each type of data. However, it is unclear whether these numerical values are standard deviations, 95%-confidence limits, or absolute limits. Also, the rounding of these values suggests that they may be subjective estimates rather than results of statistical studies. Therefore, the uncertainties from WSM were not used. Instead, NeoKinema interpolates stress direction to the center of each finite element, using the clustered-data algorithm of *Bird & Li* [1996] which provides individual uncertainties for each result which are based on the scatter in surrounding azimuths. Standard deviations range from 2.7° to 49.4°, with median of 8.5°. Both original and interpolated stress directions are shown in **Figure 4**.

3.5. Boundary conditions

Velocity boundary conditions may be imposed around the margins of a NeoKinema simulation, and this is highly desirable as a way of enforcing both the rigidity of the surrounding plates and the correct net relative velocity across the model domain. Because F-E grid GCN8p9.feg (Figure 1) spans the entire Gorda-California-Nevada orogen and Rio Grande rift, it is surrounded by relatively rigid portions of the North America (NA), Pacific (PA), and Juan de Fuca (JF) plates. I take stable NA as the velocity reference frame. Then, only neotectonic Euler poles for NA-PA and JF-PA are required to compute boundary velocities.

The neotectonic Euler pole for NA-PA is uncertain and controversial, as shown in **Figure 5**. (All of these NA-PA Euler poles are detailed in **Table 2**.) The NUVEL-1A pole of *DeMets et al.* [1994] came from a global solution for the poles of the 12 largest plates, based on marine magnetic anomalies 2A, transform fault azimuths, and seismic slip vectors. The other poles shown are geodetic, and unfortunately none of them took the NUVEL data set into consideration. The quality of a purely-geodetic pole depends upon: (1) length of observation; (2) technical issues concerning reference frame and data reduction; and (3) number and locations of sites which represent each plate. Length-of-observation is obviously better for the poles published more recently. On the other hand, *Argus* [2007] raised an important criticism of conventional plate-motion solutions based on ITRF2000 or (especially) ITRF2005 because these reference frames drift with respect to the global shell of lithosphere. When a poleward-drifting reference frame is used to extract horizontal velocity components for Euler-pole calculations, an equatorial belt of anomalous velocity is introduced which will contaminate NA-PA poles in particular. This concern was recently addressed by *Kogan & Steblov* [2008] with their "plate-frame" pole. An additional consideration is that the only geodetic pole to represent PA by benchmarks on Guadalupe Island and Baja California (Figure 3) is that of *Gonzalez-Garcia et al.* [2003]. Thus, this pole may be superior for representing the motion of the nearest parts of the Pacific plate, even if the *Kogan & Steblov* pole is a more accurate representation of the motion of the distant parts of the Pacific plate.

The JF-PA Euler pole used (35°N, 26°E, 0.5068 degree/m.y.) is from *Wilson* [1988]. It is based directly on magnetic anomaly bands along the Juan de Fuca Ridge, and is relatively certain. The Sierra Nevada/Great Valley plate of *Argus & Gordon* [2001] is entirely included within the model domain (Figure 1) and so does not require boundary conditions.

3.6. Fixed parameters

Certain additional parameters read as input by NeoKinema were fixed throughout this modeling project. Each solution was iterated 20 times, which typically resulted in overall relative velocity changes of 0.03% and maximum velocity changes of ~0.1 mm/a in the last iteration. Parameter xi_ (ξ), a small strain-rate quantum used in the code to prevent singularities, was fixed at 3.2×10^{-17} /s based on previous experience. The standard deviation of slip rake for dip-slip faults (around the nominal target of $\pm 90°$) was 20°. The shallower and deeper interseismic locking depth limits for faults outside California were 1 and 12 km, respectively, except in the Cascadia subduction zone where they were 14 and 40 km [*Bird & Kagan*, 2004]. All optional program features were switched off.

4. High Rates of Distributed Anelastic Deformation

Distributed deformation is defined here as that part of the field of strain-rate tensors in a NeoKinema solution which is not due to slip on modeled faults. It is anelastic by definition because NeoKinema solves for long-term-average (10^4- to 10^6-year) velocities, and cyclical variations in elastic strain average to insignificant rates over many earthquake cycles. In the weighted-least-squares algorithm of NeoKinema, distributed deformation rate is treated as an undesirable error and minimized. However, solutions with real data show a recalcitrant residual which cannot be eliminated. For plotting, tabulation, and discussion it is convenient to convert strain-rate tensors to scalars; for consistency with the objective function of NeoKinema, I use the azimuthally-invariant scalar measure:

$$\dot{e} \equiv \sqrt{\dot{\varepsilon}_{NS}^2 + \dot{\varepsilon}_{NS}\dot{\varepsilon}_{EW} + \dot{\varepsilon}_{EW}^2 + \dot{\varepsilon}_{NE}^2} \tag{5}$$

which in strike-slip regimes ($\dot{\varepsilon}_{NS} + \dot{\varepsilon}_{EW} = 0$) is equal to the greatest horizontal principal strain rate, or the shear strain rate in fault-parallel coordinates. Spatial variations of scalar $\dot{e}$ are mapped in **Figure 6**. It can be further characterized by its area-weighted RMS value, μ^*.

Because NeoKinema only computes a model of the surface velocity field, it is unclear how deep this distributed deformation extends. However, the current paradigm for continental tectonics is that the seismogenic layer is bounded by a brittle/ductile transition, below which distributed deformation by climb-assisted steady-state dislocation creep is widespread. Thus, we may say that the "problem" or "innovation" of distributed anelastic deformation is primarily notable in the seismogenic layer, extending to perhaps 12 km depth. In the following subsections I will discuss why shallow distributed deformation must exist, what strain mechanisms might be involved, how its intensity is constrained by this study, and what this implies for future kinematic and dynamic modeling.

4.1. Arguments and observations concerning distributed deformation

If all crustal blocks were completely outlined by faults, including transform faults conforming to arcs of small circles about Euler poles, there would still be some distributed deformation in the regions surrounding unstable triple-junctions [*McKenzie & Morgan*, 1969]. Actual distributed deformation in continents must be greater because many faults simply end where their slip goes to zero. In the Basin and Range province it is often possible to estimate the (minimum) throw on normal faults from the height of their topographic scarps, and it is common to see that throw taper to zero at fault ends, which do not connect to transform faults as plate

theory predicts. Some strike-slip faults (which are mapped in the plane of motion) also end without connections; examples in WGCEP Fault Model 2.1 include the Hosgri (Extension), Ortigalita, Greenville (South), Santa Ynez, Ludlow, Earthquake Valley, and Owens Valley faults. (This list does not include cases of aligned but widely-separated faults where a buried connection is debatable.)

Another kind of evidence for distributed deformation is the well-known discrepancy between (higher) geodetic rates of dextral strain and (lower) geologic rates of dextral strain based on measured fault slip rates in the Eastern California shear zone [*Oskin et al.*, 2007]. (In this case time-dependence of regional deformation has been proposed as an alternative explanation, but no physical mechanism for time-dependence has been modeled.)

There is also a theoretical dynamical argument for distributed deformation, based on the rheologic layering of the lithosphere: A brittle/ductile transition at midcrustal depth can only be maintained if the ductile layer has a non-zero anelastic strain rate to give it strength; without distributed deformation the ductile layer would undergo viscoelastic relaxation, transferring deviatoric stress upward into a thinning brittle layer until this would eventually break [*Roy & Royden*, 2000]. Thus, even a plate with a shallow frictional layer cannot sustain deviatoric stress for a million years if its regional strain-rate is zero.

A few mesoscale investigations have identified shallow distributed deformation in favorable circumstances, especially in close proximity to major faults. *Salyards et al.* [1992] used paleomagnetic declinations to estimate distributed deformation in marsh deposits around the San Andreas fault at Pallet Creek; off-fault deformation was 3 times greater than fault slip. (However, this is usually considered a special circumstance specific to marshy paleoseismic sites.) *Unruh & Lettis* [1998] studied seismogenic transpressional deformation east of the Hayward fault, where local fold-and-thrust belts are proposed to shorten at several mm/a. *Flodin & Aydin* [2004] studied distributed deformation of the Aztec Sandstone by strike-slip faults in Valley of Fire State Park, Nevada where they identified 5 hierarchical generations of structures in outcrop. *Oskin et al.* [2007] used the inactive Silver Bell normal fault as a strain marker in the belt surrounding the active Calico dextral fault, and found distributed deformation within 500 m of the Calico trace which was ~23% of total offset. One possibility is that distributed deformation is rare, and these sites have been described because they are exceptional. Another is that distributed deformation is common, but is not typically so visible in outcrops. This would depend on whether distributed deformation is typically accomplished by faulting, or by true continuum deformation.

4.2. Strain mechanisms of distributed deformation

At least 5 different strain mechanisms might contribute to distributed anelastic deformation at shallow depths. (1) Silicate crystals accommodate small amounts of strain by primary transient creep ("cold work"), which is nonequilibrium dislocation glide ending in tangles unrelieved by climb [*Poirier*, 1985]. This kind of strain occurs at a declining rate following the first imposition of deviatoric stress, but due to "work hardening" it is much less in subsequent loading cycles. (2) Rocks whose dominant minerals are stable below the water table (quartz, calcite) can deform by solution transfer ("pressure solution"), as is commonly seen in folded sedimentary rocks [*Gratz,* 1991]. (3) Rocks whose dominant minerals are not stable (mafic rocks) can deform by an analogous but non-steady weathering process, in which stressed grains and grain corners are preferentially weathered to create unstressed clays. (4) Tensile

microcracking which is due to differential expansion of different minerals (and differently-oriented crystals of the same mineral) during erosional unloading [*Bruner,* 1984] can have a preferred orientation where there is also a regional deviatoric stress of tectonic origin [*Boness & Zoback,* 2006]. (5) Distributed deformation can occur by frictional sliding on many faults of small net offset which have not been included in the NeoKinema model.

A critical distinction is that mechanisms (1)-(4) would be practically aseismic, while mechanism (5) would produce damaging earthquakes (although at low rates). The best available double-difference relocations of California earthquakes [*Hauksson & Shearer*, 2005] continue to show that many earthquakes cannot be located on any of the faults of the Community Fault Model. Therefore, it is prudent to base seismic hazard estimates on the hypothesis that slip on unmodeled faults is the dominant mode of distributed deformation. There is an analogy between quasi-fractal fault networks and the power-law distribution of earthquake moments, in both of which the majority of strain is due to first-order features, but all scales make some contribution. The faults modeled in this paper are simplified from primary observations recorded on geologic maps, and quadrangle-scale geologic maps rarely represent more than a fraction of the faults actually present in the field. In this light, the quantity μ^* can be considered an artifact of our limited progress in mapping and modeling, rather than a fundamental physical property of the crust. (However, it is likely to be a practical reality in modeling for centuries to come.)

4.3. Constraining minimum μ^* with NeoKinema

NeoKinema models are best computed in sets, because it is necessary to find the optimal values for 3 critical input parameters: L_0, A_0, and μ. The first two should be adjusted to find acceptable fits to geologic, geodetic, and stress-direction data simultaneously, as described in section 2.2. Meanwhile, an input/prior value of μ (the model parameter) must be found which will produce a similar output/posterior value of μ^* (the computed RMS rate of scalar distributed deformation $\dot{e}$ in that model). Fortunately, experience shows that there is a neighborhood around the optimum point in 3-D parameter space where μ^* is relatively insensitive to these 3 inputs.

The reconnaissance models described here were performed without using the full covariance matrix of the geodetic velocities in California; only the block-diagonal part (individual site error ellipses) was used. This reduced run times from 36 hours to 75 minutes each. Fault Model 2.1 and the NUVEL-1A pole for NA-PA were used throughout this set.

Having previously determined that $\mu^* \cong 5 \times 10^{-16}$ s by trial-and-error, I ran a systematic set of 45 models in which $\mu = 5 \times 10^{-16}$ /s was fixed, while L_0 was increased from 1250 to 320000 m by factor-of-2 steps, and A_0 was increased 2×10^8 to 32×10^8 m^2 by factor-of-2 steps (**Table 3**). Inside this rectangle in 2-D parameter space, an elliptical region was found (**Figure 7**) in which 10 models had acceptable misfit measures of $N_2^{\text{geodetic}} < 2$, $N_2^{\text{potency}} < 2$, and $N_2^{\text{stress}} < 2$ simultaneously. **Figure 8** shows resulting μ^* values with contours: there is a flat region with minimum $\mu^* > 5 \times 10^{-16}$ /s in the lower right, and 4 acceptable models have μ^* below 6×10^{-16} /s.

Slicing in the orthogonal direction through parameter space, **Figure 9** and Table 3 show results of 8 more models in which weights (L_0=4×10^4 m, A_0=4×10^8 m^2) were fixed while prior/input μ was varied. First, it is clear that posterior/output $\mu*$ is only weakly dependent on μ, so that 5×10^{-16} /s is the only value that gives consistency of prior with posterior. Second, we see that even if we abandon consistency and try to force less distributed deformation, all 3 misfit scores quickly rise to unacceptable values because of the increased rigidity of the model. For this geographic region, with these input data, there are no successful models with $\mu*$ below 5×10^{-16} /s.

4.4. Implications for kinematic and dynamic modeling

To put this amount of distributed deformation in perspective, I used the preferred model from this project (GCN2008088, discussed below) to create a budget for right-lateral deformation along the San Andreas plate boundary. The PA-NA transform plate boundary stretches 1350 km in this model, from the Mendocino triple junction (124.41°W, 40.26°N) to the northwestern Gulf of California (114.21°W, 31.35°N). According to the Guadalupe pole for NA-PA (Table 2), the mean velocity along this boundary is 47.8 km/m.y.. The product of these numbers is 64530 (km)^2/m.y.. However, the line integral of dextral slip rates on dextral and dextral-oblique (offset type R) faults in the model, to the southeast of the Mendocino triple junction, is only 43235 (km)^2/m.y., or 67% of this. I also computed the area-integral of twice the dextral strike-slip distributed strain-rate on vertical planes trending N38°W, also to the SE of the Mendocino triple-junction: the result was 21940 (km)^2/m.y., or 34% of the total. Thus, slip on mapped faults takes up 2/3 of PA-NA relative motion in the latitudes of the San Andreas fault system, while distributed deformation takes 1/3. (Clockwise rotation does not seem to play a significant part when averaged across the state of California, although it is locally important as discussed below.)

Interpretations of geodetic velocities have traditionally assumed purely-elastic microplates in the seismogenic depth range (although they vary according to the rheologies and layering assumed at greater depth). Since this assumed shallow structure can be described by 2 parameters per fault (slip rate and locking depth) it is relatively easy to determine both by inversion. Now I propose that many fault-crossing profiles are also sampling significant amounts of either distributed anelastic deformation (if it is aseismic and steady in time) or elastic straining preparatory to future distributed anelastic deformation (if it is unsteady). Since NeoKinema models (*e.g.*, Figure 6) predict that distributed deformation is often concentrated near major faults, it may be quite difficult to distinguish between these models using geodetic velocities alone. One prediction of this new model is that, on average, inversions of geodetic velocities using elastic microplates have tended to overestimate locking depths; this can be determined in subsequent earthquakes, although postseismic deep creep is a confusing factor. Another approach is to continue collecting and refining geologic offset rates, to see if traditional inversions of geodetic data have tended to overstate the slip rates of the dominant faults, as I expect. Perhaps it will even be possible to directly invert for the fraction of distributed deformation where its spatial distribution can be independently constrained. For this purpose, histograms of well-located seismicity (averaged along a fault, and plotted in cross-section) might serve as a reasonable proxy.

This finding also has important implications for dynamic modeling. If fault systems are quasi-fractal, and only ~2/3 of long-term-average deformation is accomodated on those master faults included in community models, then dynamic models which use purely-elastic microplates cannot be expected to succeed. It will be necessary to use crustal blocks which are plastic or frictional, and to make the rheologies of fault zones and inter-fault blocks as similar as possible. Dynamic finite element programs like Shells [*Bird,* 1999] take this approach, keeping dislocation-creep rheology laterally uniform, and merely distinguishing the fault from the rest of the crust by a lower effective coefficient of friction. Much work will be needed to come to an understanding of why and how effective friction drops as crust is progressively deformed (or whether some other kind of unified rheology is more appropriate).

5. Experiments with Euler Poles, Fault Models, and Geodetic Covariance

Details of the 53 models described in Section 4.3 (Figures 7~9) are presented in Table 3. They all used the NUVEL-1A Euler pole for NA-PA relative rotation and WGCEP Fault Model 2.1 in California. The best model in the group was GCN2008028, with misfits of :
$N_2^{\text{geodetic}} = 1.730$, $N_2^{\text{potency}} = 1.523$, and $N_2^{\text{stress}} = 1.746$; its overall misfit level is rated as:
$$\sup\left(N_2^{\text{geodetic}}, N_2^{\text{potency}}, N_2^{\text{stress}}\right) = 1.746.$$

The NUVEL-1A pole gives the highest velocity azimuth for stable NA with respect to stable PA when computed at Palmdale, CA (Table 2); that is, it gives the most transpressional model. In models GCN2008-053~057 and -094, I investigated the results of recomputing the boundary conditions using each of 5 published geodetic poles: ITRF2000, PA_GPS, Guadalupe, ITRF2005, and Plate_frame. The comparison of NUVEL-1A with Plate_frame is especially interesting because they span the range from most transpressional to most transtensional model; the range of azimuths for relative plate velocity is 4°. They are also the "slowest" and "fastest" of the poles modeled in terms of their predictions at Palmdale: the range is 45.7~50.4 mm/a.

By differencing output files from these two extreme models and plotting differential velocity, I found that the changes are mostly offshore. This is natural, as velocities on land are strongly constrained by GPS velocities which are relative to stable eastern NA. Therefore, the Plate_frame pole gave about 4.7 mm/a of additional dextral shear along the length of the borderland, and about 3.3 mm/a more compression perpendicular to the borderland. We have very little offshore data that is relevant to choosing between these models. However, there were slight variations in on-land velocities in 4 regions: Point Arena, San Francisco peninsula, Salinia terrane, and the southern tip of the model domain in northern Baja California. The Plate_frame pole causes the San Andreas (North Coast) dextral rate to increase from 14.7 to 17.5 mm/a, coming closer to its geologic target rate. The San Andreas (Peninsula) dextral rate increases from 14.5 to 17.3 mm/a, increasing its overrate error. The San Andreas (Santa Cruz Mt.) dextral rate increases from 17.7 to 19.6 mm/a, but is still well below its geologic target. The dextral rate on the Rinconada fault increases from 0.05 to 2.8 mm/a. The San Gregorio (North & South) dextral rates also increase by 1.5~2 mm/a. All other rate changes on faults for which we have geologic constraints are less than 1 mm/a.

The effect of the Euler pole on overall model misfit is very modest, and occurs by changing N_2^{stress} which is uniformly the highest misfit in this set of 6 models. The best result (Table 3) is not for either NUVEL-1A or Plate_frame but for the "compromise" Guadalupe pole which lies between them (Figure 5). As mentioned above, this pole is also the only geodetic pole

to incorporate Pacific-plate sites closer to California than Hawaii. For both reasons, the Guadalupe pole of *Gonzalez-Garcia et al.* [2003] was selected as the best for use in this modeling project, and employed in most of the subsequent calculations.

The next experiment was to keep all input parameters constant, and retain the Guadalupe pole, but to use WGCEP Fault Model 2.2 in southern California (GCN2008056 *vs.* -055 in Table 3). Right slip on the San Andreas (San Gorgonio Pass-Garnet Hill) train dropped from 11.1 to 5 mm/a when its throw rate was reduced from 0.6 to 0 mm/a by treating it as a purely strike-slip fault (see section 3.1 above). Right slip on the Mission Creek train increased from -0.05 to 2.2 mm/a in partial compensation. Right slip on the adjacent San Andreas (Coachella) train decreased from 16.6 to 15.2 mm/a. Right slip on the Brawley seismic zone dropped from 12.8 to 8.2 mm/a due to its modified shape. Right slip on the Imperial fault dropped from 24.6 to 18.6 mm/a, presumably due to the modified Brawley seismic zone. Left slip on the Malibu Coast fault increased from 2.1 to 3.2 mm/a due to its new trace. Left-transpressional faulting in the Santa Barbara Channel region was reorganized, and implausible extensional slip on two thrust faults in Fault Model 2.1 was eliminated. Most other changes in slip rate were either under 1 mm/a, or occurred on faults which are only present in one of the Fault Models. The effect on misfit measures was mixed, with N_2^{stress} going down slightly and the other two measures rising slightly.

The next innovation was to use the full covariance matrix of the California GPS velocities, which increases NeoKinema run times greatly. Using Fault Model 2.2 and the Guadalupe pole, I computed 18 models with varying L_0 and A_0, while fixing μ at 5×10^{-16} /s. Results in **Figure 10** and Table 3 show the same pattern as in Figure 7, only slightly offset in parameter space. Seven of these models were successful according to the criterion, $\sup\left(N_2^{\mathrm{geodetic}}, N_2^{\mathrm{potency}}, N_2^{\mathrm{stress}}\right) < 2$.

Then another 6 models (GCN2008077~081, Table 3) tested all combinations of the two Fault Models with the NUVEL-1A, Guadalupe, and Plate_frame poles. Neither model with the Plate_frame pole succeeded, because their geodetic misfits N_2^{geodetic} rose to 2.1~2.2. Lastly, 6 more models (GCN2008-082~087, Table 3) repeated all the models that had succeeded using the Guadalupe pole and Fault Model 2.2, but now using Fault Model 2.1.

This concludes the set of models which I refer to as the "community" models because of the origins of their input data. By testing various combinations of Fault Models, Euler poles, and NeoKinema weighting parameters, a suite of 16 "acceptable community models" has been found (counting only the latter computations using the full geodetic covariance within California). This provides a good estimate of the ranges of fault offset rates which might be obtained while still fitting all of the community input data reasonably well.

6. Pseudo-prospective Tests, and Updated Models

A true prospective test of these models will require collection of new geologic, geodetic, and/or stress-direction data following publication of this paper. However, there is an opportunity to conduct a pseudo-prospective test immediately by examining the prediction of data already published but not used in the computation.

By surveying major journals through October 2008, I located 54 additional papers giving 126 "new" offset rates on 68 fault trains in the western U.S. (beyond those tabulated by *Bird* [2007] and used in the community models). All are detailed in **Table 4**. The column "Community model predictions" gives the range of long-term offset rates predicted by the set of 16 acceptable community models just described. The columns "New geologic offset rate: Min., Max." give the 95%-confidence limits on long-term fault offset rate obtained by running the new datum through program Slippery.f90 (as described in section 2.1 above) as an individual offset feature. New rates are plotted against predictions in **Figure 11**.

The best results among these 126 pseudo-prospective tests were the 44% which showed no discrepancy. In these cases there was some overlap between the 95%-confidence bounds on the new offset rate (as computed by Slippery.f90 considering only the single offset feature) and the range of predictions among the 16 acceptable community models. For example, 2 new provisional dextral rates on the San Andreas (Mojave S) train of 5.9~18.5 and 11~57 mm/a from *Weldon et al.* [2008] overlap the 16.2~17.4 mm/a range of model predictions.   On the same fault train, the new rate of 16~29.5 mm/a based on alluvial fan #3 of *Matmon et al.* [2005] has no discrepancy (but their rates based on other fans do, as described below). On the San Andreas (San Bernardino N) train one provisional new rate of 7.2~20 mm/a from *McGill et al.* [2008] overlaps the model range of 18.9~20.6 mm/a. On the adjacent San Andreas (San Bernardino S) train, another provisional new rate from *McGill et al.* [2008] of 8.1~21.7 mm/a includes the model range of 11.6~15.4 mm/a. On the San Andreas (Coachella) train, the new dextral rate of 12~16.4 mm/a from *Behr et al.* [2008] overlaps the community model predictions of 14.8~17.5 mm/a. Off the San Andreas system, there were some cases where the NeoKinema community models "predicted" the offset rates of faults even in the absence of any offset geologic features to constrain their rates: right slip on the Owens Valley dextral/normal fault was predicted to be 1.44~2.18 mm/a, and is actually estimated as 0.63~5.3 mm/a [*Lee et al.*, 2001b]. Convergent heave on the Compton blind thrust was predicted as 0.85~1.56 mm/a, and is actually estimated as 1.3~2.7 mm/a [*Dooling et al.*, 2008]. (This is an incomplete list; see Table 4 for other cases.)

Another 48% of these pseudo-prospective tests resulted in "small" discrepancies of less than 1 mm/a. Another new provisional dextral rate of 13~18 mm/a on the San Andreas (San Bernardino N) train [*McGill et al.*, 2008] is slightly discrepant with the model prediction range of 18.9~20.6 mm/a. Admittedly, there are many cases where the same discrepancy would be "large" if stated as a percentage. For example, the model predictions of 0.18~0.23 for normal throw rate on the Carson Range normal fault miss the new geologic rate of 0.88~15 mm/a [*Ramelli et al.*, 1999] by a discrepancy of only 0.65 mm/a, but by a large fraction. On the other hand, within this subset of 60 small discrepancies, there are 33 cases (55%) in which the community models were not guided by any dated offset geologic features in the tables of *Bird* [2007] that provided their geologic input. Predicting a fault offset rate in advance of any geologic measurement is a hard test for any deformation model.

The remaining cases are 11 (8%) in which the discrepancy was larger than 1 mm/a. Nine of these were under 4 mm/a, and two were much larger (11 and 26 mm/a, respectively). These problems cluster in the Mojave Desert region of California, where it is well-known that geologic and geodetic rates are difficult to reconcile. These large discrepancies will be considered individually in the regional discussion below.

After this comparison, the 126 new offset rates (and 10 new fault traces) were combined with those already published [Tables 1 & 2 of *Bird,* 2007] to obtain updated combined geologic

target rates and standard deviations for all fault trains. Four additional NeoKinema models, here called the "updated" model set, were computed with the revised geologic target rates and uncertainties and fault traces, keeping other input datasets unchanged. These models used either the NUVEL-1A or the Guadalupe pole for NA-PA, and either WGCEP Fault Model 2.1 or 2.2 in California. On the basis of minimum misfit, model GCN2008088 (Guadalupe pole, Fault Model 2.2) was selected as the best updated model, and therefore as the "preferred" model of this paper, which is displayed in most map-view figures. **Figure 12** shows the long-term velocity field of this model.

It is interesting how little the preferred model changes as a result of these 68 updated geologic target rates. Comparing models GCN2008060 and -088, no offset rate changes by more than 3 mm/a. On the San Andreas fault, the Big Bend train slows from 15.4 to 13.6 mm/a, the Mojave N train speeds up from 17.4 to 20 mm/a, the San Bernardino N train slows from 18.9 to 16.6 mm/a, the San Bernardino S train speeds up from 12.2 to 13.4 mm/a, and the Coachella train speeds up from 15.1 to 17 mm/a. On the Elsinore fault, the Temecula stepover train speeds up from 0.8 to 3.7 mm/a, and the en-echelon Glen Ivy stepover train slows from 3.7 to 1.3 mm/a in local compensation. Throw rate increases on the Carson Range normal fault from 0.2 to 2.9 mm/a. All other changes are less than 1.8 mm/a. (All updated offset rates for fault trains with new data are shown in Table 4.) In this test, the addition of several years of new (or newly-catalogued) geologic rates had only modest effects on the preferred NeoKinema model, indicating its stability. On the other hand, this stability means that many discrepancies remain: 10 (8% of new data) remain above 1 mm/a, and 25 (20% of new data) below 1 mm/a. This is desirable behavior if the discrepancies are due to errors [*Bird,* 2007] in the new data, but obviously not desirable if the errors are in the model.

7. Regional Discussion and Ad-hoc Experiments

NeoKinema provides predictions of fault offset rates in two formats. In most text and in Table 4 of this paper, the quantities described as model predictions have been the length-weighted along-trace averages of model offset rates in all the finite elements cut by one fault train. When this along-trace average is plotted all along the trace, as in **Figure 13A**, the result is a ribbon of uniform width; this is easy to interpret, but potentially misleading. The more informative display of **Figure 13B** shows per-element estimates of fault offset rate, with all their noisy discontinuities in strike and value. Such a display includes some artifacts (especially unreasonably high rates at some fault terminations), but also displays some important variations in slip-rate along traces which are due to interactions between faults and/or distributed anelastic deformation. In the remainder of this paper, detailed/noisy plots similar to Figure 12B will be shown in order to convey more information.

7.1. Washington and Oregon

As in most plate-tectonic models, relative motion in the greater Washington-Oregon region (including adjacent seafloor) is dominated by spreading/transform activity on the northern Gorda Ridge and convergence in the Cascadia subduction zone (Figure 13). (Speading on the Juan de Fuca Ridge is not shown in this figure because it is outside the model domain shown in Figure 1). Convergence in the Cascadia subduction zone is relatively constant at values near the mean rate of 36.7 mm/a (Figure 13A, B). However, the strike-slip component changes locally with the azimuth of the trace of the plate boundary, so that its mean of 2.8 mm/a dextral (Figure

13A) conceals local variations from 15 mm/a sinistral to 29 mm/a dextral (Figure 13B). (These local variations have little tectonic significance; I mention them only to illustrate the difference between these two ways of plotting the predictions of the same model.)

In the Cascadia forearc offshore Oregon (43°~46.5°N) 11 WNW-trending high-angle faults have been mapped by *Goldfinger et al.* [1992] and/or *Personius et al.* [2003]. All were entered in my database as nominally sinistral faults, although this was based primarily on the conceptual model of *Goldfinger et al.*; only the Wecoma and Coos Basin faults have sinistrally-offset features, and only the Wecoma fault has a geologic offset rate, of 9.1±2.2 mm/a, which comes from the part of the fault on the Juan de Fuca plate. In the preferred NeoKinema model, sinistral motion on the Wecoma fault is preserved because of its relatively well-constrained geologic rate, but most of the other faults are predicted to slip with a dextral sense, at lower rates. This raises serious doubt about the continuity of the Wecoma fault where it crosses the Cascadia trench. The part of the fault on the Juan de Fuca plate is sinistral where it offsets the Astoria fan, but perhaps the part of the fault in the North America plate is dextral, and the alignment between these two opposite-sense faults is coincidental and temporary (as the Juan de Fuca plate drifts NE relative to NA). The kinematic incompatibility that would normally arise between aligned sinistral and dextral faults would be relieved in this case by a quadruple-junction with the Cascadia trench, and a decrease in subduction rate on the N side of this junction relative the S side.

An interesting prediction of the preferred NeoKinema model is that Oregon is bisected by an active dextral fault system composed of 5 aligned faults: from NW to SE, the Tillimook Bay fault (predicted mean dextral rate 1.9 mm/a), the Newburg fault (3.8 mm/a), the Mount Angel fault (3.2 mm/a), the Clackamas River fault (3.2 mm/a), the Sisters fault zone (0.5 mm/a), and the 280-km-long Brothers fault zone [*Lawrence*, 1976; *Walker*, 1977; *Christiansen & Yeats,* 1992] (3.0 mm/a). Distributed deformation bridges the gaps between these traces to create a continuous belt of dextral shear at about 3 mm/a. In the model, this belt acts as a transform fault system accomodating the northern termination of many normal faults in southeastern Oregon [*Lawrence*, 1976] and northwestern Nevada (Figure 12). Because none of these predicted dextral faults had a well-constrained geologic slip rate in the input data, this result is primarily dictated by regional kinematic compatibility, and by the PBO GPS velocity solution. Additional campaign-mode GPS velocities that can check this prediction (because they were not included in the "community" datasets) were published by *Hammond & Thatcher* [2005]. They interpreted clockwise relative rotation between their microplate CSOR (Central Southern OR) and stable NA with Euler pole (-118°E, 44.3°N, -0.8°/m.y.) that would be consistent with dextral slip on the Brothers fault zone, at rates increasing from 2.1 mm/a at its SE end to ~3 mm/a at its NW end (where there would also be an extensional component). However, *Hammond & Thatcher* did not discuss this fault system, or identify any other discrete microplate boundary. To test this part of the NeoKinema model, I computed one ad-hoc model (GCN2008100) with the addition of 49 new *Hammond & Thatcher* [2005] GPS velocities in Oregon to those used previously. This model scored slightly better than the "preferred" model GCN2008088 because of its lower stress misfit (which was probably due to the "dilution" of the influence of a questionable high GPS velocity at MDMT in the WGCEP solution). Model GCN2008100 predicts a mean dextral slip rate of 2.3 mm/a instead of 3 mm/a on the Brothers fault, but in every other way is qualitatively identical to the preferred model. This is another demonstration of the stability of the NeoKinema modeling process.

Another area of relatively rapid faulting in this region is the thrust belt in the seaways of Juan de Fuca Strait, San Juan archipelago, and Puget Sound. The West Coast-West San Juan-Survey Mountain thrust along the SW side of Vancouver Island has predicted mean heave rate of 0.9 mm/a, with slip beginning at Clayoquot and increasing southeastward to 1.3 mm/a in southeastern Vancouver Island. To the east, this shortening is divided between a north branch on the Devils Mountain thrust (mean heave rate 0.44 mm/a; locally up to 0.65), and a south branch on the South Whidbey Island thrust (mean heave rate 0.63 mm/a). Further south in Puget Sound, a crustal block between the Seattle and Tacoma thrust faults is predicted to be elevated at throw rate 0.2 mm/a by heave rates of about 0.55 mm/a on each of these faults. (Other faults not mentioned have lower mean rates.) This association of active thrusting with deep glacial troughs is intriguing. Perhaps it is due to an observer bias resulting from higher population densities and/or easier access in these areas. Or, if it is real, it could reflect an enhancement of thrusting by the Pleistocene glacial removal of topographic mass that would otherwise oppose and moderate thrusting. A similar process on a grander scale was proposed for the Chugach-Wrangell Mountains region of Alaska by *Bird* [1996].

7.2. Mendocino triple junction region

Relative motion between the rigid northern part of the Juan de Fuca plate and the Pacific (JF-PA) is parallel to the Blanco fracture zone at azimuths of 110~120°, as *Chadwell & Spiess* [2008] recently confirmed with seafloor geodesy. The Mendocino fault is part of the same JF-PA plate boundary, but has azimuth 93°. This creates a problem of excess area in the southern "Gorda orogen" part of the Juan de Fuca plate, which requires thrust-faulting.

One possibility is that the Mendocino fault is an oblique right-transpressional fault, with underthrusting of Juan de Fuca crust to the south [*Silver*, 1971], especially in the Gorda Escarpment portion east of 126°W. One possible indicator of thrusting is a linear dipolar gravity anomaly of 90 mGal amplitude along the Mendocino fault [*Leitner et al.*, 1998] with more negative anomalies to the N and more positive to the S. Another is depression of the Moho and crustal thickening to 12 km in the northeast corner of the Pacific plate within 25 km of the Mendocino triple-junction [*Henstock & Levander*, 2003] without accompanying surface deformation. Because of these arguments, I permitted oblique slip on the Mendocino fault in most models; in the preferred model, its mean convergent heave rate is predicted to be 10 mm/a, superimposed on a mean dextral rate of 33.5 mm/a (**Figure 14A**). Therefore, the predicted azimuths of slip vectors would be about 110°, and this is kinematically close to a rigid-plate solution. The many faults mapped by *Chaytor et al.* [2004] are active in sinistral and/or reverse senses in this model, but mostly at very slow rates of less than 0.1 mm/a. The average rate of the 24 "active" sinistral faults is 0.12 mm/a.

Other authors [*Smith et al.*, 1993; *Gulick et al.,* 2001] have denied any component of thrusting on the Mendocino fault. Because the question is open, I also computed ad-hoc model GCN2008101 in which the Mendocino fault is treated as a purely strike-slip vertical fault. Results in Figure 14B are subtly different: 10 mm/a of N-S shortening is absorbed about equally by fault slip and distributed deformation within the southern "Gorda orogen" part of the Juan de Fuca plate. The average slip velocity on the 24 active sinistral faults identified by *Chaytor et al.* [2004] increases to 0.28 mm/a. This ad-hoc model also involves a slightly greater indentation of the northeast corner of the Pacific plate, and a slightly reduced slip rates on the northernmost (Offshore) train of the San Andreas fault (7.8 instead of 9.3 mm/a at Cape Mendocino; mean 8.3

instead of 8.8 mm/a). However, there is no dramatic change predicted that would be easy to test on land.

There is another space problem in the region. As pointed out by *McCrory* [2000], the northernmost part of the San Andreas trace does not align with the Mendocino triple junction, but instead lies ~70 km East of its ideal position. Where the San Andreas bends sharply westward in the King Range/Punta Gorda area, a corner of the Pacific plate is colliding with Cascadia forearc of the North America plate. The SW-dipping King Range and Petrolia thrust faults at this critical corner may not have moved since Early Quaternary time [*Jennings*, 1994], and are not included in the WGCEP Fault Models. However, extending for 100 km North along the California coast is an active fold-and-thrust belt of mostly NE-dipping thrusts (and blind thrusts beneath anticlines) whose offset rates (and structural growth rates) were catalogued by *McCrory* [2000]. She estimated their total shortening rate conservatively as 10 mm/a. (My alternative analysis, assuming thrust fault dips of only 20°, suggests that shortening is permitted to range from 14~24 mm/a.) Either is less than PA-NA relative velocity of ~48 mm/a; but the facts that collision is oblique and that many of these thrust faults are longer than the 70-km width of the indentor may allow for area-balancing. The preferred model of Figure 14A satisfies 9 of *McCrory's* 17 rates (Table 4), with a mixture of under- and over-predictions in the other 8 cases. The Russ thrust fault has the only large discrepancy, with predicted throw rate of 3.1~3.5 mm/a exceeding one of *McCrory's* two constraints, while nearly agreeing with the other. The model also predicts its second-greatest concentration of distributed deformation (second only to the Imperial Valley region) around Cape Mendocino (Figure 6).

7.3. San Francisco Bay area and central California Coast Ranges

Model predictions (**Figure 15**) in this area are for dextral slip unless otherwise noted. At 39°N (*e.g.,* Point Arena) the 34.1 mm/a of shear between the borderland and the Great Valley plate is divided among: San Andreas (North Coast) 12.6, Maacama-Garberville 10.2, Bartlett Springs 7.8, and distributed deformation of 3.5 mm/a. At 38°N (*e.g.,* Point Reyes) the 35.3 mm/a of shear is divided among: San Andreas (North Coast) 23.0, Hayward (No) 6.7, Concord 3.0, and distributed deformation of 2.6 mm/a. At 37°N (*e.g.,* Santa Cruz) the 36.6 mm/a of shear is divided among: San Gregorio (No) 0.8, Zayante-Vergeles 1.4, San Andreas (Santa Cruz Mtn) 21.8, Calaveras (So) 4.9, Ortigalita 3.0, and distributed deformation of 4.7 mm/a. At 36°N (*e.g.,* Kettleman City) the 36.6 mm/a of shear is divided among: Hosgri 1.6, Rinconada 0.9, San Andreas (Parkfield) 31.5, and distributed deformation of 2.6 mm/a. Note that distributed deformation is only 7~13% of total in this region because of the generally subparallel and continuous fault traces which are also nearly parallel to relative plate motion.

Thrusting is predicted at low convergent heave rates on 4 faults in the region: Mount Diablo thrust 0.17 mm/a, Monte Vista-Shannon thrust 0.26 mm/a, Zayante-Vergeles thrust 0.32 mm/a, and Monterey Bay-Tularcitos thrust 0.9 mm/a (combined with 0.6 mm/a dextral slip).

Comparing mean slip rates in this preferred model with those selected by *2007 WGCEP* [2008] for their seismic hazard forecast, the biggest contrast is that this model tends to have lower mean rates on many (but not all) trains of the San Andreas system. From NW to SE: Offshore train 8.8 *vs.* 24 mm/a, North Coast 16.2 *vs.* 24, Peninsula 17.9 *vs.* 17, Santa Cruz Mtn 22.6 *vs.* 17, Creeping Segment 29.1, Parkfield 31 *vs.* 34, Cholame 26.4 *vs.* 34, Carrizo 25 *vs.* 34, and Big Bend train 13.6 *vs.* 34 mm/a. This is because WGCEP rates were primarily based on

rigid microplate models, whereas this model has large fractions of PA-NA relative motion accomodated by distributed deformation (see section 4.4 above).

7.4. Southern California

Predicted fault heave rates from the preferred model are shown in **Figure 16**. Neotectonics in southern California are complicated by the 154-km left step of the San Andreas fault system, which requires thrust-faulting. One organizing factor is the boundary condition applied to the base of the crust by the symmetrical downwelling of mantle lithosphere under the Transverse Ranges [*Bird & Rosenstock*, 1984]. However, in the absence of true subduction, locations of thrusting change through geologic time due to relative advection of faults, growth of topographic resistance, and growth of bending-stress resistance. Another chaotic or disorganizing factor is the frequent reactivation of diverse faults formed in earlier stages of the tectonic history [*Ingersoll & Rumelhart*, 1999].

A budget for the total rate of thrust-faulting in the Transverse Ranges (from the Tehachipi Mountains on the N to the San Joaquin Hills on the S) is obtained by multiplying the width of this left step by the relative velocity of the Pacific plate with respect to the Sierra Nevada/Great Valley plate: 154 km × 35 km/m.y. = 5390 (km)^2/m.y.. The following 10 thrust faults, listed with their lengths and mean convergent heave rates, are the most prominent contributors to area loss among the 75 nominal thrust or oblique-thrust faults in the Transverse Ranges, and together they make up 50% of the budget: Red Mountain 100 km × 7.1 mm/a = 13.3%, White Wolf 64 km × 6.6 mm/a = 7.8%, Oak Ridge (Offshore) 38 km × 6.7 mm/a = 4.7%, Oak Ridge (Onshore) 49 km × 5.1 mm/a = 4.7%, Santa Susana (alt 2) 43 km × 5.3 mm/a = 4.2%, Simi-Santa Rosa 39 km × 4.6 mm/a = 3.3%, Santa Cruz Island 69 km × 2.6 mm/a = 3.3%, White Wolf (Extension) 46 km × 3 mm/a = 2.6%, Channel Islands thrust 59 km × 2.3 mm/a = 2.6%, and San Cayetano 42 km × 3.1 mm/a = 2.4%. Distributed deformation takes up 38.4% of the budget. The other 11.6% is the net shortening among the other 65 nominal thrust faults in the Transverse Ranges, but as some of these are predicted to have extensional slip in the preferred model (*e.g.*, Mission Ridge-Arroyo Parida-Santa Ana, Nacimiento, and San Gabriel) there is some cancellation of area changes within this group. It is interesting that very little of the shortening is taken up along the impressive mountain fronts of the San Bernardino and San Gabriel Mountains (North Frontal faults 77 km ×1.7 mm/a = 2.3%; Mission Creek 32 km × 1.2 mm/a = 0.7%; Cucamonga fault 28 km × 2.6 mm/a = 1.4%); instead it occurs primarily within the lower topography of the Santa Barbara Channel, Channel Islands, Simi Valley, and south of the San Gabriel Mountains. This may be a sign of very low crustal strength, and the consequent regulation of thrusting by the topographic resistance that it eventually generates.

In the Imperial Valley region of southeastern California and northern Baja California, it is notorious that the primary fault trains of the plate boundary (Cerro Prieta, Imperial, San Andreas, San Jacinto (Superstition Mountain), Laguna Salada, and Elsinore (Coyote Mountain)) are not mapped as connecting to each other. One reason is recurring coverage by lacustrine or marine sediments. Another may be tectonic decollement on weak evaporite horizons within the sedimentary section. A third is rapid intrusion of basaltic dikes (analogous to seafloor spreading) beneath the sedimentary cover, which may link some mapped faults by creating gaps in the lithosphere. The WGCEP Fault Models attempt to close one large gap between traces by elevating the intrusive center known as the "Brawley seismic zone" to the status of a fault (for strike-slip only), but they leave other gaps. Consequently, the preferred model has extremely

high rates of distributed deformation in this region (Figure 6). It is important to include this distributed deformation as a potential source of seismicity, which would otherwise be underestimated. If heat-flow or seismic tomography should show the lithosphere to be very thin in some areas, this can be considered when converting rates of distributed anelastic deformation to long-term seismic moment rates.

7.5. Mojave Desert: San Andreas fault versus Eastern California shear zone

There has been extensive debate about the long-term crustal flow in this region, which can be summarized by reference to 5 conceptual models. The primary contendors are: (1) a "geologic model" based on dated offset features in the Eastern California shear zone which indicate a low rate of dextral shear [*e.g.*, 5.9±1.4 mm/a per *Oskin et al.*, 2006]. If the motion of the western Mojave relative to stable NA is only 6 mm/a, then the slip rate of the Mojave trains of the San Andreas must be high [*e.g.,* 30±10 mm/a per *Matmon et al.*, 2005; 30~46 mm/a per *Rust*, 2005]. This model is opposed by a (2) "geodetic model" which estimates Eastern California shear zone motion as 12±2 mm/a [*e.g., Sauber et al.*, 1994] and estimates a lower rate of dextral slip on the Mojave trains of the San Andreas [*e.g.*, 14.3±1.2 mm/a per *Meade & Hager*, 2005]. Both of these models are conceived in terms of the steady flow of elastic microplates.

Three more concepts attempt to add degrees of freedom to resolve the controversy. A (3) "cyclical model" suggests that crustal flow switches between two modes, and that geologists and geodecists have observed different parts of the cycle [*e.g., Dolan et al.,* 2007]. Another (4) "rheologic model" attempts to show how high rates of slip on the San Andreas could be disguised by rheologic structures at depth to appear as low rates in simplistic inversions of geodetic data [*Johnson et al.*, 2007]. Finally, (5) "distributed deformation" might reconcile the geodetic rate with geologic offsets in the Eastern California shear zone [*Oskin et al.*, 2007], at least.

Program NeoKinema is not able to test concepts (3) or (4) because they have not been developed into formal hypotheses. (Mode-switching has no articulated cause or mechanism, and its kinematics outside the Mojave region are vague. The *Johnson et al.* [2007] model of the San Andreas requires that there is no fault at the level of the mantle lithosphere, which is hard to reconcile with 240 km of net displacement on the southern San Andreas [*Buesch & Ehlig,* 1982].) So, NeoKinema predictions are necessarily some mixture of models (1), (2), and (5). Results of the preferred model in this study are closest to the "geodetic model" (2) with an added component of "distributed deformation" (5). I do not think that this is due to inadequate weight on the geologic constraints. (See section 2.2 for discussion of how the geologic misfit measure was redefined upward, and section 5 for discussion of how geologic and geodetic misfits were balanced.) Instead, it is because of two simple constraints: (i) Geologic slip rates are not uniformly high for the Mojave South train of the San Andreas. Including all sources (*Ehlert & Ehlig* [1977], *Buesch & Ehlig* [1982], *Sieh* [1984], *Barrows et al.* [1985], *Frizzell et al.* [1986], *Meisling & Weldon* [1986], *Schwartz & Weldon* [1986], *Sieh et al.* [1989], *Salyards et al.* [1992], *Weldon et al.* [2002, 2004, 2008], and *Matmon et al.* [2005]) in an analysis by program Slippery, the combined rate is only 21.9±3.85 mm/a (median±standard deviation; 95%-confidence range 16.2~29.3 mm/a). (ii) Geodesy has convincingly demonstrated that the Sierra Nevada/Great Valley plate moves NW at 12~13 mm/a relative to stable North America [*e.g., Argus & Gordon,* 2001]. Because the western Mojave overthrusts the Sierra Nevada/Great Valley plate on the left-

transpressional White Wolf and White Wolf (Extension) faults, its velocity to the NW must be higher than this.

The preferred model GCN2008088 has mean slip rates on the Mojave N and Mojave S trains of the San Andreas of 20.1 and 17.4 mm/a, respectively (Figure 16). It is important to note the apparent conflict with recent geologic rates by *Matmon et al.* [2005] and *Rust* [2005] which had 95%-confidence lower limits of 21 mm/a (fan #0), 43 (fan #1), 16 (fan #3), 21 (fan #4), 28 (fan #5) and 30 mm/a, respectively. However, each of these rates is only as good as its offset distance, and each offset distance is only as good as the assumption that the drainage crossed the fault in a straight line at a right angle during deposition of the dated sediment. If sediments were deposited at a time when the drainage already had a right-lateral kink, then offset distances and rates have been overestimated. Similar (but left-lateral) arguments may apply to the Garlock (Central) sinistral fault, where the model predicts only 3.8 mm/a, but two offsets identified and dated by *McGill & Sieh* [1993] imply minimum rates of 5 or 6.2 mm/a, respectively,

Other "large" (> 1 mm/a) discrepancies (Table 4) occur on the Blackwater fault in the Eastern California shear zone, where the model is predicting a dextral slip rate of 1.8 mm/a, which is higher than two geologic rates of *Oskin & Iriondo* [2004] with upper limits of 0.3 and 0.5 mm/a, respectively. Since their offset lava flows are pre-Quaternary (7.2 and 3.8 Ma, respectively), a resolution may be possible if Blackwater fault slip began about 1 Ma.

Generally, the preferred model has elevated the dextral rates of all faults in the Eastern California shear zone (Figure 16) above their input target geologic rates, but only by an average of +0.6 datum standard deviations, so it has not exceeded 95%-confidence upper limits on other faults. The solution also incorporates high rates of distributed deformation ($1{\sim}5{\times}10^{-15}$/s, Figure 6) to bring the net dextral rate up to the geodetic value. A third contribution comes from clockwise rotation of small crustal blocks in the northeast and east-central Mojave Desert, which is accomodated by left-lateral slip on E-trending faults separating these blocks. Another block which rotates clockwise is that containing Joshua Tree National Park, which lies between the Pinto Mountain and Blue Cut faults. These predicted clockwise rotation rates increase southward, from ~4°/m.y. just S of the Garlock fault, to ~10°/m.y. in the central eastern Mojave, and reach ~20°/m.y. at Joshua Tree National Park.

7.6. Walker Lane

Wesnousky [2005] presented a comprehensive review of active faulting and block rotation in the Walker Lane. Preferred model GCN2008088 supplements this with estimates of fault heave rates, as seen in Figure 15 and **Figure 17**.

The preferred model does not have any significant rate of slip on the Stateline dextral fault system mapped by *Guest et al.* [2007]. Although this fault was assigned a target dextral rate of 2.4±9.1 mm/a based on offset of 30±4 km since 13.1±0.2 Ma, its model rate is only 0.06 mm/a. This is due to the lack of geodetic evidence for continuing strain in the region, and also to the lack of connecting structures on its SE end.

South of 37°51'N (Boundary Peak, NV), the model has dextral shear shared between two widely-separated but Northward-converging fault systems. On the western system, dextral slip at 2.4 mm/a on the Panamint Valley fault connects to dextral slip at 2.1 mm/a on the Hunter Mountain-Saline Valley fault. Continuing northward, there is a gap before dextral slip is taken

up by the White Mountains fault at mean rate 2.3 mm/a; this gap is bridged by slip transfer to the nearby and parallel Owens Valley fault, which has a mean dextral component of 1.9 mm/a.

The eastern dextral fault system includes (S to N) the Death Valley (So) train at 1.6 mm/a, the Death Valley (Black Mountains frontal) train at 2.0 mm/a (dextral component), the Death Valley (No) train at 2.6 mm/a, and the Death Valley (N of Cucamongo) train at 1.4 mm/a.

Both the western and the eastern systems have releasing bends (right steps) in the latitudes of Death Valley. This is the primary cause of the extensional fault-normal (D) rate component of 2.3 mm/a predicted for the Death Valley (Black Mountains frontal) train. In this model, other normal or oblique-normal faults of the southern Walker Lane have relatively small extensional heave rates (*e.g.,* Deep Springs fault D = 0.6 mm/a; So Sierra Nevada D = 0.3 mm/a), and do not form a connected extensional system.

As *Wesnousky* [2005] predicted, the central Walker Lane (37°51'~38°25'N) is occupied by the Excelsior-Coaldale block(s), bounded by ENE-trending faults with high rates of sinistral slip, which rotate clockwise at ~3°/m.y.. In the model these sinistral faults include (S to N): the connected Coaldale faults #1 & #2 at 2.5 mm/a, connected sinistral faults #1302 and #1303 at ~1.5 mm/a, and the sinistral faults of the southern Garfield Hills (#1304) at 3.5 mm/a. (Fault names in this paragraph follow *Haller et al.* [2002].) Locally, the rotating block pulls away from the White Mountains block at D =2.3 mm/a on the Boundary Peak detachment fault [*dePolo*, 1998]; isostatic rebound of the footwall probably explains the prominent height of this peak.

In the northern Walker Lane (Figure 17), there is another cycle of dextral faulting-block rotation-dextral faulting. At the border between Figures 16/17 (38°40'N) the Gumdrop Hills fault (3.1 mm/a) and the Bettles Well-Petrified Springs fault (1.6 mm/a) are carrying most of the dextral slip [*c.f. Wesnousky*, 2005]. Then, in the greater Reno area (39°~40°N, 120°~119°W) there is another set of 3 clockwise-rotating blocks bounded by 4 NE-trending sinistral faults (1.1~2.8 mm/a) including the Spanish Springs Peak fault. (Note that none of these faults has a dated offset feature to give a geologic rate, so NeoKinema has estimated these rates from kinematic compatibility.) Then, at 40°N (near the California border) dextral slip resumes, where it is divided between the Honey Lake fault (1.2 mm/a), Warm Springs Valley fault (1.4 mm/a), and Pyramid Lake fault (2.3 mm/a). This is not the end of the Walker Lane, as there are additional NW-trending faults in the lava beds of the Modoc Plateau which are presumably dextral or dextral-transtensional. However, as they were not catalogued in WGCEP Fault Models, their activity is treated here as distributed deformation, at rates up to 2×10^{-15} /s (Figure 6), extending up to the Oregon border.

7.7 Inland states

In the interior of the western U.S., geologic and geodetic data are less concentrated than they are in coastal states. *Wesnousky et al.* [2005] has collected geologic rates for many of the Basin & Range normal faults along one transect (Table 4), but elsewhere in the province Quaternary geologic rates are quite rare. Therefore, many Basin & Range normal faults in this model have prior/input throw rates set to the generic N = 0.183±0.343 mm/a (see section 3.2), which scales to a generic heave rate of D = 0.128±0.24 mm/a. Other normal faults have rates based on minimum net throw (from scarp heights) since some time in the Oligocene or Miocene, but because of the throw uncertainty and great age of these offset features program Slippery attributes a comparable or even greater proportional uncertainty [*Bird,* 2007]. Also, the

relatively low strain rates and fault slip rates in the interior mean that differences between velocities of adjacent geodetic benchmarks are typically less than the uncertainties in their velocities. These (relative) deficiencies in quantity and precision of inland data make the NeoKinema inverse problem "soft" or "easy" in the sense that many offset rates and geodetic velocities can be set to their prior/input values without causing any serious conflict with adjacent data. Consequently, the inland part of the map of long-term velocities (Figure 12) looks like a (smoothed) map of GPS velocities, while the maps of predicted fault heave rates (**Figures 17-19**) look very much like the prior/input values computed and tabulated in Table 1 of *Bird* [2007]. Due to length limits on this paper, these inland predicted fault heave rates are only presented graphically (and in an attached digital supplement), without discussion.

However, one kind of artifact that appeared in these figures requires explanation. When I prepared preliminary versions of Figures 17-19 using results from the preferred model GCN2008088, I saw that certain Basin & Range "normal faults" (according to the input dataset) were predicted to be slipping as reverse faults. The worst region was east-central Nevada, where 10 "normal faults" out of 195 had the wrong sense of throw, with the most negative rate at −1.5 mm/a. This is very implausible from a dynamical point of view. Most likely these predictions are artifacts. They could result from a few geodetic velocities which are not "interseismic" as assumed because there was some undetected creep event or slow earthquake in the region, either during or just before the time window of geodetic observations. Alternatively, they could result from a "crowding" effect if the default normal throw rate is too high for this region of many closely-spaced normal faults. Fortunately, such artifacts can be removed by an iterative process. In the first round of corrections, 22 inland "normal faults" with rapid reverse-slip predictions were removed from the input data for ad-hoc model GCN2008102, effectively locking these faults. In the next calculation, when these faults could no longer accommodate shortening, extensional rates on neighboring faults were reduced and some became negative which had previously been positive. A second correction involving the deletion of 18 remaining wrong-way faults (even those with N = -0.001 mm/a) gave ad-hoc model GCN2008103, which has very few artifacts in inland states. This iterated model is the basis for the versions of Figures 17-19 displayed.

8. Forecasting Seismicity

The techniques displayed here can contribute to forecasts of seismicity in 3 ways:

(1) Successful NeoKinema models provide better fault slip rates. Because geologic slip rates are unavailable or conflicting for many faults, committees of experts have often been assembled to choose rates (which I have referred to as "consensus combined rates"). Program Slippery of *Bird* [2007] illustrated how computational statistics can be used to deal with conflicting or incomplete information about geologic offsets along any individual fault train. Program NeoKinema, run with input from Slippery, goes further by providing posterior/output estimates of fault slip rates which also take into account geodetic velocities, stress directions, kinematic compatibility, and plate tectonics. Although slip rates from one particular NeoKinema model do not come with uncertainties, a range of rates can be assembled from a suite of acceptable alternative models using different fault sets and Euler poles (*etc.*) as illustrated by attached file **f_GCN_nko_ranges.txt** (based on the 16 acceptable community models, 4 updated models, and 4 ad-hoc models of this paper). Expert panels would still be needed, but their roles could be modified to emphasize (a) collection and screening of data to be used in computations;

(b) review of predictions for obvious artifacts, including (c) consideration of cases where NeoKinema predicts the wrong(?) sense of slip; and (d) consideration of paleoseismic studies as to whether particular faults creep or stick-slip.

The problems with extracting *only* improved slip-rates from NeoKinema modeling are that: (i) varying slip rates on one fault are typically correlated with varying slip rates on neighboring faults, so it is not appropriate to treat these refined slip-rate ranges as independent; (ii) long-term fault slip rates often vary along the fault trace, and this is not captured by using only the along-trace mean rate for seismicity prediction; and (iii) modeling in this paper has shown that as much as 1/3 of relative motion between some pairs of plates is accomodated by distributed anelastic deformation off the mapped fault traces. Therefore, a superior approach considers that:

(2) Successful NeoKinema models are deformation models. Each computation provides estimates for the slip rate of each fault in each finite element (typically 15-30 km wide) as seen in Figures 13B~19 of this paper. These are "noisy" in two ways: they are discontinuous between elements, and sometimes implausibly large at fault terminations. However, it would be easy to apply smoothing if this were thought desirable. Also, each computation provides an estimate of the tensor of distributed anelastic strain rate for each finite element. Again, discontinuities at element boundaries are artifacts, but these could easily be smoothed. (Any smoothing method should conserve seismic moment rate.) Using this fine-grained and detailed information from one finite-element model addresses all 3 concerns of the previous paragraph. (As examples, I attach 2 files as supplemental material with the predictions of the preferred model: **h_GCN2008088.nko**, and **e_GCN2008088.nko**.) The principal decision that has to be made is whether to consider distributed anelastic deformation as a source of earthquakes; I argue that this is prudent.

Given a deformation model, there are still many controversial decisions which have to be made (or straddled) to get to a seismicity forecast. The report of *2007 WGCEP* [2008] decribes a complex logic-tree with branches expressing divergent models about fault segmentation, area/magnitude relations, characteristic earthquakes, periodic earthquakes, and ruptures outside the mapped fault traces. Incorporation of these many divergent models will always require a large team and very complex programs. This makes it difficult to update models quickly in response to new information, and it makes the modeling process laborious and expensive. In some cases, in may be desirable to consider a simpler two-step alternative:

(3) Program Long_Term_Seismicity can transform any preferred NeoKinema model into a map of estimated long-term seismicity, after which the forecast can be made time-dependent by introducing the modulating effects of actual historical seismicity with an empirical statistical model. The first step implies provisional acceptance of the SHIFT hypotheses reviewed in section 2.3 of this paper, and the calibration constants estimated by *Bird & Kagan* [2004]. The second step might involve treating some fixed fraction of the long-term seismicity map as the "background" or "immigrant" term in an epidemic-type earthquake sequence (ETES) model like that of *Werner* [2007], using maximum-likelihood methods to obtain the ETES parameters from the historic earthquake catalog, and then projecting the model forward in time. In this way, time-dependent processes such as aftershock sequences, earthquake clustering, and stress-shadowing could be added as perturbations to a steady process, while demonstrating at each step that the (single) model is statistically optimal and free of subjective elements.

To illustrate the first of these steps, I show in **Figure 20** a calculation of long-term shallow seismicity based on preferred NeoKinema model GCN2008088 of this study. The forecast is also attached as supplemental material in digital form: **LTS_GCN2008088_m5p663.grd**. The threshold is moment-magnitude 5.663 (scalar seismic moment 3.5×10^{17} N m), above which the Global CMT catalog (like most seismic catalogs covering the western U.S.) is probably complete since 1977. Then, in **Figure 21** I superpose actual shallow seismicity from 1977.01.01-2008.03.31 in the same region from the Global CMT catalog. There is absolutely no circularity in this comparison because historical seismicity played no part in the NeoKinema modeling, and because the Gorda-California-Nevada orogen was excluded from the spatial domain used by *Bird & Kagan* [2004] to estimate the seismicity constants of different kinds of plate boundaries.

In a longitude/latitude "trapezoid" (128~104°W, 30~49°N) surrounding the NeoKinema model, the forecast long-term seismicity rate of $m > 5.663$ shallow earthquakes is 4.49/year. The actual record in 1977.01.01-2008.03.31 was 70 earthquakes, or 2.24/year. This suggests that the western U.S. has been 50% below its long-term seismicity rate, and should be expected to have more shallow earthquakes in the future. The map pattern in Figure 21 shows several prominent seismic gaps: First, the Cascadia subduction zone (as opposed to the adjacent Gorda orogen) in the smaller trapezoid (128~122°W, 42~49°N) produced only 9 $m > 5.663$ shallow earthquakes in this period for a rate of 0.288/year, although its long-term average rate is expected to be 1.44/year. In the remainder of the large trapezoid, the deficit was less dramatic: 1.95/year actual versus 3.05/year expected (64% of expectation). Figure 21 shows that much of this remaining deficit occurred along the North Coast, Big Bend, and northern Gulf of California portions of the Pacific-North America boundary. The Garlock fault has also been very quiet.

Now, we know from historic great earthquakes in 1700 AD (Cascadia) and 1857 and 1906 AD (San Andreas) that the relative quiescence in at least 3 of these regions is temporary. Whenever the next great earthquake occurs on either fault, it is likely to be associated with clusters of $m > 5.663$ aftershocks and more distant triggered seismicity which will make up the deficit, and likely even exceed the long-term rate.

Acknowledgements

References

2007 Working Group on California Earthquake Probabilities: E. H. Field, T. E. Dawson, K. R. Felzer, A. D. Frankel, V. Gupta, T. H. Jordan, T. Parsons, M. D. Petersen, R. S. Stein, R. J. Weldon II, and C. J. Wills [2008] The Uniform California Earthquake Rupture Forecast, version 2 (UCERF 2), U. S. Geol. Surv. Open-File Rep., 2007-1437, 104 pages.

Altamimi, Z., P. Sillard, and C. Boucher [2002] ITRF2000: A new release of the International Terrestrial Reference Frame for Earth science applications, J. Geophys. Res., 107(B10), 2214, doi: 10.1029/2001JB000561.

Altamimi, Z., X. Collilieux, J. Legrand, B. Garayt, and C. Boucher [2007] ITRF2005: A new release of the International Terrestrial Reference Frame based on time series of station positions and Earth Orientation Parameters, J. Geophys. Res., 112(B9), B09401, doi: 10.1029/2007JB004949.

Antonelis, K., D. J. Johnson, M. M. Miller, and R. Palmer [1999] GPS determination of current Pacific-North American plate motion, Geology, 27(4), 299-302.

Argus, D. F. [2007] Defining the translational velocity of the reference frame of Earth, Geophys. J. Int., 169, 83-838, doi: 10.1111/j.1365-246X.2007.03344.x.

Argus, D. F., and R. G. Gordon [2001] Present tectonic motion across the Coast Ranges and San Andreas fault system in central California, Geol. Soc. Am. Bull., 113(12), 1580-1592.

Armstrong, P. A., A. R. Taylor, and T. A. Ehlers [2004] Is the Wasatch fault footwall (Utah, United States) segmented over million-year timescales?, Geology, 32(5), 385-388, doi: 10.1130/G20421.1.

Bacon, S. N., and S. K. Pezzopane [2007] A 25,000-year record of earthquakes on the Owens Valley fault near Lone Pine, California: Implications for recurrence intervals, slip rates, and segmentation models, Geol. Soc. Am. Bull., 119(7/8), 823-847, doi: 10.1130/B25879.1.

Bacon, C. R., M. A. Lanphere, and D. E. Champion [1999] Late Quaternary slip rate and seismic hazards of the West Klamath Lake fault zone near Crater Lake, Oregon Cascades, Geology, 27(1), 43-46.

Barrows, A. G., J. E. Kahle, and D. J. Beeby [1985] Earthquake hazards and tectonic history of the San Andreas fault zone, Los Angeles County, California, Cal. Div. Mines Geol. Open-File Rep., 85-10LA, 236 pages + 21 plates.

Beavan, J. P., P. Tregoning, M. Bevis, T. Kato, and C. Meertens [2002] Motion and rigidity of the Pacific plate and implications for plate boundary deformation, J. Geophys. Res., 107(B10), 2261, doi: 10.1029/2001JB000282.

Becker, T. W., J. L. Hardebeck, and G. Anderson [2005] Constraints on fault slip rate of the southern California plate boundary from GPS velocity and stress inversions, Geophys. J. Int., 160, 634-650, doi: 10.1111/j.1365-246X.2004.02528.x.

Behr, W. M., D. H. Rood, K. E. Fletcher, N. E. Guzman, R. Finkel, T. C. Hanks, K. W. Hudnut, K. J. Kendrick, J. P. Platt, W. D. Sharp, R. J. Weldon, and J. D. Yule [2008] Uncertainties in slip rate estimates for the Mission Creek strand of the southern San Andreas fault at Biskra Palms oasis (abstract), Proceedings and Abstracts, 18, 163, Southern California Earthquake Center, Los Angeles.

Bell, J. W., and T. Katzer [1990] Timing of late Quaternary faulting in the 1954 Dixie Valley earthquake area, central Nevada, Geology, 18(7), 622-625.

Bell, J. W., C. M. dePolo, A. R. Ramelli, A. M. Sarna-Wojcicki, and C. E. Meyer [1999] Surface faulting and paleoseismic history of the 1932 Cedar Mountain earthquake area, west-central Nevada, and implications for modern tectonics of the Walker Lane, Geol. Soc. Am. Bull., 111(6), 791-807.

Bell. J. W., S. J. Caskey, A. R. Ramelli, and L. Guerrieri [2004] Pattern and rates of faulting in the central Nevada seismic belt and paleoseismic evidence for prior belt-like behavior, Bull. Seismol. Soc. Am., 94, 1229-1254, doi: 10.1785/012003226.

Bird, P. [1996] Computer simulations of Alaskan neotectonics, Tectonics, 15(2), 225-236.

Bird, P. [1999] Thin-plate and thin-shell finite element modeling programs for forward dynamic modeling of plate deformation and faulting, Comput. Geosci., 25(4), 383-394.

Bird, P. [2003] An updated digital model of plate boundaries, Geochem. Geophys. Geosyst., 4(3), 1027, doi:10.1029/2001GC000252.

Bird, P. [2007] Uncertainties in long-term geologic offset rates of faults: General principles illustrated with data from California and other western states, Geosphere, 3(6), 577-595; doi:10.1130/GES00127.1, + 9 digital file appendices.

Bird, P., and Y. Y. Kagan [2004] Plate-tectonic analysis of shallow seismicity: Apparent boundary width, beta, corner magnitude, coupled lithosphere thickness, and coupling in seven tectonic settings, Bull. Seismol. Soc. Am., 94(6), 2380-2399.

Bird, P., and Y. Li [1996] Interpolation of principal stress directions by nonparametric statistics: Global maps with confidence limits, J. Geophys. Res., 101(B3), 5435-5443.

Bird, P., and Z. Liu [2007] Seismic hazard inferred from tectonics: California, in: S. E. Hough and K. B. Olsen (ed.), Special Issue on: Regional Earthquake Likelihood Models, Seismol. Res. Lett., 78(1), 37-48.

Bird, P., and R. Rosenstock [1984] Kinematics of present crust and mantle flow in southern California, Geol. Soc. Am. Bull., 95, 946-957.

Bird, P., Z. Liu, and W. K. Rucker [2008] Stresses that drive the plates from below: Definitions, computational path, model optimization, and error analysis, J. Geophys. Res., 113(B11), B11406, doi: 10.1029/2007JB005460.

Black, N. [2008] Fault length, multi-fault rupture, and relations to California earthquakes, 167 pages.

Boness, N. L., and M. D. Zoback [2006] Mapping stress and structurally controlled crustal shear anisotropy in California, Geology, 34(10), 825-828, doi:10.1130/G22309.1.

Bos, A. G., and W. Spakman [2005] Kinematics of the southwestern U.S. deformation zone inferred from GPS motion data, J. Geophys. Res., 110(B8), B08405, doi: 10.1029/2003JB002742.

Briggs, R. W., and S. G. Wesnousky [2004] Late Pleistocene fault slip rate, earthquake recurrence, and recency of slip along the Pyramid Lake fault zone, northern Walker Lane, Nevada, J. Geophys. Res., 109(B8), B08402, doi:10.1029/2003JB002717.

Bruner, W. M. [1984] Crack growth during unroofing of crustal rocks: Effects on thermoelastic behavior and near-surface stresses, J. Geophys. Res., 89(B6), 4167-4184.

Buesch, D. C., and P. L. Ehlig [1982] Structural and lower Miocene volcanic rock correlation between Soledad Pass and Salton Wash along the San Andreas fault (abstract), Geol. Soc. Am. Abstr. Prog., 14, 153.

Caskey, S. J., J. W. Bell, and S. G. Wesnousky [2004] Historic surface faulting and paleoseismicity in the area of the 1954 Rainbow Mountain-Stillwater earthquake sequence, Bull. Seismol. Soc. Am., 94, 1255-1275, doi: 10.1785/012003012.

Chadwell, C. D., and F. N. Spiess [2008] Plate motion at the ridge-transform boundary of the south Cleft segment of the Juan de Fuca Ridge from GPS-Acoustic data, J. Geophys. Res., 113(B4), B04415, doi: 10.1029/2007JB004936.

Chaytor, J. D., C. Goldfinger, R. D. Dziak, and C. G. Fox [2004] Active deformation of the Gorda plate: Constraining deformation models with new geophysical data, Geology, 32(4), 353-356.

Chaytor, J. D., C. Goldfinger, M. A. Meiner, G. J. Huftile, C. G. Romsos, and M. R. Legg [2008] Measuring vertical tectonic motion at the intersection of the Santa Cruz-Catalina Ridge and Northern Channel Islands platform, California continental borderland, using submerged paleoshorelines, Geol. Soc. Am. Bull., 120(7/8), 1053-1071, doi: 10.1130/B26316.1.

Christiansen, R. L., and R. S. Yeats [1992] Post-Laramide geology of the U.S. Cordilleran region, in: B. C. Burchfiel, P. W. Lipman, and M. L. Zoback (ed.), The Cordilleran Orogen: Conterminous U.S., The Geology of North America, G-3, 261-406.

Clark, M. N. [1979] Quaternary faulting in southern California, Summaries of Technical Reports, National Earthquake Hazards Reduction Program, U.S. Geol. Surv. Open-File Rep., 8, 16-17.

d'Alessio, M. A., I. A. Johnson, R. Burgmann, D. A. Schmidt, and M. H. Murray [2005] Slicing up the San Francisco Bay area: Block kinematics and fault slip rates from GPS-derived surface velocities, J. Geophys. Res., 110(B6), B06403, doi: 10.1029/2004JB003496.

DeMets, C., R. G. Gordon, D. F. Argus, and S. Stein [1990] Current plate motions, Geophys. J. Int., 101, 425-478.

DeMets, C., R. G. Gordon, D. F. Argus, and S. Stein [1994] Effect of recent revisions to the geomagnetic reversal time scale on estimate of current plate motions, Geophys. Res. Lett., 21(20), 2191-2194.

dePolo, C. M. [1998] A reconnaissance technique for estimating the slip rates of normal-slip faults in the Great Basin, and application to faults in Nevada, U.S.A., Ph.D. dissertation, U. Nevada Reno, 381 pages.

Dolan, J. F. [2007] Long-range and long-term fault interactions in southern California, Geology, 35(9), 855-858, doi: 10.1130/G23789A.1.

Dolan, J. F., K. Sieh, T. K. Rockwell, P. Guptill, and G. Miller [1997] Active tectonics, paleoseismology, and seismic hazards of the Hollywood fault, northern Los Angeles basin, California, Geol. Soc. Am. Bull., 109(12), 1595-1616.

Dolan, J. F., S. A. Christofferson, and J. H. Shas [2003] Recognition of paleoearthquakes on the Puente Hills blind thrust fault, California, Science, 300(4 April), 115-118.

Dooling, P. R., L. A. Leon, J. F. Dolan, J. H. Shaw, T. L. Pratt, and A. U. Martinez [2008] New late Pleistocene and Holocene slip rates on the southern segment of the Compton blind-thrust fault, Lakewood, California (abstract), Proceedings and Abstracts, 18, 154-155, Southern California Earthquake Center, Los Angeles.

Ehlert, K. W., and P. L. Ehlig [1977] The polka-dot granite and the rate of displacement on the San Andreas fault in southern California (abstract), Geol. Soc. Am. Abstr. Prog., 9, 415-416.

Faulds, J. E., C. D. Henry, and N. H. Hinz [2005] Kinematics of the northern Walker Lane: An incipient transform fault along the Pacific-North America plate boundary, Geology, 33(6), 505-508, doi: 10.1130/G21274.1.

Fenton, C. R., R. H. Webb, P. A. Pearthree, T. E. Cerling, and R. J. Poreda [2001] Displacement rates on the Toroweap and Hurricane faults: Implications for Quaternary downcutting in the Grand Canyon, Arizona, Geology, 29(11), 1035-1038.

Field, E. H. [2007] Overview of the Working Group for the Development of Regional Earthquake Likelihood Models (RELM), in: S. E. Hough and K. B. Olsen (ed.), Special Issue on: Regional Earthquake Likelihood Models, Seismol. Res. Lett., 78(1), 7-16.

Flesch, L. M., W. E. Holt, A. J. Haines, L. Wen, and B. Shen-Tu [2007] The dynamics of western North America: Stress magnitude and the relative role of gravitational potential energy, plate interaction at the boundary, and basal tractions, Geophys. J. Int., 169, 866-896, doi: 10.1111/j.1365-246X.2007.03274.x.

Fletcher, K. E., W. D. Sharp, and T. K. Rockwell [2008] Long-term slip rates of the Elsinore-Laguna Salada fault, southern California, by U-series dating of pedogenic carbonate in progressively offset alluvial fan remnants (abstract), Proceedings and Abstracts, 18, 167-168, Southern California Earthquake Center, Los Angeles.

Flodin, E. A., and A. Aydin [2004] Evolution of a strike-slip fault network, Valley of Fire State Park, southern Nevada, Geol. Soc. Am. Bull., 116(1/2), 42-59.

Frankel, A., C. Mueller, T. Barnhard, D. Perkins, E. V. Leyendecker,N. Dickman, S. Hanson, and M. Hoper [1996] National seismic-hazard maps: Documentation June 1996, U.S. Geol. Surv. Open-File Rep., 96-532, 110 pages.

Frankel, A. D., M. D. Petersen, C. S. Mueller, K. M. Haller, R. L. Wheeler, E. V. Leyendrecker, R. L. Wesson, S. C. Hamsen, C. H. Cramer, D. M. Perkins, and K. S. Rukstales [2002] Documentation for the 2002 update of the National Seismic Hazard Maps, U.S. Geol. Surv. Open-File Report, 02-420, 33 pages.

Frankel, K. L., K. S. Brantley, J. F. Dolan, R. C. Finkel, R. E. Klinger, J. R. Knott, M. N. Machette, L. A. Owen, F. M. Phillips, J. L. Slate, and B. P. Wernicke [2007] Cosmogenic ^{10}Be and ^{36}Cl geochronology of offset alluvial fans along the northern Death Valley fault zone: Implications for transient strain in the eastern California shear zone, J. Geophys. Res., 112(B6), B06407, doi: 10.1029/2006JB004350.

Friedrich, A. M., J. Lee, B. P. Wernicke, and K. Sieh [2004] Geologic context of geodetic data across a Basin and Range normal fault, Crescent Valley, Nevada, Tectonics, 23(2), TC2015, doi: 10.1029/2003TC001528.

Frizzell, V. A., Jr., J. M. Mattinson, and J. C. Matti [1986] Distinctive Triassic megaporphyritic monzogranite: Evidence for only 160 km offset along the San Andreas fault, southern California, J. Geophys. Res., 91(B14), 14,080-14,088.

Goldfinger, C., L. D. Kulm, R. S. Yeats, B. Applegate, M. E. MacKay, and G. F. Moore [1992] Transverse structural trends along the Oregon convergent margin: Implications for Cascadia earthquake potential and crustal rotations, Geology, 20(2), 141-144.

Gonzalez-Garcia, J. J., L. Prawirodirdjo, Y. Bock, and D. Agnew [2003] Guadalupe Island, Mexico as a new constraint for Pacific plate motion, Geophys. Res. Lett., 30(16), 1872, doi: 10.1029/2003GL017732.

Gratz, A. J. [1991] Solution-transfer compaction of quartzites: progress toward a rate law, Geology, 19(9), 901-904.

Guest, B., N. Niemi, and B. Wernicke [2007] Stateline fault system: A new component of the Miocene-Quaternary Eastern California shear zone, Geol. Soc. Am. Bull., 119(11/12), 1337-1346, doi: 10.1130/B26138.1.

Gulick, S. P. S., and S. Meltzer, T. J. Henstock, and A. Levander [2001] Internal deformation of the southern Gorda plate: Fragmentation of a weak plate near the Mendocino triple junction, Geology, 29(8), 691-694.

Haines, A. J., and W. E. Holt [1993] A procedure for obtaining the complete horizontal motions within zones of distributed deformation from the inversion of strain rate data, J. Geophys. Res., 98(B7), 12,057-12,082.

Haines, A. J., J. A. Jackson, W. E. Holt, and D. C. Agnew [1998] Representing distributed deformation by continuous velocity fields, Sci. Rept., 98/5

Haller, K. M., R. L. Wheeler, K. S. Rukstales [2002] Documentation of changes in fault parameters for the 2002 National Seismic Hazard Maps - Conterminous United States except California, U.S. Geol. Surv. Open-File Rep., 02-467, 34 pages.

Hammond, W. C., and W. Thatcher [2005] Northwest Basin and Range tectonic deformation observed with the Global Positioning System, 1999-2003, J. Geophys. Res., 110(B10), B10405; doi:10.1029/2005JB003678.

Hanks, T. C., and R. E. Wallace [1985] Morphological analysis of the Lake Lahontan shoreline and Beachfront fault scarps, Pershing County, Nevada, Bull. Seismol. Soc. Am., 75, 835-846.

Hauksson, E., and P. Shearer [2005] Southern California hypocenter relocation with waveform cross-correlation, Part 1: Results using the double-difference method, Bull. Seismol. Soc. Am., 95(3), 896-903, doi:10.1785/0120040167.

Hearn, E. H., and E. D. Humphreys [1998] Kinematics of the southern Walker Lane Belt and motion of the Sierra Nevada block, California, J. Geophys. Res., 103(B11), 27,033-27,049.

Henstock, T. J., and A. Levander [2003] Structure and seismotectonics of the Mendocino triple junction, California, J. Geophys. Res., 108(B5), 2260, ESE-12, doi: 10.1029/2001JB000902.

Ingersoll, R. V., and P. E. Rumelhart [1999] Three-stage evolution of the Los Angeles basin, southern California, Geology, 27(7), 593-596.

Jennings, C. W. [1994] Fault activity map of California and adjacent regions, with locations and ages of Recent volcanic eruptions, scale 1:750,000, with Explanatory Text, Geol. Data Map, 6, 92 pages plus map.

Johnson, K. M., G. E. Hilley, and R. Burgmann [2007] Influence of lithosphere viscosity structure on estimates of fault slip rate in the Mojave region of the San Andreas fault system, J. Geophys. Res., 112(B7), B07408, doi: 10.1029/2006JB004842.

Johnson, S. Y., S. V. Dadisman, J. R. Childs, and W. D. Stanley [1999] Active tectonics of the Seattle fault and central Puget Sound, Washington: Implications for earthquake hazards, Geol. Soc. Am. Bull., 111(7), 1042-1053.

Johnson, S. Y., R. J. Blakely, W. J. Stephenson, W. V. Dadisman, and M.A. Fischer [2004] Active shortening in the Cascadia forearc and implications for seismic hazards of Puget Sound, Tectonics, 23(1), TC1011, dot:10.1029/2003TC001507.

Kelsey, H. M., B. Sherrod, S. Y Johnson, and S. V. Dadisman [2004] Land-level changes from a late Holocene earthquake in the northern Puget Lowland, Washington, Geology, 32(6), 469-472, doi: 10.1130/G20361.1.

Kogan, M. G., and G. M. Steblov [2008] Current global plate kinematics from GPS (1995-2007) with the plate-consistent reference frame, J. Geophys. Res., 113(B4), B04416, doi: 10.1029/2007JB005353.

Kong, X., and P. Bird [1995] SHELLS: A thin-plate program for modeling neotectonics of regional or global lithosphere with faults, J. Geophys. Res., 100(B11), 22,129-22,131.

Lawrence, R. D. [1976] Strike-slip faulting terminates the Basin and Range province in Oregon, Geol. Soc. Am. Bull., 87(6), 846-850.

Le, K., J. Lee, L. A. Owen, and R. Finkel [2007] Late Quaternary slip rates along the Sierra Nevada frontal fault zone, California: Slip partitioning across the western margin of the eastern California shear zone-Basin and Range province, Geol. Soc. Am. Bull., 119(1/2), 240-256, doi: 10.1130/B25960.

Lee, J., C. M. Rubin, and A. Calvert [2001a] Quaternary faulting history along the Deep Springs fault, California, Geol. Soc. Am. Bull., 113(7), 855-869.

Lee, J., J. Spencer, and L. Owen [2001b] Holocene slip rates along the Owens Valley fault, California: Implications for the recent evolution of the Eastern California shear zone, Geology, 29(9), 819-822.

Leitner, B., A. M. Trehu, and N. J. Godfrey [1998] Crustal structure of the northwestern Vizcaino block and Gorda Escarpment, offshore northern California, and implications for postsubduction deformation of a paleoaccretionary margin, J. Geophys. Res., 103(B10), 23795-23812.

Liu, Z., and P. Bird [2008] Kinematic modelling of neotectonics in the Persia-Tibet-Burma orogen, Geophys. J. Int., 172(2), 779-797 + 3 digital appendices, doi: 10.1111/j.1365-246X.2007.03640.x.

Martel, S. J., T. M. Harrison, and A. R. Gillespie [1987] Late Quaternary vertical displacement rate across the Fish Springs fault, Owens Valley fault zone, California, Quaternary Research, 27, 113-129.

Matmon, A., D. P. Schwartz, R. Finkel, S. Clemmens, and T. Hanks [2005] Dating offset fans along the Mojave section of the San Andreas fault using cosmogenic ^{26}Al and ^{10}Be, Geol. Soc. Am. Bull., 117(5/6), 795-807.

Mattson, A., and R. L. Bruhn [2001] Fault slip rates and initiation age based on differential equation modeling: Wasatch fault zone and eastern Great Basin, J. Geophys. Res., 106(B7), 13739-13750.

McCaffrey, R. [2005] Block kinematics of the Pacific-North American plate boundary in the southwestern United States from inversion of GPS, seismological, and geologic data, J. Geophys. Res., 110(B7), B07401, doi:10.1029/2004JB003307.

McCrory, P. A. [2000] Upper plate contraction north of the migrating Mendocino triple junction, northern California: Implications for partitioning of strain, Tectonics, 19(6), 1144-1160.

McGill, S., and K. Sieh [1993] Holocene slip rate of the central Garlock fault in southeastern Searles Valley, California, J. Geophys. Res., 98(B8), 14,217-14,231.

McGill, S. F., R. J. Weldon, and L. A. Owen [2008] Preliminary slip rates along the San Bernardino strand of the San Andreas fault (abstract), Proceedings and Abstracts, 18, 165-166, Southern California Earthquake Center, Los Angeles.

McKenzie, D. P., and W. J. Morgan [1969] Evolution of triple junctions, Nature, 224, 125-133.

Meade, B. J., and B. H. Hager [2005] Block models of crustal motion in southern California constrained by GPS measurements, J. Geophys. Res., 110(B3), B03403, dot:10.1029/2004JB003209.

Meisling, K. E., and R. J. Weldon [1986] Cenozoic uplift of the San Bernardino Mountains: Possible thrusting across the San Andreas fault (abstract), Geol. Soc. Am. Abstr. Prog., 18(2), 157.

Meltzner, A. J., and T. K. Rockwell [2008] Late Holocene slip on the Imperial fault, Mesquite Basin, Imperial Valley, California (abstract), Proceedings and Abstracts, 18, 157, Southern California Earthquake Center, Los Angeles.

Myers, D. J., J. L. Nabalek, and R. S. Yeats [2003] Dislocation modeling of blind thrusts in the eastern Los Angeles

basin, California, J. Geophys. Res., 108(B9), 2443, ESE-14, doi: 10.1029/2002JB002150.

Nazareth, J. J., and E. Hauksson [2004] The seismogenic thickness of the southern California crust, Bull. Seismol. Soc. Am., 94(3), 940-960.

Numelin, T., E. Kirby, J. D. Walker, and B. Didericksen [2007] Late Pleistocene slip on a low-angle normal fault, Searles Valley, California, Geosphere, 3(3), 163-176, doi: 10.1130/GES00052.1.

Onderdonk, N. W., S. A. Minor, and K. S. Kellogg [2005] Taking apart the Big Pine fault: Redefining a major structural feature in southern California, Tectonics, 24(6), TC6002, doi: 10.1029/2005TC001817.

Oskin, M., and A. Iriondo [2004] Large-magnitude transient strain accumulation on the Blackwater fault, Eastern California shear zone, Geology, 32(4), 313-316, doi: 10.1130/G20223.1.

Oskin, M., L. Perg, E. Shelef, M. Strane, E. Gurney, D. Blumentritt, S. Mukhopadhyay, and A. Iriondo [2006] Geologic fault slip rates support transitory, elevated geodetic strain accumulation across the Mojave Desert, Eastern California shear zone (abstract), Eos Trans. AGU, 87(52), Fall Meeting Supplement, Abstract G43B-0992.

Oskin, M., L. Perg, D. Blumentritt, S. Mukhopadhyay, and A. Iriondo [2007] Slip rate of the Calico fault: Implications for geologic versus geodetic rate discrepancy in the Eastern California Shear Zone, J. Geophys. Res., 112(B3), B03402, doi: 10.1029/2006JB004451.

Parsons, T., G. A. Thompson, and R. P. Smith [1998] More than one way to stretch: A tectonic model for extension along the plume track of the Yellowstone hotspot and adjacent Basin and Range province, Tectonics, 17(2), 221-234.

Payne, S. J., R. McCaffrey, and R. W. King [2008] Strain rates and contemporary deformation in the Snake River Plain and surrounding Basin and Range from GPS and seismicity, Geology, 36(8), 647-650, doi: 10.1130/G25039A.1.

Pederson, J., K. Karlstrom, W. Sharp, and W. McIntosh [2002] Differential incision of the Grand Canyon related to Quaternary faulting: Constraints from U-series and Ar/Ar dating, Geology, 30(8), 739-742.

Personius, S. F., R. E. Anderson, K. Okumura, S. A. Mahan, and D. A. Hancock [2002] Preliminary paleoseismology of the Santa Rosa Range fault zone, Humboldt County, Nevada (abstract), Geol. Soc. Am. Abstr. Prog., 34(6), 27.

Personius, S. F., R. L. Dart, L.-A. Bradley, and K. M. Haller [2003] Map and data for Quarternary faults and folds in Oregon, U.S. Geol. Surv. Open-File Rep., 03-095 (version 1.0)

Petersen, M. D., A. D. Frankel, S. C. Harmsen, C. S. Mueller, K. M. Haller, R. L. Wheeler, R. L. Wesson, Y. Zeng, O. S. Boyd, D. M. Perkins, N. Luco, E. H. Field, C. J. Wills, and K. S. Rukstales [2008] Documentation for the 2008 update of the United States National Seismic Hazard Maps, U.S. Geol. Surv. Open-File Rep., 2008-1128

Pinter, N., S. B. Lueddecke, E. A. Keller, and K. R. Simmons [1998] Late Quaternary slip on the Santa Cruz Island fault, California, Geol. Soc. Am. Bull., 110(6), 711-722.

Pinter, N., C. C. Sorlien, and A. T. Scott [2003] Fault-related fold growth and isostatic subsidence, California Channel Islands, Am. J. Sci., 303(4), 300-318, doi: 10.2475/ajs.303.4.300.

Plesch, A., J. Shaw, C. Benson, W. A. Bryant, S. Carena, M. Cooke, J. Dolan, G. Fuis, E. Gath, L. Grant, E. Hauksson, T. Jordan, M. Kamerling, M. Legg, S. Lindvall, H. Magistrale, C. Nicholson, N. Niemi, M. Oskin, S. Perry, G. Planansky, T. Rockwell, P. Shearer, C. Sorlien, M. P. Suss, J. Suppe, J. Treiman, and R. S. Yeats [2007] Community Fault Model (CFM) for southern California, Bull. Seismol. Soc. Am., 97(6), 1793-1802; doi: 10.1785/0120050211.

Poirier, J.-P. [1985] Creep of Crystals, Cambridge University Press, 260 pages.

Pollitz, F. F., P. McCrory, J. Svarc, and J. Murray [2008] Dislocation models of interseismic deformation in the western United States, J. Geophys. Res., 113(B4), B04413, doi: 10.1029/2007JB005174.

Ramelli, A. R., J. W. Bell, C. M. dePolo, and J. C. Yount [1999] Large-magnitude late Holocene earthquakes on the Genoa fault, west-central Nevada and eastern California, Bull. Seismol. Soc. Am., 89, 1458-1472.

Reinecker, J., O. Heidbach, M. Tingay, P. Connolly, and B. Muller [2004] The 2004 release of the World Stress Map, available online at: http://www.world-stress-map.org .

Roy, M., and L. H. Royden [2000] Crustal rheology and faulting at strike-slip plate boundaries, 1. An analytic model, J. Geophys. Res., 105(B3), 5583-5597.

Rucker, W. K.Neotectonic kinematic analysis of Philippines orogen: Regional strain-rates and a forecast of long-term seismicity (abstract), Eos Trans. AGU, 89(53), Fall Meeting Suppl., Abstract T53D-1992.

Rust, D. [2005] Palaeoseismology in steep terrain: the Big Bend of the San Andreas fault, Transverse Ranges, California, Tectonophysics, 408, 193-205.

Saint-Amand, P., and G. R. Roquemore [1979] Tertiary and Holocene development of the southern Sierra Nevada

and Coso Range, California (abstract), Tectonophysics, 52, 409-410.

Salyards, S. L., K. E. Sieh, and J. L. Kirschvink [1992] Paleomagnetic measurement of nonbrittle coseismic deformation across the San Andreas fault at Pallett Creek, J. Geophys. Res., 97(B9), 12,457-12,470.

Sauber, J., W. Thatcher, S. C. Solomon, and M. Lisowski [1994] Geodetic slip rate for the eastern California shear zone and the recurrence time of Mojave Desert earthquakes, Nature, 367(20 Jan.), 264-266.

Saucier, F., and E. Humphreys [1993] Horizontal crustal deformation in southern California from joint models of geologic and very long baseline interferometry measurements, in: D. E. Smith and D. L. Turcotte (ed.), Contributions of Space Geodesy to Geodynamics: Crustal Dynamics, Geodyn. Ser., 23, 139-176.

Schwartz, D. P., and R. Weldon [1986] Late Holocene slip rate on the Mojave segment of the San Andreas fault, Littlerock, CA: Preliminary Results (abstract), Eos Trans. AGU, 67(44), 906.

Sella, G. F. [2002] REVEL: A model for Recent plate velocities from space geodesy, J. Geophys. Res., 107(B4), 2081, doi: 10.1029/2000JB000033.

Shaw, J. H., A. Plesch, J. F. Dolan, T. L. Pratt, and P. Fiore [2002] Puente Hills blind-thrust system, Los Angeles, California, Bull. Seismol. Soc. Am., 92(8), 2946-2960.

Shen-Tu, B., W. E. Holt, and A. J. Haines [1998] Contemporary kinematics of the western United States determined from earthquake moment tensors, very long baseline interferometry, and GPS observations, J. Geophys. Res., 103(B8), 18,087-18,117.

Shen-Tu, B., W. E. Holt, and A. J. Haines [1999] Deformation kinematics in the western United States determined from Quaternary fault slip rates and recent geodetic data, J. Geophys. Res., 104(B12), 28,927-28,955.

Sherrod, B. L., T. M. Brocher, C. S. Weaver, R. C. Bucknam, R. J. Blakely, H. M. Kelsey, A. R. Nelson, and R. Haugerud [2004] Holocene fault scarps near Tacoma, Washington, USA, Geology, 32(1), 9-12, doi: 10.1130/G19914.1.

Sieh, K. E. [1984] Lateral offsets and revised dates of large prehistoric earthquakes at Pallett Creek, southern California, J. Geophys. Res., 89(B9), 7641-7670.

Sieh, K. E., M. Stuiver, and D. Brillinger [1989] A more precise chronology of earthquakes produced by the San Andreas fault in southern California, J. Geophys. Res., 94(B1), 603-623.

Silver, E. A. [1971] Tectonics of the Mendocino triple junction, Geol. Soc. Am. Bull., 82, 2965-2978.

Smith, S. W., J. S. Knapp, and R. C. McPherson [1993] Seismicity of the Gorda plate, structure of the continental margin, and eastward jump of the Mendocino triple junction, J. Geophys. Res., 98(B5), 8153-8171.

Spotila, J. A., and K. E. Sieh [2000] Architecture of transpressional thrust faulting in the San Bernardino Mountains, southern California, from deformation of a deeply weathered surface, Tectonics, 19(4), 589-615.

Stewart, J. H. [1978] Basin-range structure in western North America, in: R. B. Smith and G. P. Eaton (ed.), Cenozoic Tectonics and Regional Geophysics of the Western Cordillera, Geol. Soc. Am. Mem., 152, 1-32.

Stewart, J. H. [1998] Regional characteristics, tilt domains, and extensional history of the late Cenozoic Basin and Range province,western North America, in: J. E. Faulds and J. H. Stewart (ed.), Accomodation Zones and Transfer Zones: The Regional Segmentation of the Basin and Range Province, Geol. Soc. Am. Mem., 323, 47-74.

Swan, F. H., III, K. L. Hanson, and M. M. Angell [2004] Paleoseismic investigations of the Stansbury and mid-valley faults, Skull Valley, Utah, in: W. Lund (ed.), Proceedings Volume Western States Seismic Policy Council, Basin and Range Province Seismic Hazards Summit II, 20 pages.

Tweto, O. [1979] The Rio Grande rift system in Colorado, in: R. E. Riecker (ed.), Rio Grande Rift: Tectonics and Magmatism, 33-56.

Unruh, J. R., and W. R. Lettis [1998] Kinematics of transpressional deformation in the eastern San Francisco Bay region, California, Geology, 26(1), 19-22.

Walker, G. W. [1977] Geologic map of Oregon east of the 121st meridian, U.S. Geol. Surv. Misc. Geol. Invest., I-902, 2 sheets, 1:500,000.

Weldon, R., T. Fumal, and G. Biassi [2004] Wrightwood and the earthquake cycle: What a long recurrence record can tell us about how faults work, GSA Today, 14(9), doi:10.1130/1052-5173(2004)014<4:WATECW>2.0.CO;2.

Weldon, R. J., II, T. E. Fumal, T. J. Powers, S. K. Pezzopane, K. M. Scharer, and J. C. Hamilton [2002] Structure and earthquake offsets at the Wrightwood, California, paleoseismic site, Bull. Seismol. Soc. Am., 92(7), 2704-2725.

Weldon, R. J., K. M. Scharer, R. R. Sickler, A. H. Pruitt, C. L. Gilleland, and J. Garroway [2008] Slip rate site on the San Andreas fault near Littlerock, CA (abstract), Proceedings and Abstracts, 18, 167, Southern California Earthquake Center, Los Angeles.

Werner, M. J. [2007] On the fluctuations of seis\micity and uncertainties in earthquake catalogs: Implications and

methods for hypothesis testing, 340 pages.

Wesnousky, S. G. [2005] Active faulting in the Walker Lane, Tectonics, 24(3), TC3009, doi: 10.1029/2004TC001645.

Wesnousky, S. G. [2006] Predicting the endpoints of earthquake ruptures, Nature, 444, 358-360.

Wesnousky, S. G., and C. H. Willoughby [2003] Neotectonic note: The Ruby-East Humboldt Range, northeastern Nevada, Bull. Seismol. Soc. Am., 93, 1345-1354.

Wesnousky, S. G., A. D. Barron, R. W. Briggs, S. J. Caskey, S. Kumar, and L. Owen [2005] Paleoseismic transect across the northern Great Basin, USA, J. Geophys. Res., 110(B5), B05408, doi:10.1029/2004JB003283.

Wilson, D. S. [1988] Tectonic history of the Juan de Fuca Ridge over the last 40 million years, J. Geophys. Res., 93(B10), 11,863-11,876.

Working Group on California Earthquake Probabilities [2003] Earthquake probabilities in the San Francisco Bay region: 2002-2031, U.S. Geol. Surv. Open-File Rep., 03-214, 235 pages.

Figures
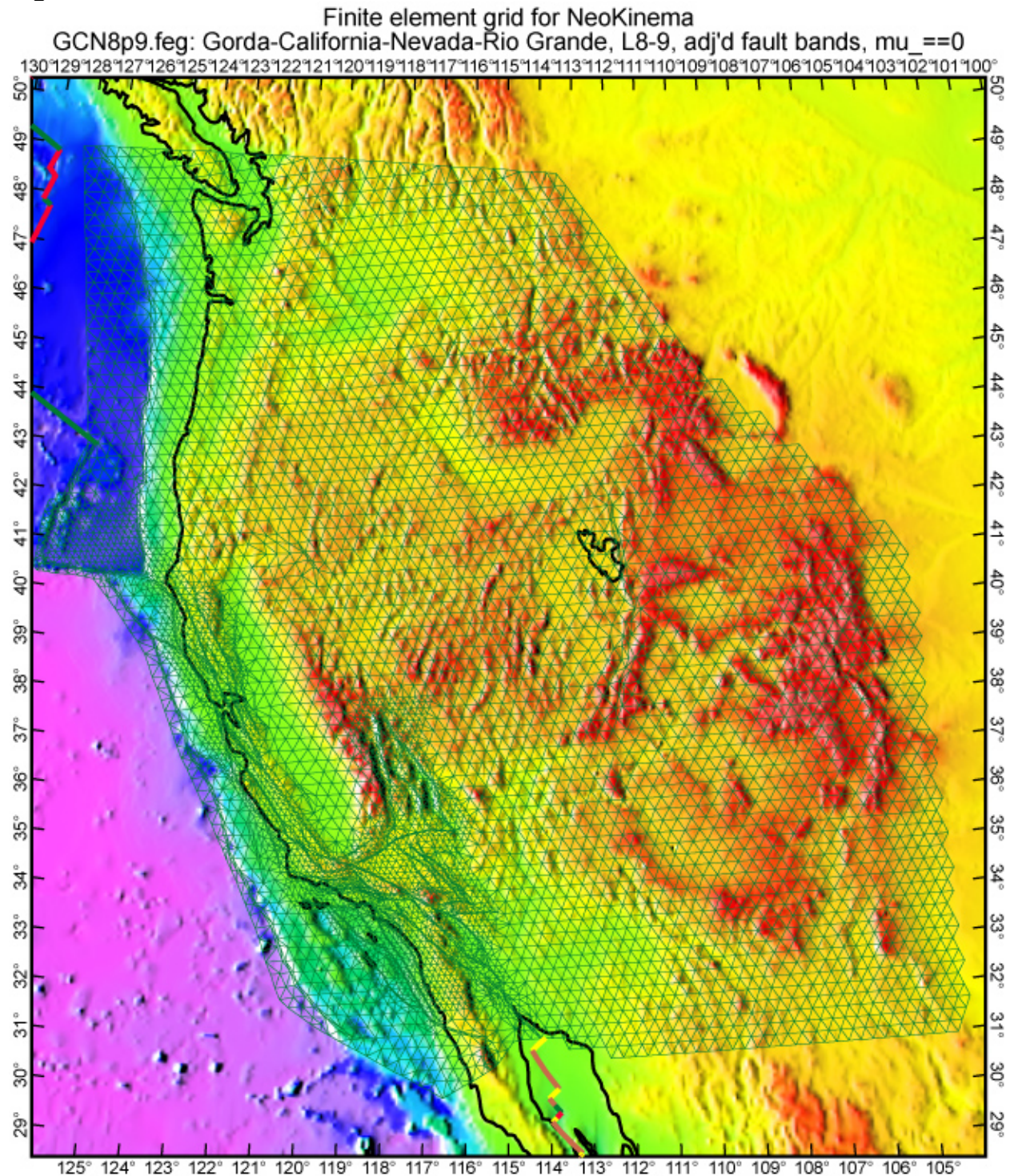
Figure 1. Finite element grid GCN8p9.feg used in this study. Most of the grid is composed of quasi-equilateral spherical triangles, with sides of either 30 km (coarse regions) or 15 km (fine regions). Ribbons of smaller elements, with width approximately 4 km, have been inserted along most fast-slipping faults, to better approximate the expected velocity discontinuities. There are 6452 nodes and 12627 elements.
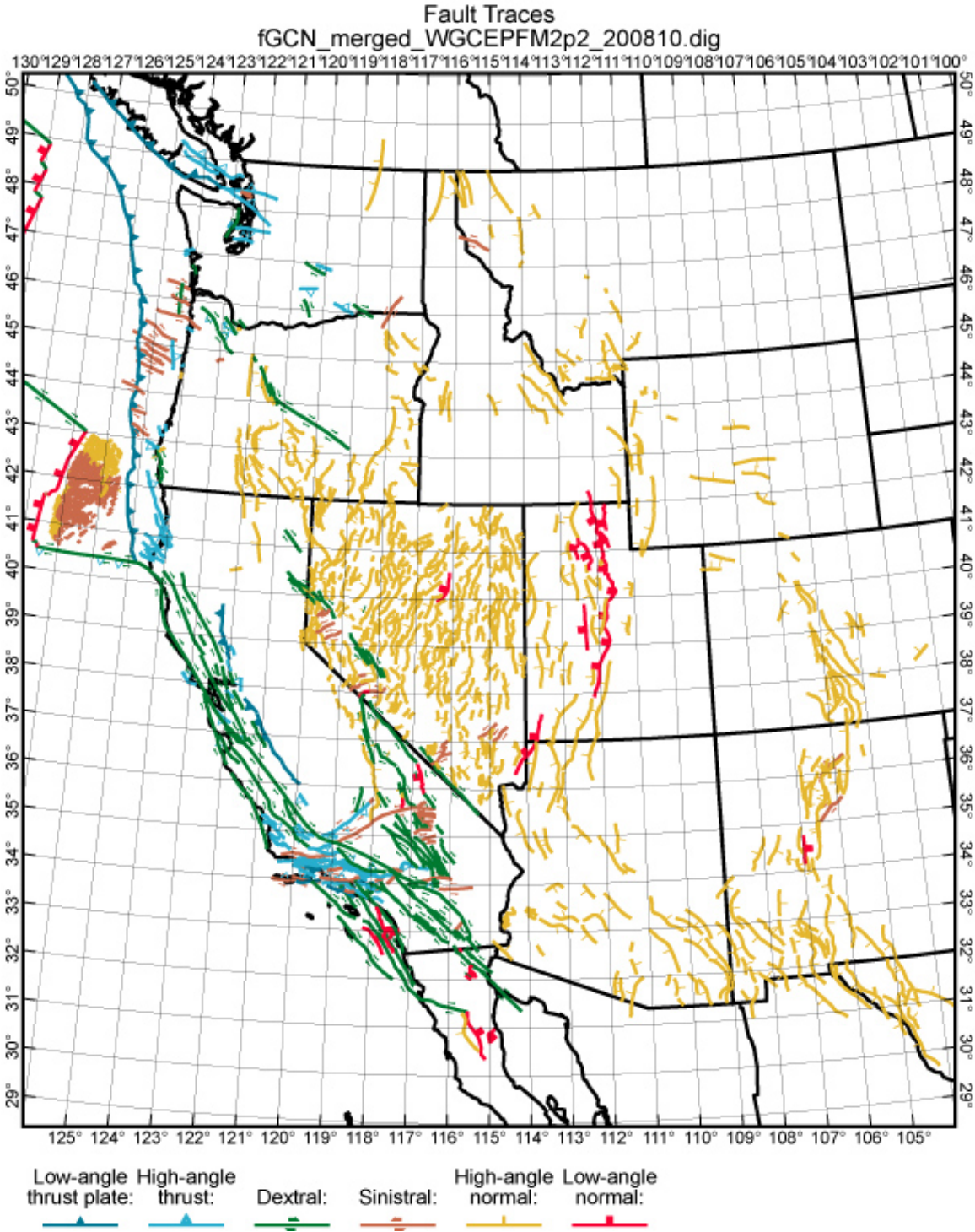
Figure 2. Traces of 1472 active and potentially-active faults included in these models. Traces are colored according to prior expectations of their predominant sense(s) of slip. Faults with oblique slip have a green or brown trace to indicate dextral or sinistral component, plus dip-ticks of a different colors and shapes to indicate the primary mode of dip-slip. Offset type D is used for both low-angle detachment faults and magmatic spreading centers.
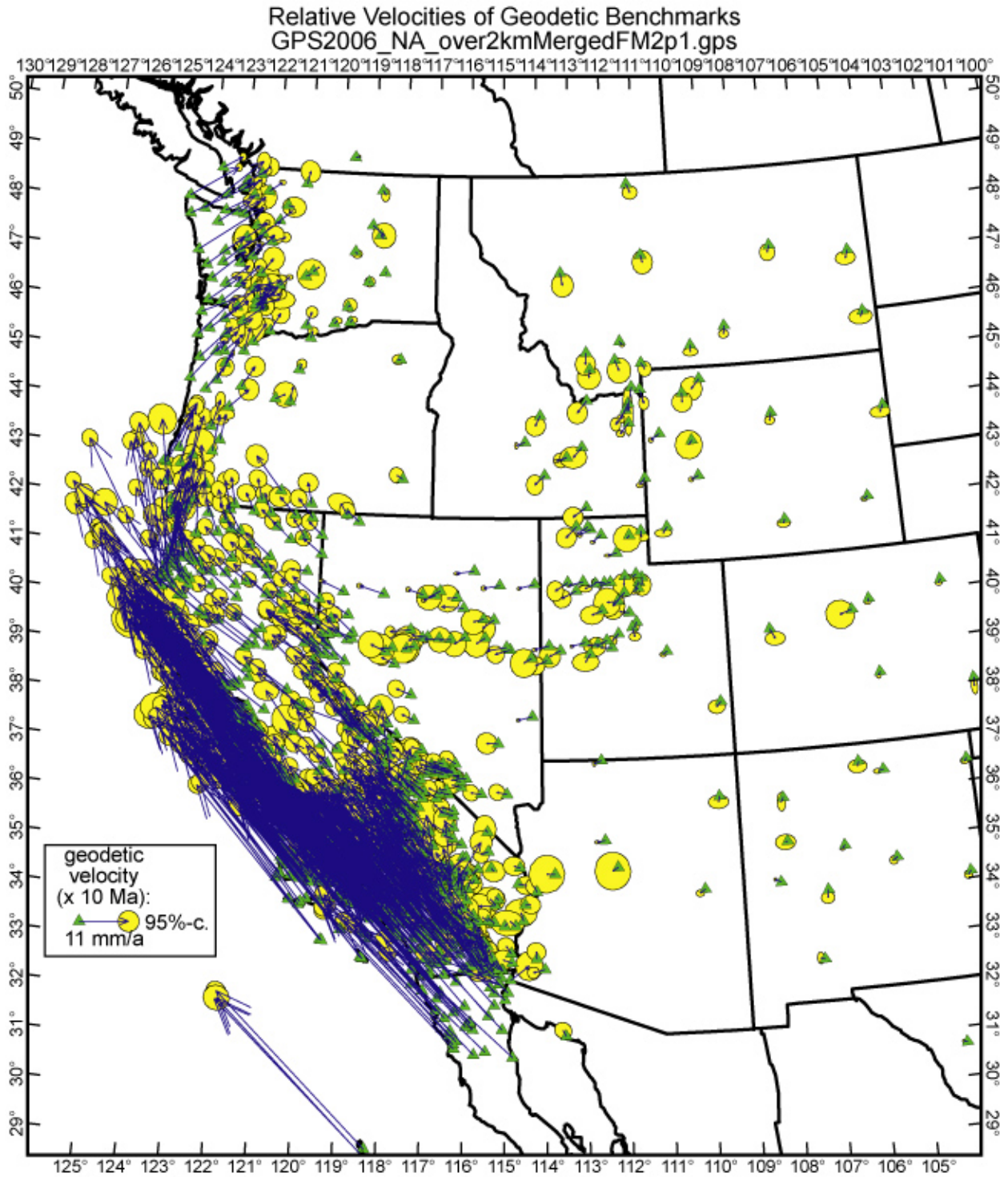
Figure 3. GPS benchmarks, interseismic velocities, and 95%-confidence ellipses used in modeling. As described in text, California velocities are from a 2006 solution by Shen and others for WGCEP; velocities outside California are selected from the PBO solution of September 2007. All velocities are in the stable North America reference frame.
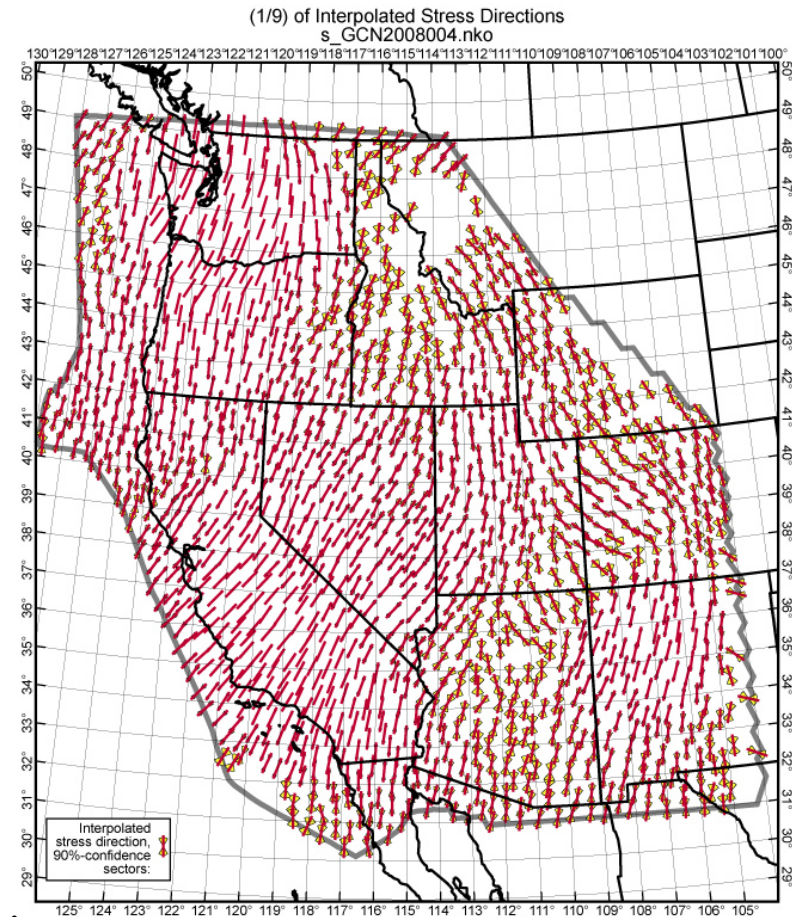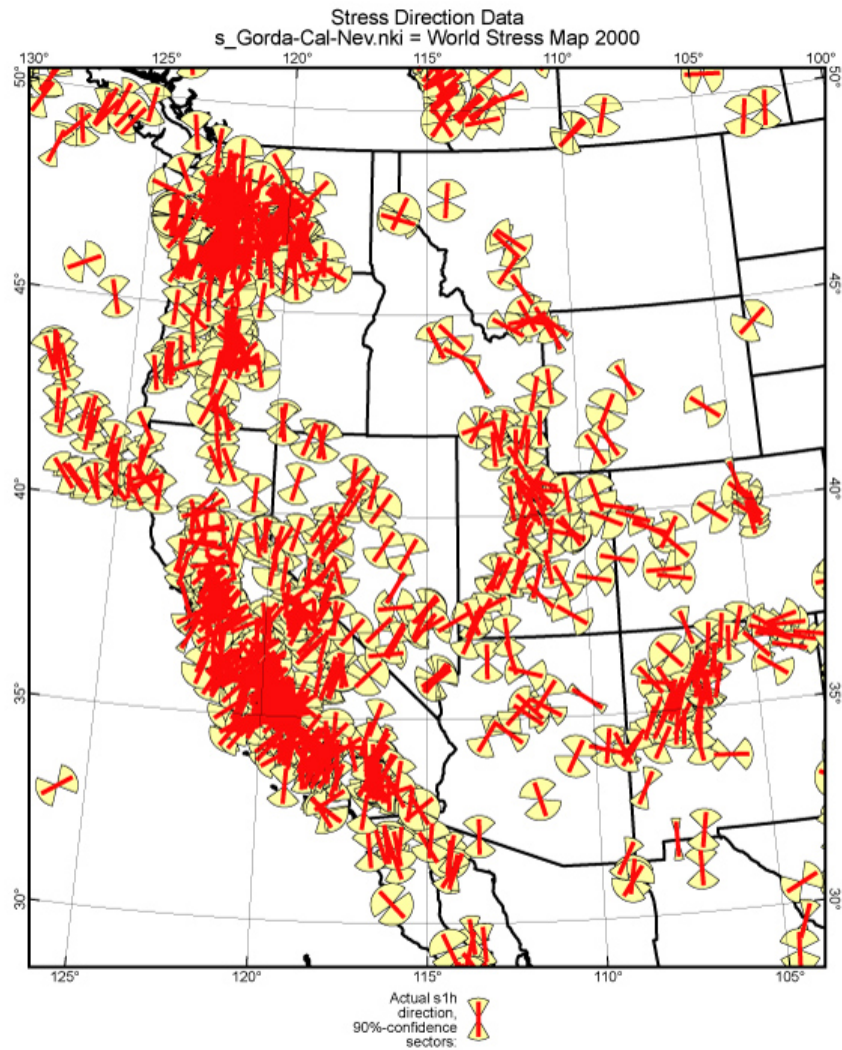
Figure 4. Data on the azimuth of the most-compressive horizontal principal stress from the World Stress Map (A), and directions interpolated by NeoKinema (B) using the clustered-data algorithm of *Bird & Li* [1996].
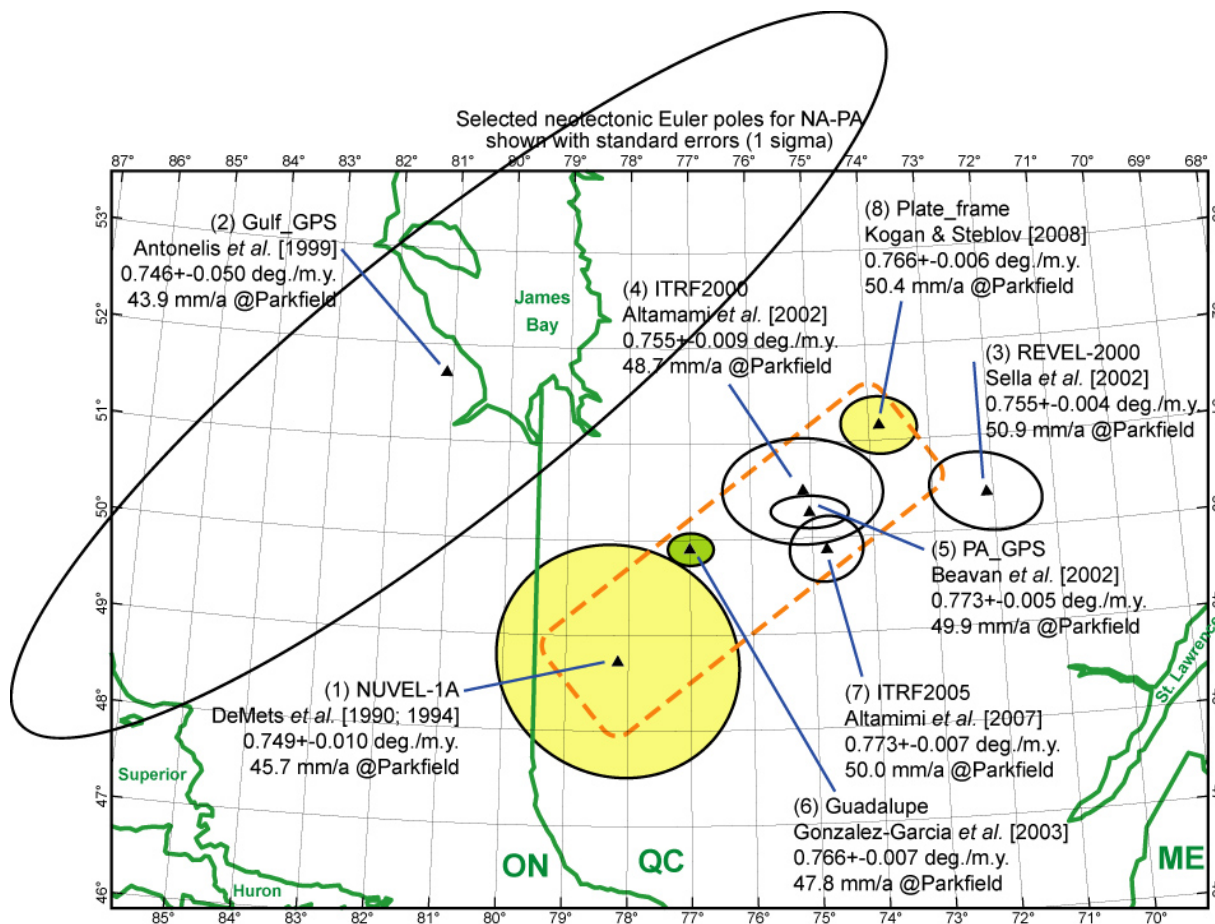
Figure 5. Neotectonic Euler poles for relative rotation of North America (NA) with respect to Pacific (PA). The error ellipses shown are standard errors, so 95%-confidence ranges have twice the diameters shown, and typically overlap. For each pole, a label indicates the implied NA-PA relative velocity at Parkfield, CA (assuming that stable NA and PA lithosphere extend up to the San Andreas fault at that point, whereas actually they do not). Poles within the dashed rectangle were used in NeoKinema modeling; others are shown for historical interest. The Gulf_GPS pole was not explicitly stated by *Antonelis et al.* [1999] but was computed by the author from their velocity vectors.
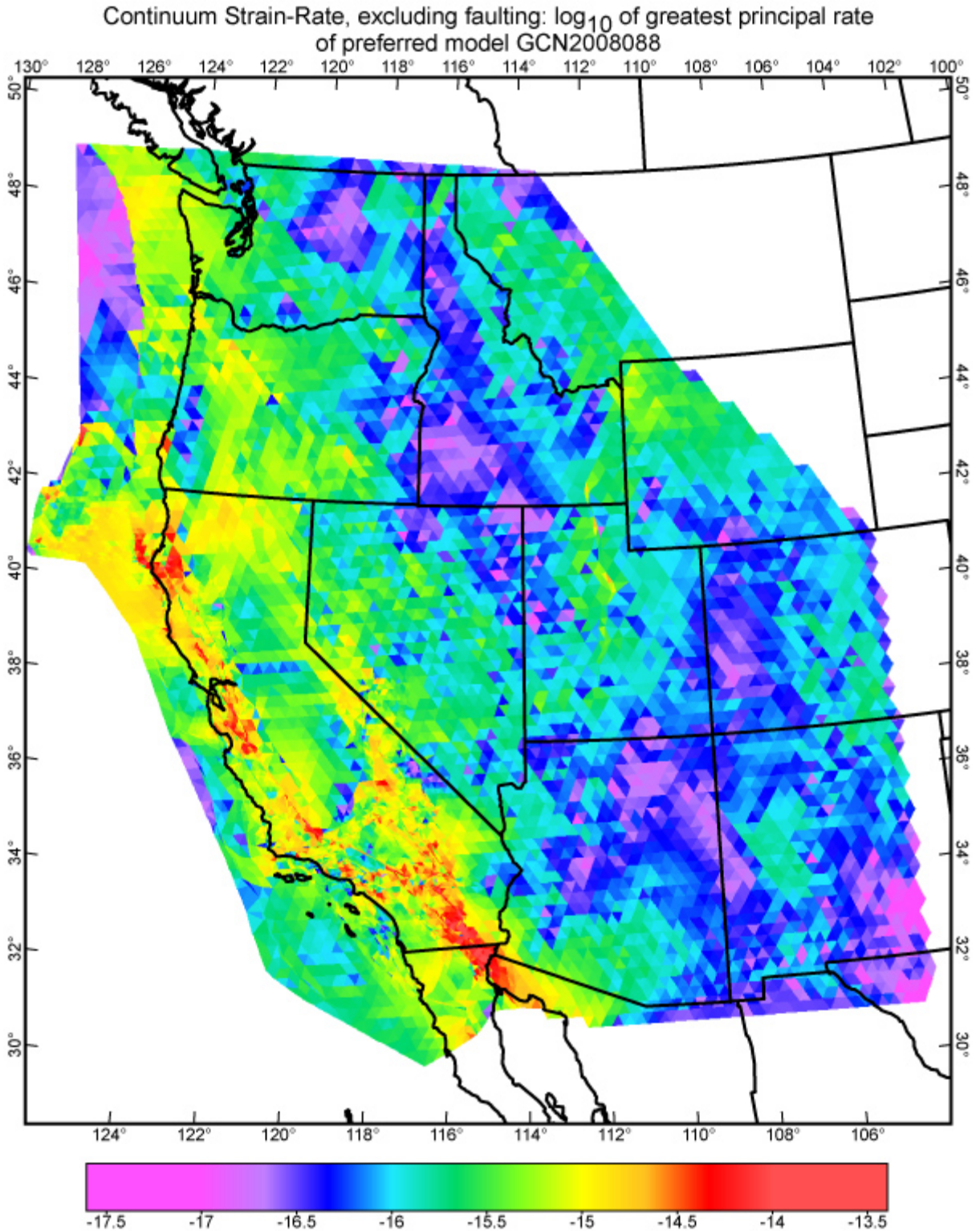
Figure 6. Common logarithms of distributed anelastic deformation rates (excluding strain-rates due to slip on modeled faults) in the preferred model GCN2008088. See equation (5) for definition of scalar measure.
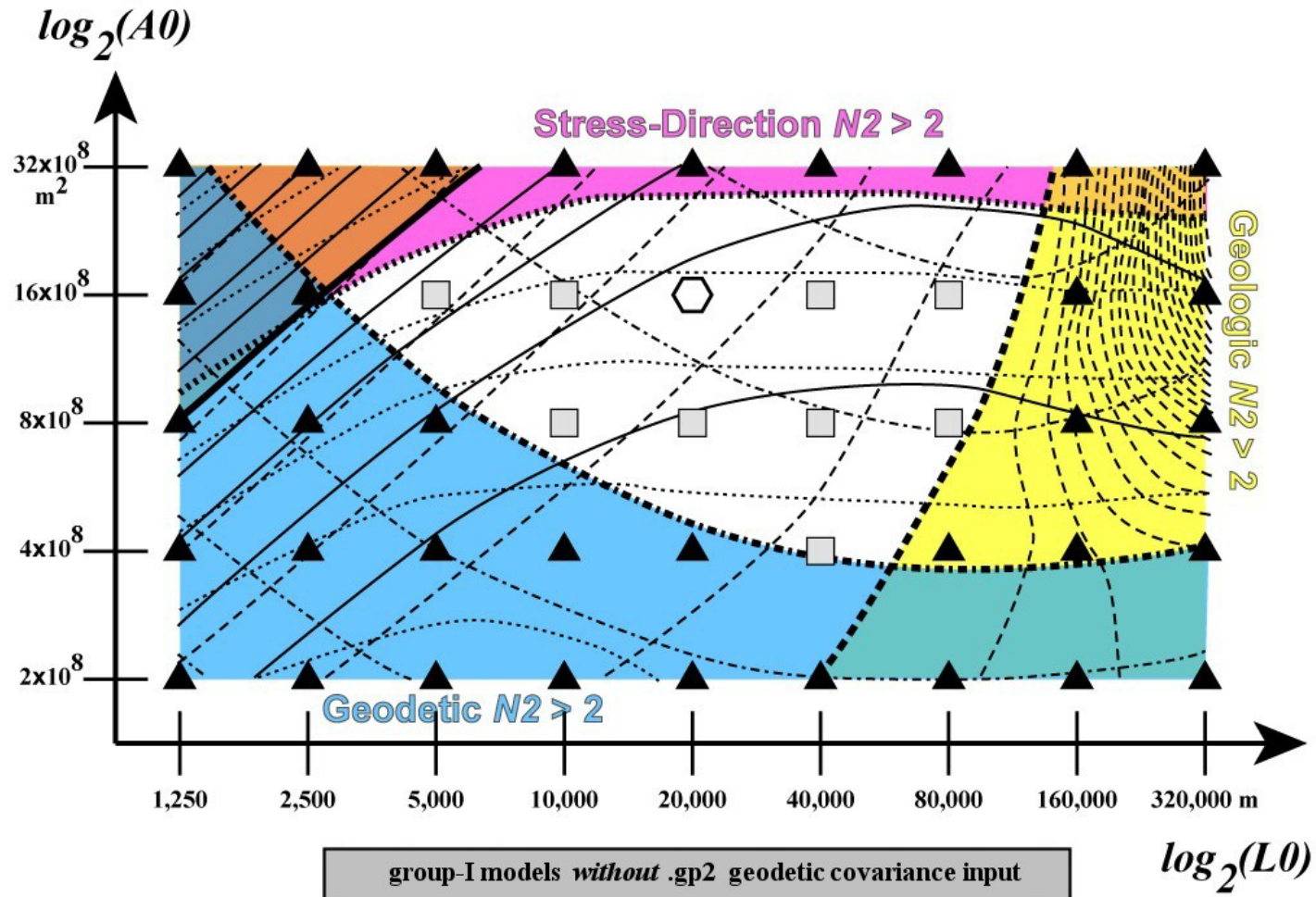
Figure 7. Three misfit measures (N_2^{geodetic} , N_2^{potency} , N_2^{stress}) are contoured in a 2-D parameter space with axes of $\log_2(L_0)$ and $\log_2(A_0)$. Contour interval 0.2, with heavier lines at value 2.0, and colored shading to show regions of unacceptable misfit (any $N_2 > 2$). Acceptable models are shown by rectangles and octagon, while unacceptable models are shown by triangles. All computations used prior/input $\mu = 5 \times 10^{-16}$, Fault Model 2.1, NUVEL-1A pole, and block-diagonal approximation of the geodetic covariance.
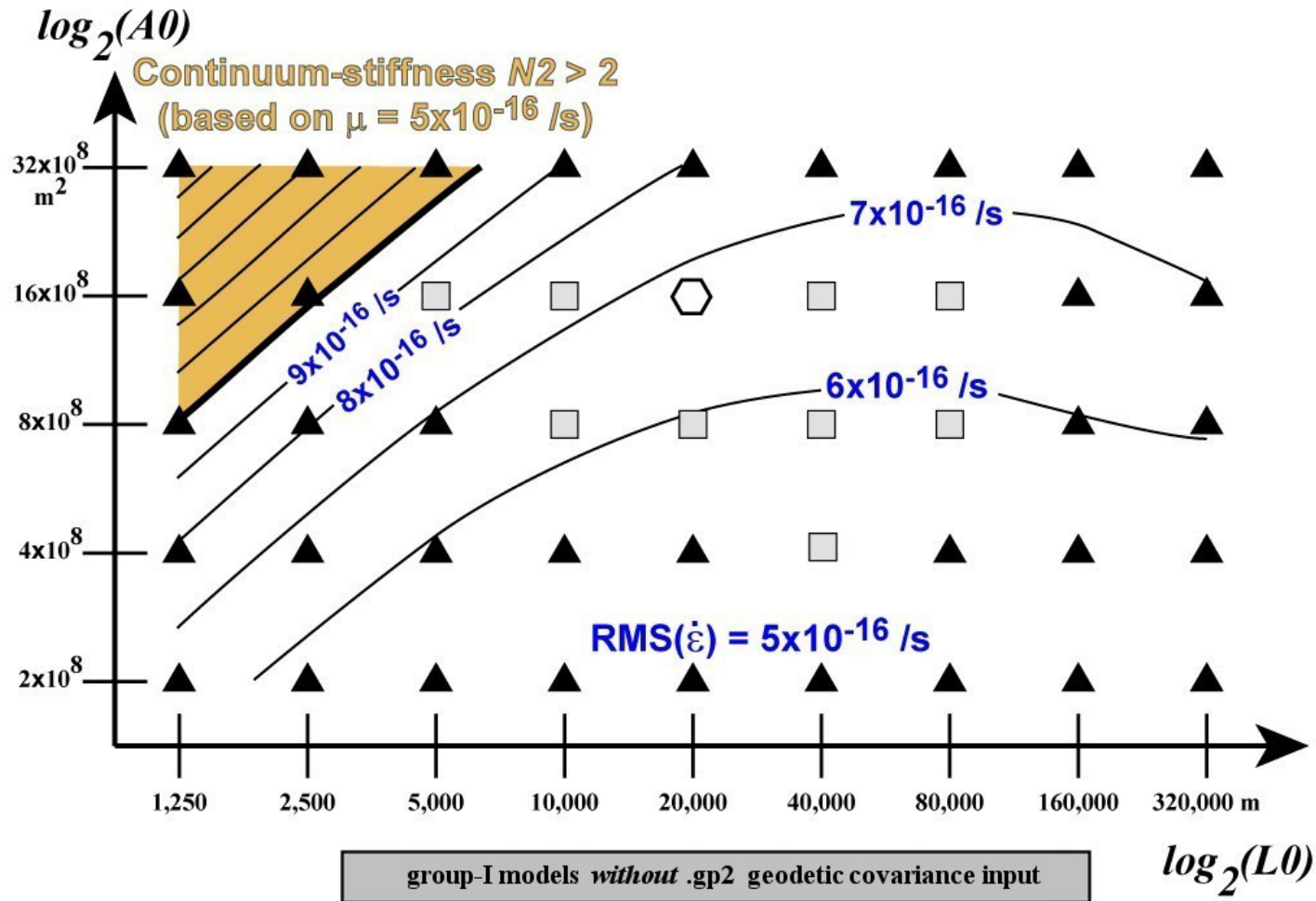
Figure 8. Posterior/output values of RMS distributed deformation rate (μ^*) shown with contours in the same 2-D parameter space as Figure 7. All inputs as in Figure 7. Acceptable models (with all misfit measures < 2) are shown by rectangles and octagon, while unacceptable models are shown by triangles.
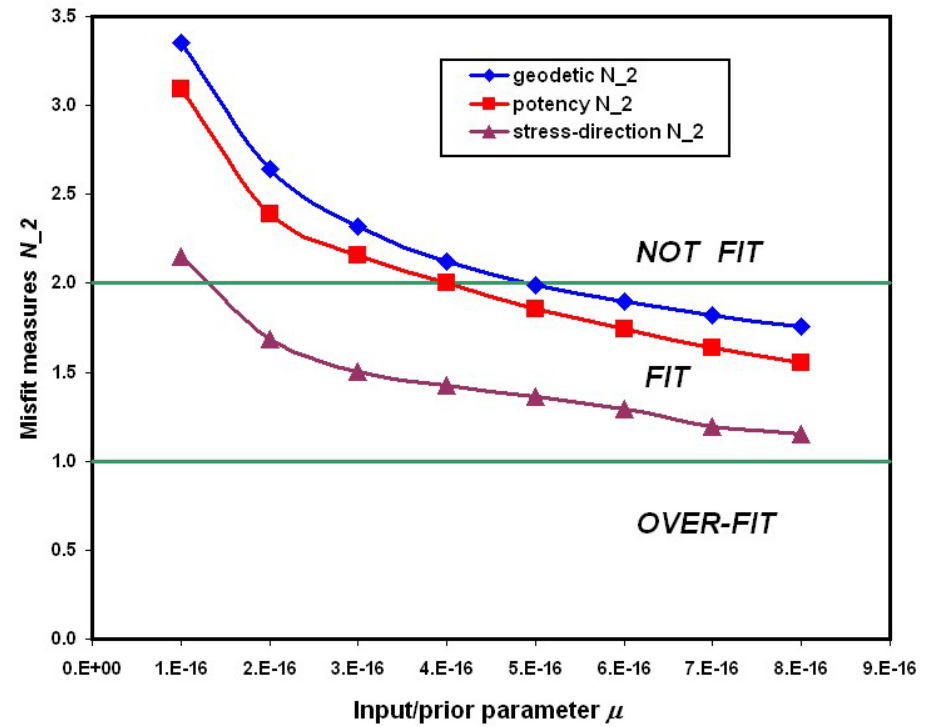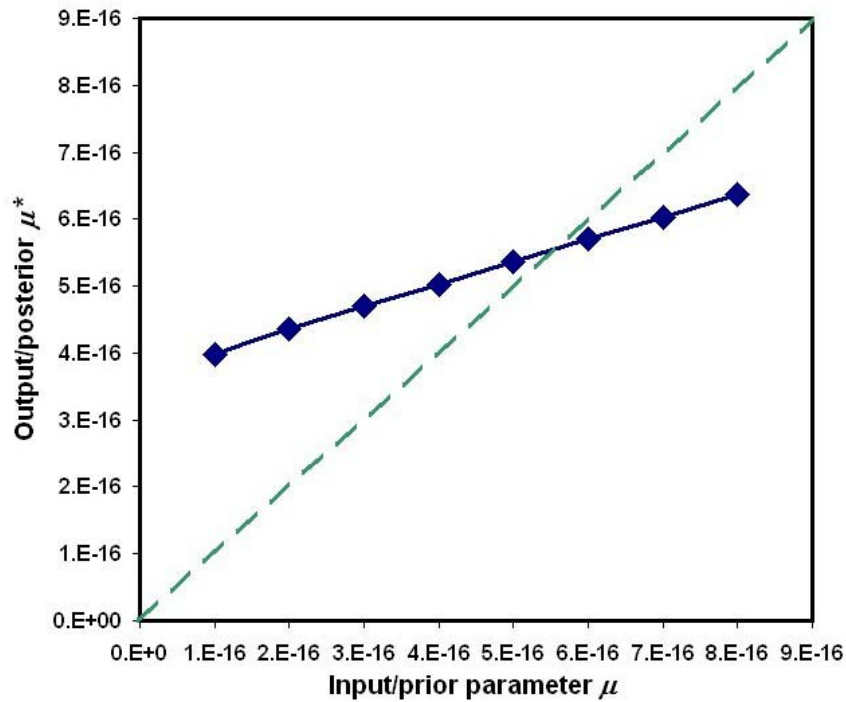
Figure 9. Posterior/output values of RMS distributed deformation rate (μ^*, in A) and 3 misfit measures (N_2^{geodetic}, N_2^{potency}, N_2^{stress}, in B) plotted as functions of input parameter μ, with fixed weights ($L_0 = 4 \times 10^4$ m, $A_0 = 4 \times 10^8$ m^2), and other inputs as in Figure 7. Note that output μ^* is relatively insensitive to input μ, and that this problem has a natural minimum μ^* of 5×10^{-16} /s.
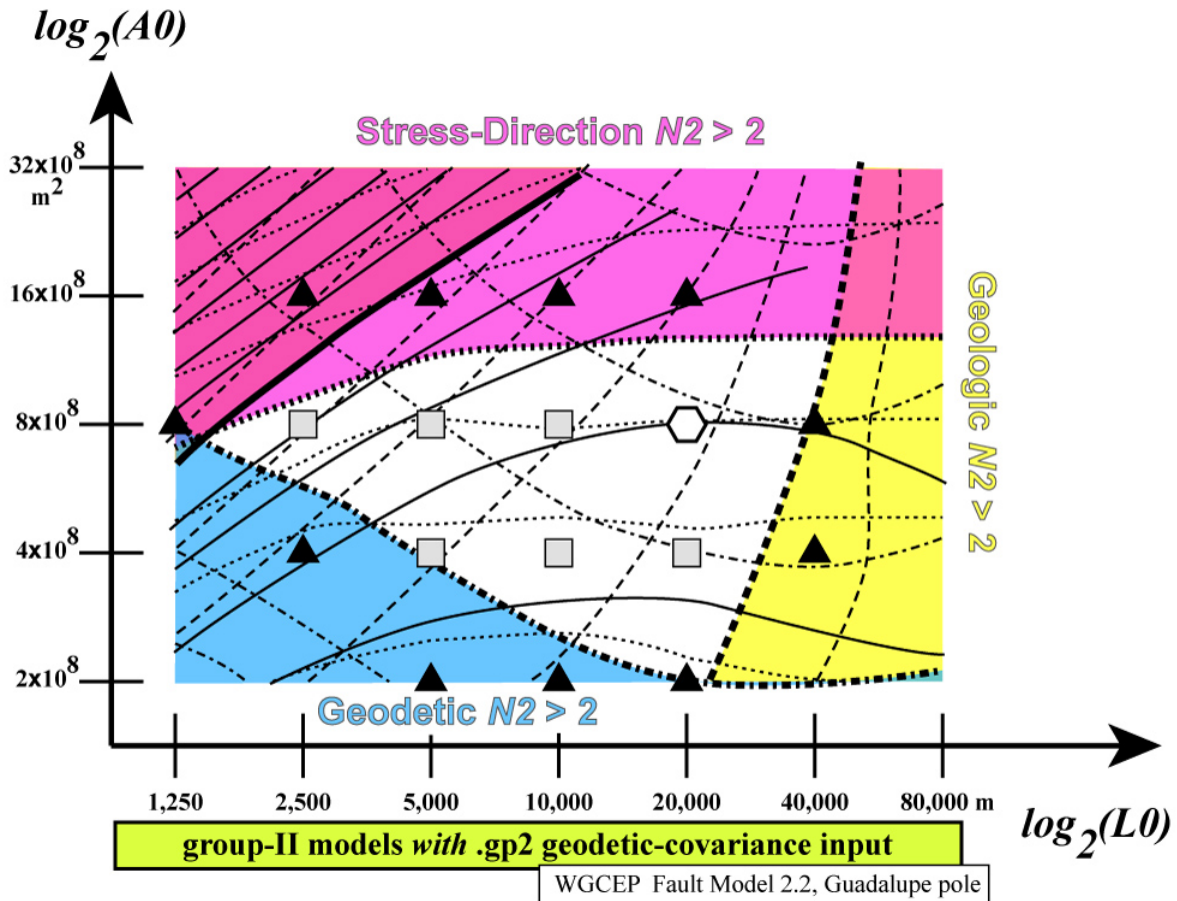
Figure 10. Three misfit measures (N_2^{geodetic} , N_2^{potency} , N_2^{stress}) are contoured in a 2-D parameter space with axes of $\log_2(L_0)$ and $\log_2(A_0)$. All conventions as in Figure 7. The differences here are that the full covariance matrix of California GPS velocities is used, the NA-PA Euler pole is the Guadalupe pole, and southern California fault traces are from WGCEP Fault Model 2.2.
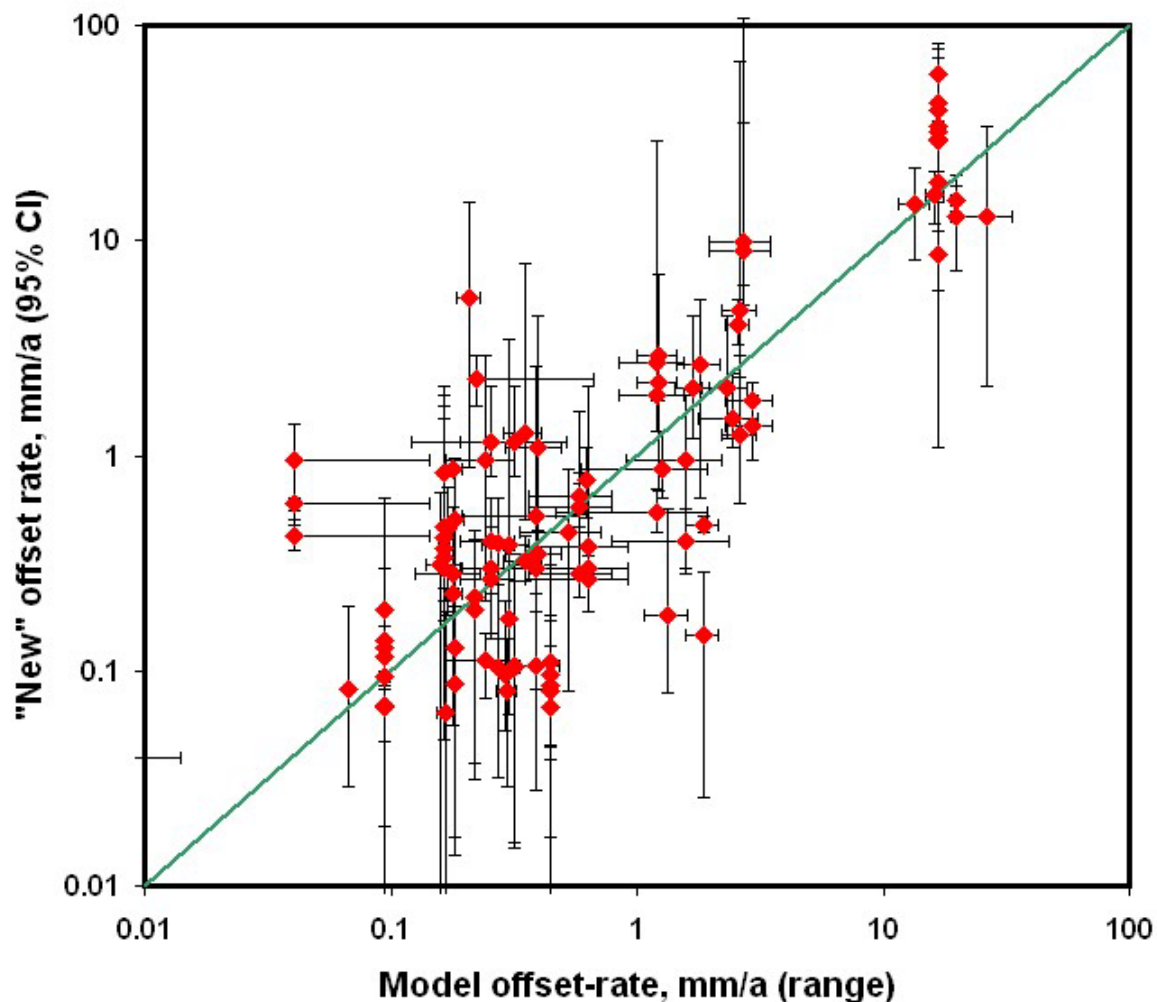
Figure 11. A pseudo-prospective test of the ability of the set of 16 successful "community" models to predict "new" long-term geologic offset rates which were not used in their computation. Data sources in Table 4. Large discrepancies are discussed individually in text Section 7.
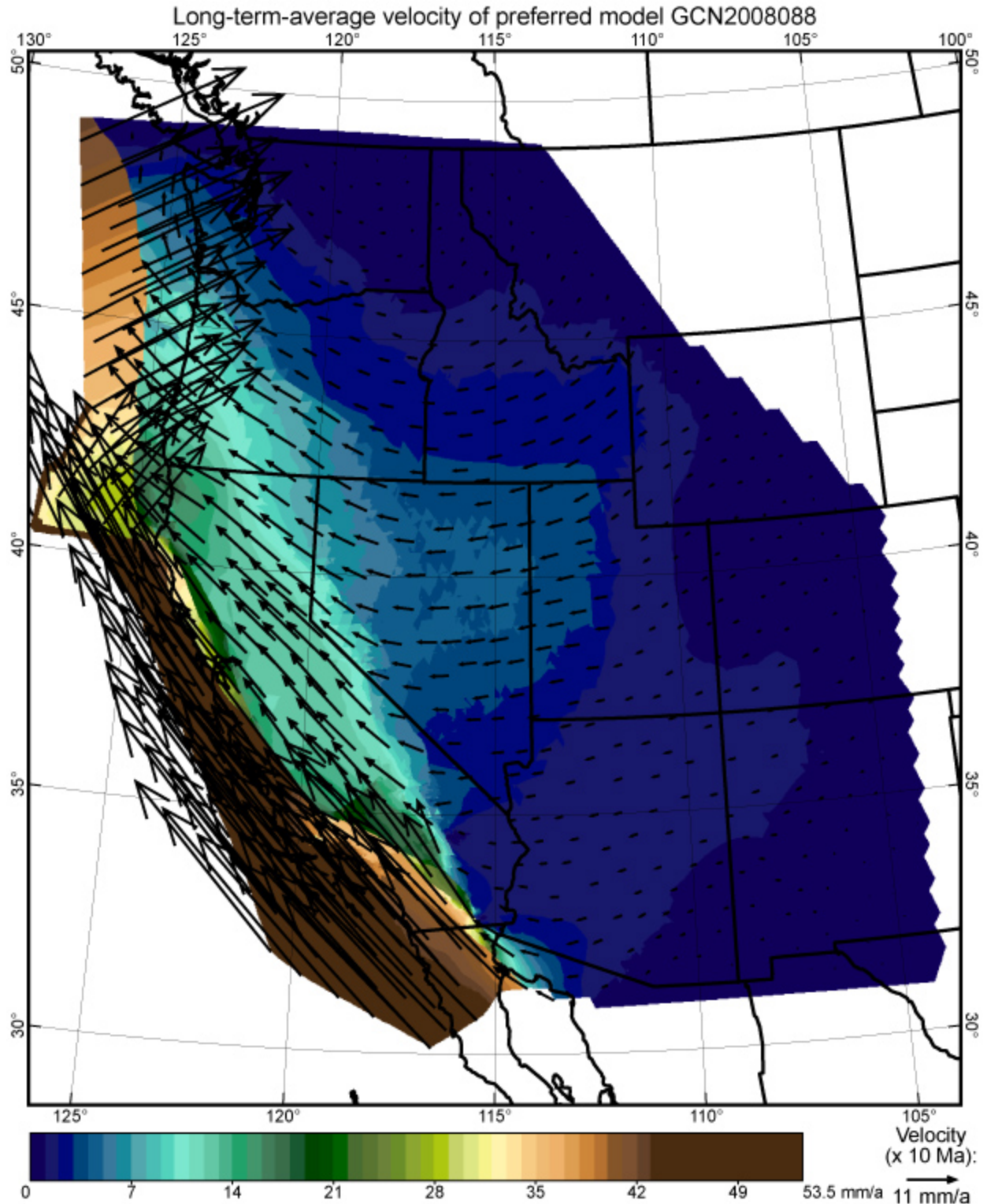
Figure 12. Long-term velocity field of the preferred model GCN2008088. Note that effects of transient elastic strain accumulation about the Cascadia trench and San Andreas fault system (and all other faults) have been removed. Color contour interval 1 mm/a up to 44 mm/a where scale saturates. For legibility, velocity vectors are shown at only 1/9 of nodes. Velocity reference frame is stable eastern North America.
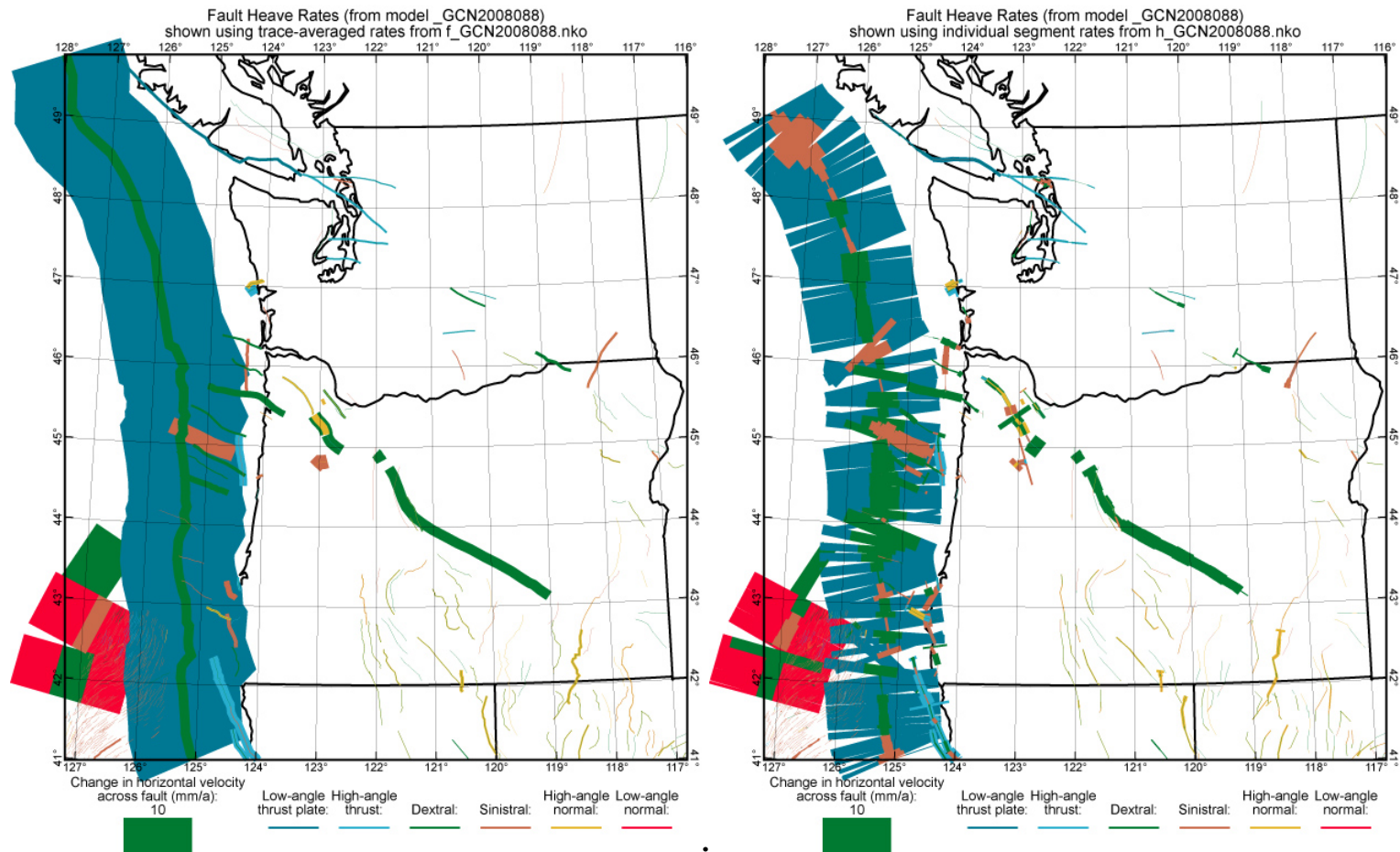
Figure 13. Fault heave rates from preferred model GCN2008088 in the Washington-Oregon region, displayed in two formats: (A) The trace-averaged heave rate is plotted at every point along the trace, giving ribbons of uniform width. (Oblique slip is represented by two ribbons of different colors plotted along the same trace.) (B) Individual per-element heave rates are plotted, without enforcing continuity along trace. This "noisy" plot has the potential advantage of displaying predicted variations in offset rate along each trace. However, it also displays probable artifacts, such as implausible high rates in elements where faults terminate without any fault junction.
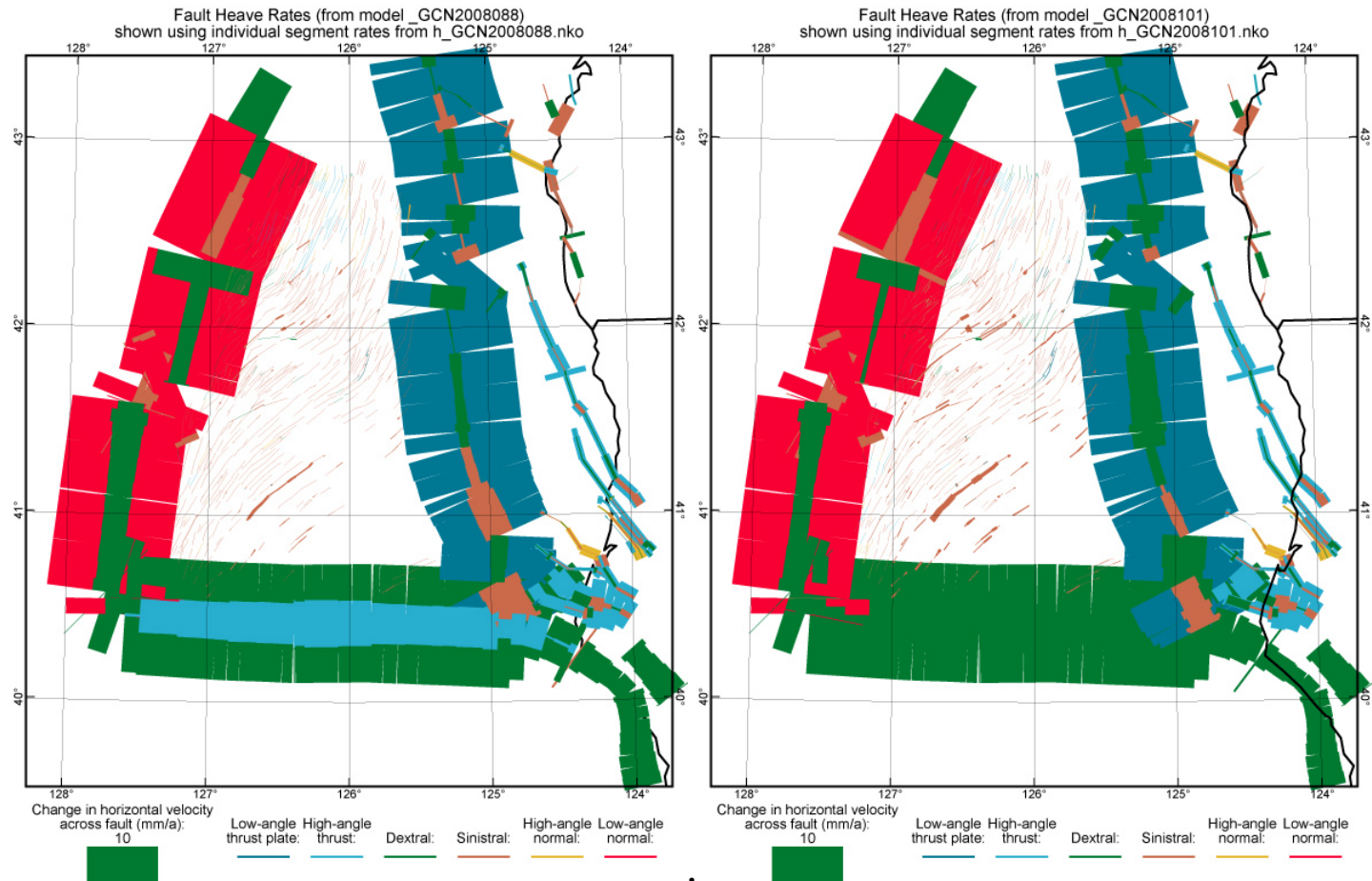
Figure 14. Fault heave rates predicted by NeoKinema in the region of the Mendocino triple junction. (A) Preferred model GCN2008088, in which the Mendocino fault is allowed to slip obliquely and absorbs 10 mm/a of N-S shortening by underthrusting Gorda crust under Pacific. (B) Ad-hoc model GCN2008101 in which the Mendocino fault is vertical, and shortening takes place by distributed deformation, faster sinistral faulting within the Gorda crust, and its accelerated subduction at the south end of the Cascadia trench.
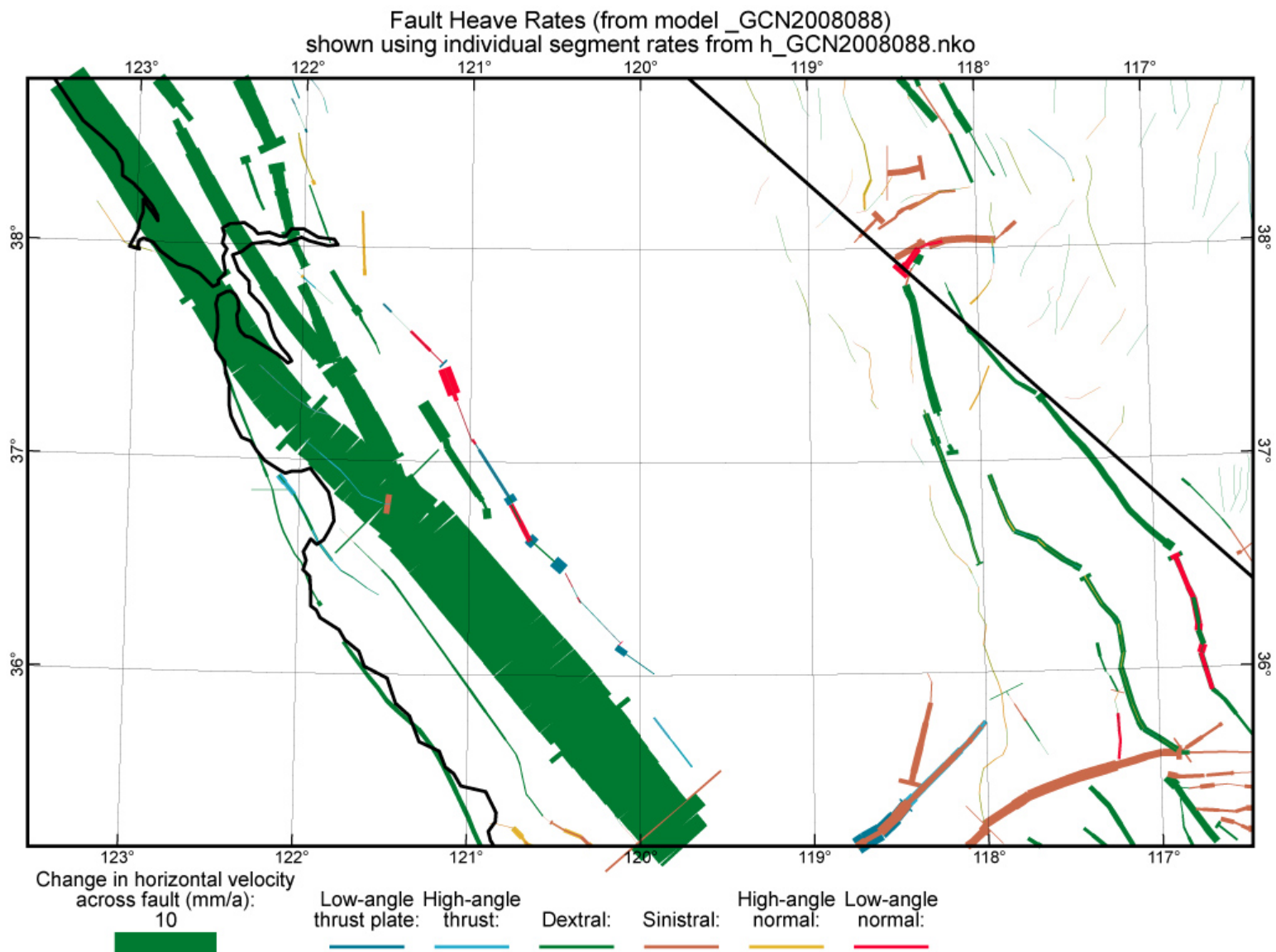
Figure 15. Fault heave rates from preferred model GCN2008088 in the San Francisco Bay, central California Coast Ranges, and central and southern Walker Lane regions.
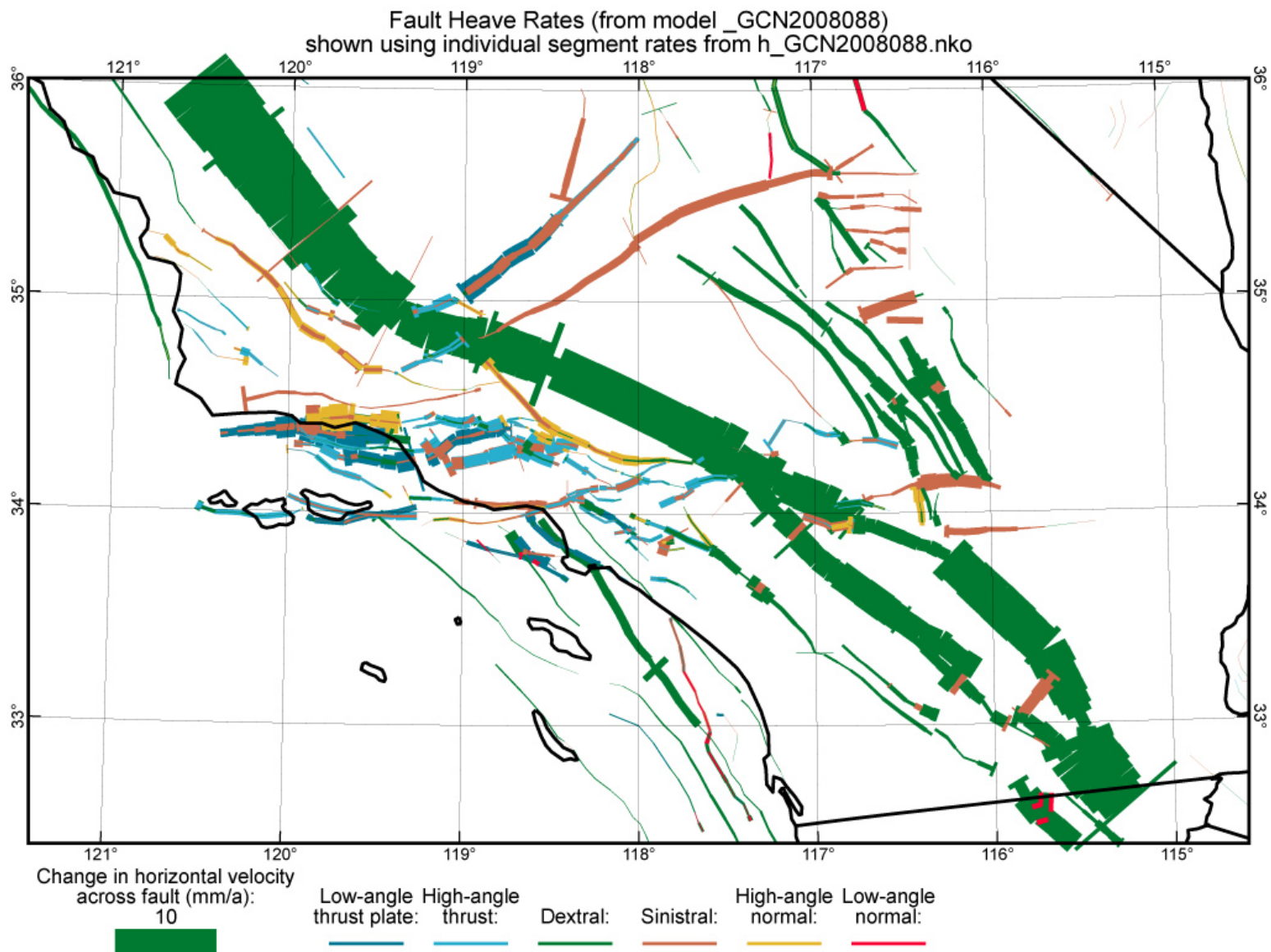
Figure 16. Fault heave rates from preferred model GCN2008088 in southern California.
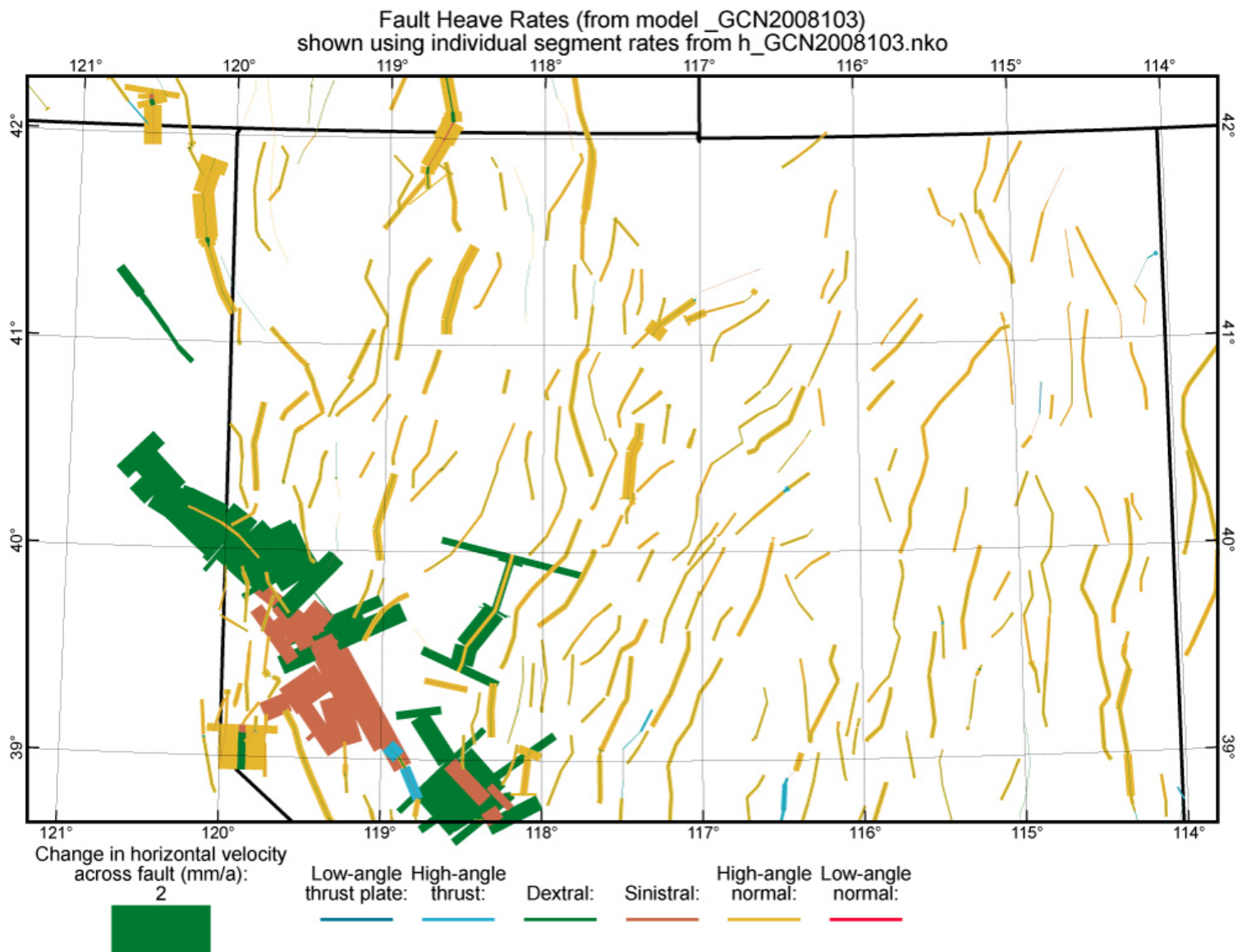
Figure 17. Fault heave rates from model GCN2008103 in the northern Walker Lane and northern Nevada.
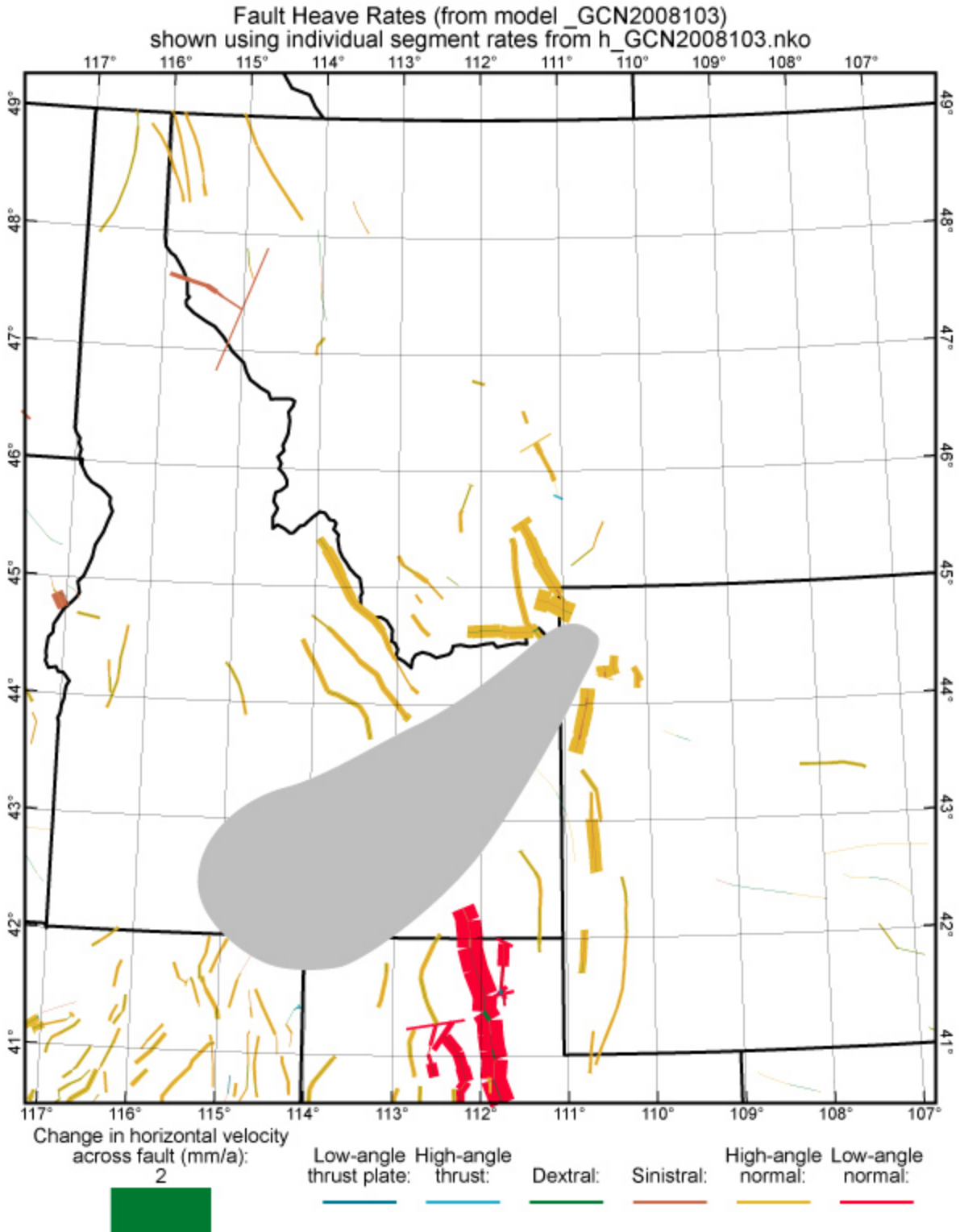
Figure 18. Fault heave rates from model GCN2008103 in the northern Rocky Mountains and northeastern Basin & Range province. While few faults are mapped within the Snake River Plain (shaded), it is moving [*Payne et al.*, 2008] and deforming by other means [*Parsons et al.*, 1998].
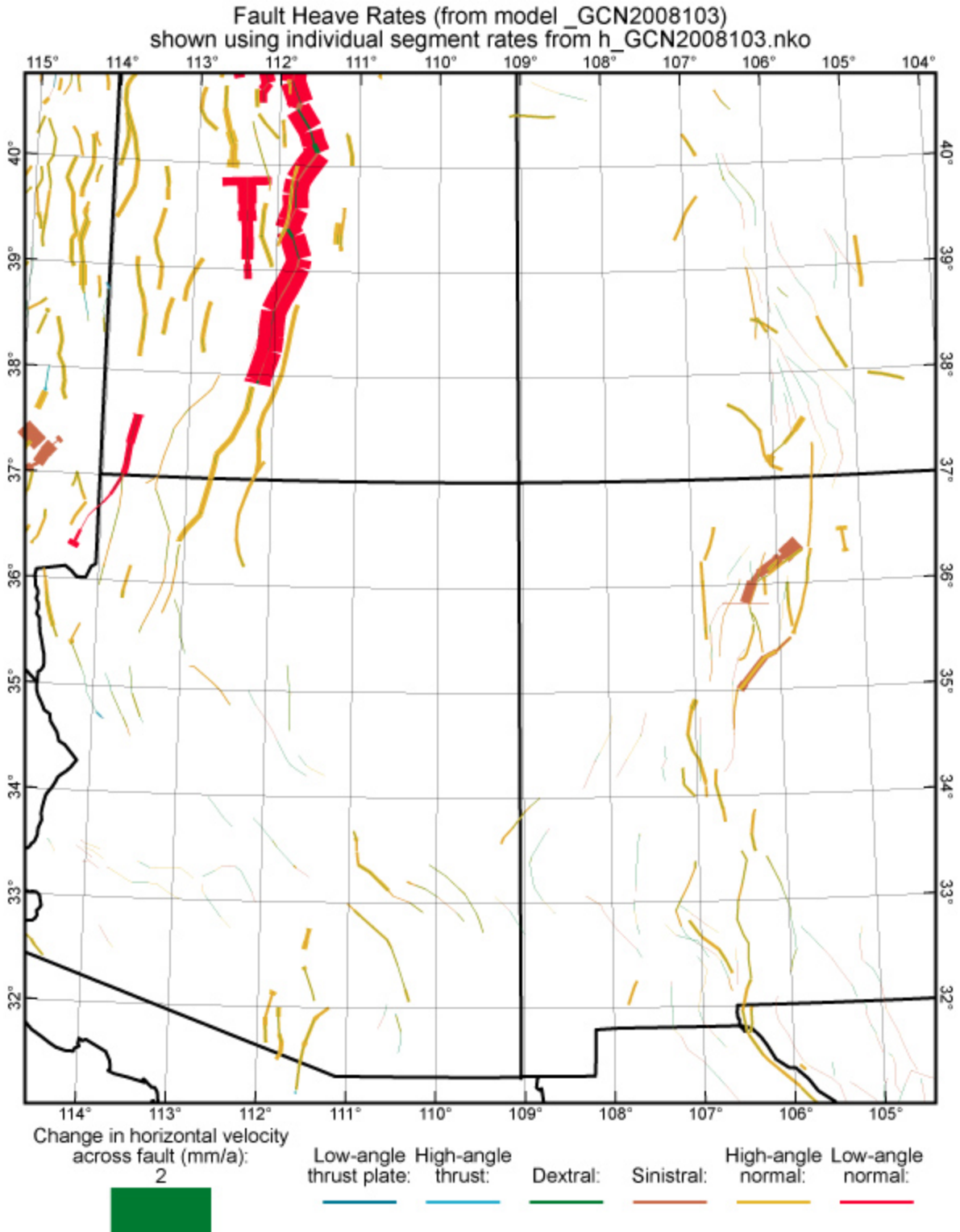
Figure 19. Fault heave rates from model GCN2008103 in the regions surrounding the Colorado Plateau.
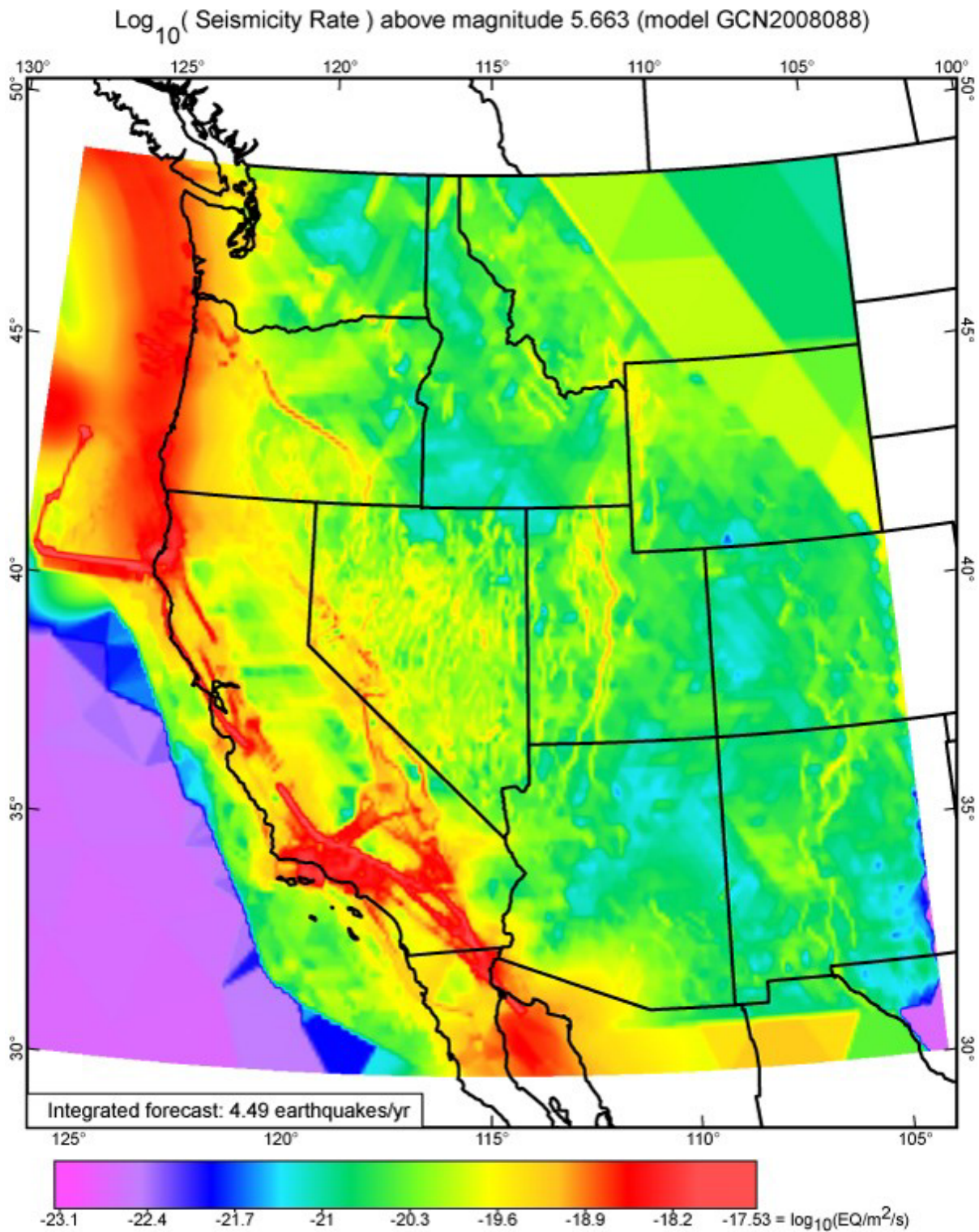
Figure 20. Common logarithm of long-term shallow seismicity (epicenters per square meter per second, including aftershocks) for threshold magnitude 5.663 (moment 3.5×10^{17} N m), computed preferred NeoKinema model GCN2008088. Seismicity around the margins (outside the NeoKinema model domain) based on relative plate motions from model PB2002 of *Bird* [2003] and intraplate strain rates from dynamic Shells model Earth5-049 of *Bird et al.* [2008]. Rates in central Montana and eastern Wyoming are probably too high, for reasons explained in that paper. The spatial integral of these forecast rates is 140 earthquakes per 31.25 years in the depth range 0~70 km. (To convert seismicity from earthquakes/m²/s to earthquakes/km²/year, add 13.5 to the values along the logarithmic scale. To convert to earthquakes/(100 km)²/century, add 19.5.)
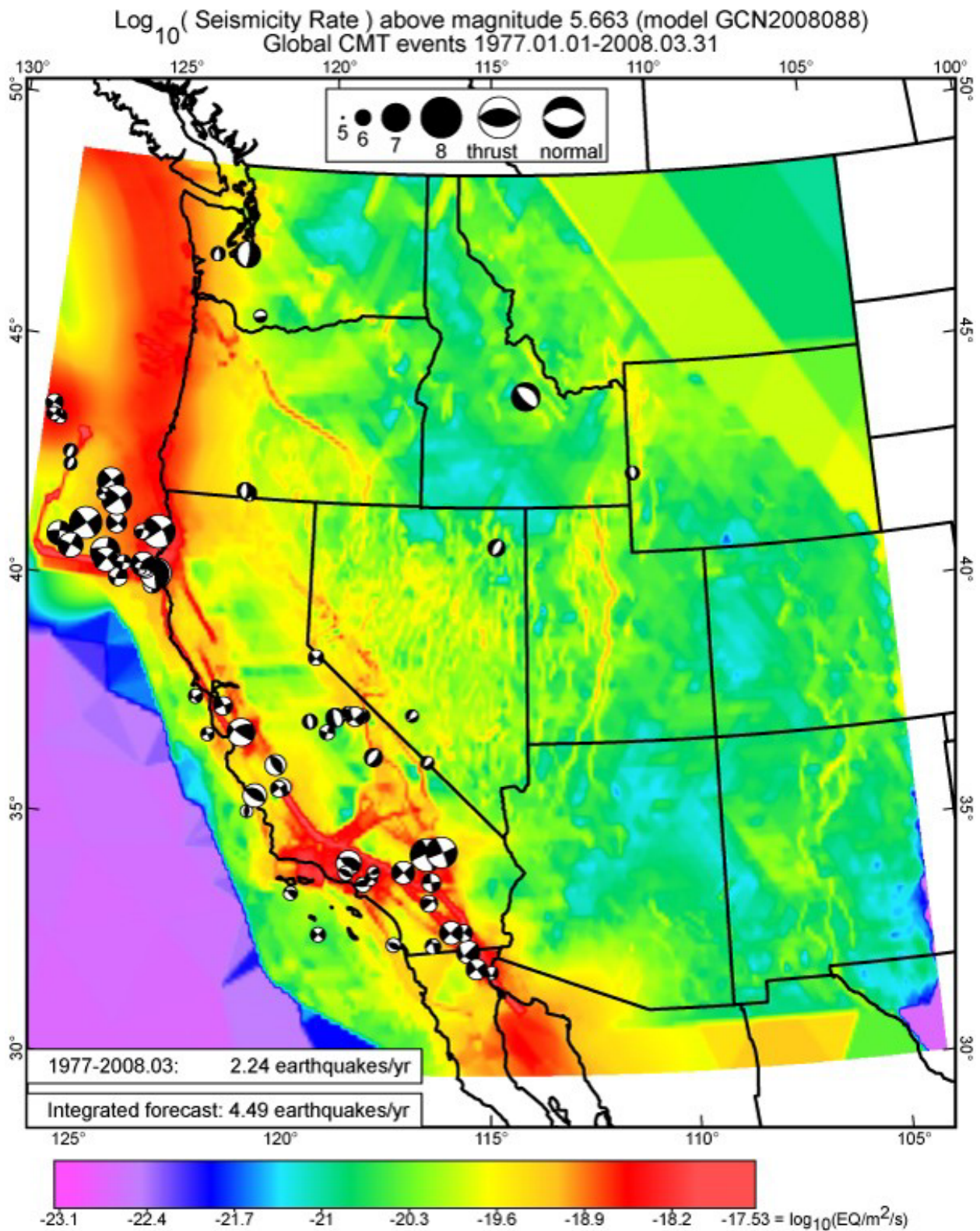
Figure 21. Colored background shows long-term forecast, exactly as in Fig. 20. For retrospective comparison, the Harvard CMT catalog shows 70 events (with focal mechanisms on lower focal hemispheres) of $m>5.663$ at 0~70 km depth in the 31.25-year interval 1977.01~2008.03. This figure illustrates why the instrumental record of seismicity is very inadequate for estimating maps of long-term seismicity.

Table 1. Comparison of modeling methods, input data counts, misfit measures, and numbers of predictions

Kinematic model of neotectonics of/within/including the western U.S.	Model type[a]	Area, 10^{12} m^2	Elements/cells/blocks	RMS resolution, km	Input geologic offset rates[b]	Input geodetic benchmarks	Input stress azimuths	$\sqrt{\dfrac{\sum \chi^2}{n}}$ of best model	Predicted fault offset rates[c]	Predicted off-fault anelastic strain-rate tensors
Saucier & Humphreys [1993]	F-E	0.36	400	30	9	10	0	?	33	0
Hearn & Humphreys [1998]	F-E	0.14	~81	42	7	5	0	?	6	0
Shen-Tu et al. [1998]	Spline	1.0	200	72	0	263	0	?	0	200
Shen-Tu et al. [1999]	Spline	0.97	154	80	<100[d]	622	0	1.3	0	154
Becker et al. [2005]	Block	0.28	10	170	0	533	5500	1.9	26	0
Bos & Spakman [2005]	F-E	1.0	1327	27	0	497	0	2.0	146	1327
McCaffrey [2005]	Soft-block	0.9	23	200	<110[d]	1523	0	1.1	220	23
Meade & Hager [2005]	Block	0.43	22	140	0	439	0	1.0[e]	94	0
d'Alessio et al. [2005]	Block	0.088	~9	~100	0	>300	0	1.9	102	0
Flesch et al. [2007]	Spline	~10	~2900	~60	?	~1970	0	?	0	~2900
Bird & Liu [2007]	F-E	2.3	10233	15	<591[d]	1034	2068	2.5	1210	10233
Pollitz et al. [2008]	VE	2.3	(none)	(fine)	<51[d]	1052	0	3.4	~28	0
This study	F-E	3.2	12627	16	572	1210	2068	1.8	2410	12627

[a]Block = purely-elastic microplates; Soft-block = microplates with 3 DOF each for internal anelastic strain-rate; F-E = finite-element grid; Spline = velocity derived from Euler pole, and Euler pole components interpolated laterally by splines on a deformed quadrilateral grid; VE = analytical viscoelastic model with faults.

[b]Counted as number of fault trains with at least one dated offset feature supporting the prior/input offset rate for that train, not as total number of offset features. Fault trains with generic/default prior/input offset rates are not counted.

[c]From 1 to 3 offset-rate components per fault train; in this study only 1 or 2 per train. In cases of Block and Soft-block models, components may include nonphysical fault-orthogonal components on vertical faults.

[d]Consensus composite fault slip rates selected by committees of experts are influenced by seismicity, paleoseismicity, geodesy, plate tectonics, and geometric compatibility as well as by dated offset geologic features (if any). Thus, many do not meet the criteria for counting in note [b].

[e]After "iterative elimination of outliers" [*Meade & Hager,* 2005, paragraph 26].

Table 2. Alternative neotectonic Euler poles for NA-PA relative rotation

Name	Reference(s)	Pole: N. lat.(deg.)	E. lon(deg.)	Rate(deg./m.y.)	@Parkfield, CA: Velocity (mm/a)	Azimuth (deg.)
NUVEL-1A	*DeMets et al.* [1990; 1994]	48.709	-78.167	0.7486	45.7	144.0
Gulf_GPS*	based on *Antonelis et al.* [1999]	51.7	-81.1	0.746	43.9	137.9
REVEL-2000*	*Sella et al.* [2002]	50.38	-72.11	0.755	50.9	141.8
ITRF2000	*Altamimi et al.* [2002]	50.488	-75.134	0.755	48.7	141.3
PA_GPS	*Beavan et al.* [2002]	50.26	-75.04	0.773	49.9	141.7
Guadalupe	*Gonzalez-Garcia et al.* [2003]	49.89	-77.01	0.766	47.8	142.1
ITRF2005	*Altamimi et al.* [2007]	49.866	-74.774	0.773	50.0	142.4
Plate_frame	*Kogan & Steblov* [2008]	51.16	-73.83	0.766	50.4	140.3

*illustrated in Figure 5, but not used in modeling.

Table 3. Computed models and their misfit measures

Model Set	Model	NA-PA Euler pole	CA Fault Model	Full GPS covariance?	$L0$, m	$A0$, m^2	μ, /s	μ^*, /s	$N_2^{geodetic}$	$N_2^{potency}$	N_2^{stress}
community	GCN2008040	NUVEL-1A	2.1	No	1.25E+03	2.0E+08	5.E-16	6.50E-16	2.614	1.423	1.237
community	GCN2008041	NUVEL-1A	2.1	No	2.50E+03	2.0E+08	5.E-16	5.72E-16	2.491	1.582	1.176
community	GCN2008042	NUVEL-1A	2.1	No	5.00E+03	2.0E+08	5.E-16	5.32E-16	2.383	1.688	1.135
community	GCN2008043	NUVEL-1A	2.1	No	1.00E+04	2.0E+08	5.E-16	5.10E-16	2.297	1.775	1.153
community	GCN2008044	NUVEL-1A	2.1	No	2.00E+04	2.0E+08	5.E-16	5.05E-16	2.238	1.863	1.220
community	GCN2008045	NUVEL-1A	2.1	No	4.00E+04	2.0E+08	5.E-16	5.09E-16	2.202	2.005	1.195
community	GCN2008046	NUVEL-1A	2.1	No	8.00E+04	2.0E+08	5.E-16	5.13E-16	2.199	2.183	1.201
community	GCN2008047	NUVEL-1A	2.1	No	1.60E+05	2.0E+08	5.E-16	5.09E-16	2.214	2.340	1.199
community	GCN2008048	NUVEL-1A	2.1	No	3.20E+05	2.0E+08	5.E-16	5.06E-16	2.260	2.600	1.201
community	GCN2008011	NUVEL-1A	2.1	No	1.25E+03	4.0E+08	5.E-16	7.90E-16	2.447	1.189	1.549
community	GCN2008010	NUVEL-1A	2.1	No	2.50E+03	4.0E+08	5.E-16	6.64E-16	2.313	1.395	1.375
community	GCN2008009	NUVEL-1A	2.1	No	5.00E+03	4.0E+08	5.E-16	5.92E-16	2.203	1.548	1.316
community	GCN2008008	NUVEL-1A	2.1	No	1.00E+04	4.0E+08	5.E-16	5.56E-16	2.358	1.658	1.275
community	GCN2008012	NUVEL-1A	2.1	No	2.00E+04	4.0E+08	5.E-16	5.39E-16	2.039	1.750	1.363
community	GCN2008013	NUVEL-1A	2.1	No	4.00E+04	4.0E+08	5.E-16	5.37E-16	1.992	1.855	1.364
community	GCN2008014	NUVEL-1A	2.1	No	8.00E+04	4.0E+08	5.E-16	5.44E-16	1.971	2.071	1.345
community	GCN2008023	NUVEL-1A	2.1	No	1.60E+05	4.0E+08	5.E-16	5.49E-16	1.983	2.369	1.330
community	GCN2008049	NUVEL-1A	2.1	No	3.20E+05	4.0E+08	5.E-16	5.45E-16	2.007	2.602	1.325
community	GCN2008015	NUVEL-1A	2.1	No	1.25E+03	8.0E+08	5.E-16	9.99E-16	2.297	0.969	1.908
community	GCN2008016	NUVEL-1A	2.1	No	2.50E+03	8.0E+08	5.E-16	8.10E-16	2.158	1.169	1.675
community	GCN2008017	NUVEL-1A	2.1	No	5.00E+03	8.0E+08	5.E-16	6.90E-16	2.042	1.371	1.520
community	GCN2008018	NUVEL-1A	2.1	No	1.00E+04	8.0E+08	5.E-16	6.24E-16	1.948	1.525	1.493
community	GCN2008019	NUVEL-1A	2.1	No	2.00E+04	8.0E+08	5.E-16	5.95E-16	1.869	1.640	1.501
community	GCN2008020	NUVEL-1A	2.1	No	4.00E+04	8.0E+08	5.E-16	5.84E-16	1.817	1.747	1.535
community	GCN2008021	NUVEL-1A	2.1	No	8.00E+04	8.0E+08	5.E-16	5.85E-16	1.788	1.944	1.503
community	GCN2008022	NUVEL-1A	2.1	No	1.60E+05	8.0E+08	5.E-16	5.98E-16	1.805	2.638	1.521
community	GCN2008050	NUVEL-1A	2.1	No	3.20E+05	8.0E+08	5.E-16	6.07E-16	1.862	3.842	1.506
community	GCN2008024	NUVEL-1A	2.1	No	1.25E+03	1.6E+09	5.E-16	1.27E-15	2.158	0.806	2.327
community	GCN2008025	NUVEL-1A	2.1	No	2.50E+03	1.6E+09	5.E-16	1.03E-15	2.013	0.958	2.048
community	GCN2008026	NUVEL-1A	2.1	No	5.00E+03	1.6E+09	5.E-16	8.45E-16	1.901	1.154	1.856
community	GCN2008027	NUVEL-1A	2.1	No	1.00E+04	1.6E+09	5.E-16	7.32E-16	1.808	1.357	1.763
community	GCN2008028	NUVEL-1A	2.1	No	2.00E+04	1.6E+09	5.E-16	6.73E-16	1.730	1.523	1.746
community	GCN2008029	NUVEL-1A	2.1	No	4.00E+04	1.6E+09	5.E-16	6.52E-16	1.669	1.652	1.749
community	GCN2008030	NUVEL-1A	2.1	No	8.00E+04	1.6E+09	5.E-16	6.47E-16	1.633	1.842	1.755

community	GCN2008031	NUVEL-1A	2.1	No	**1.60E+05**	**1.6E+09**	5.E-16	6.58E-16	1.640	2.685	1.792
community	GCN2008051	NUVEL-1A	2.1	No	**3.20E+05**	**1.6E+09**	5.E-16	6.93E-16	1.736	6.103	1.782
community	GCN2008032	NUVEL-1A	2.1	No	**1.25E+03**	**3.2E+09**	5.E-16	1.58E-15	2.037	0.687	2.779
community	GCN2008033	NUVEL-1A	2.1	No	**2.50E+03**	**3.2E+09**	5.E-16	1.31E-15	1.888	0.801	2.470
community	GCN2008034	NUVEL-1A	2.1	No	**5.00E+03**	**3.2E+09**	5.E-16	1.07E-15	1.772	0.949	2.258
community	GCN2008035	NUVEL-1A	2.1	No	**1.00E+04**	**3.2E+09**	5.E-16	8.98E-16	1.682	1.144	2.119
community	GCN2008036	NUVEL-1A	2.1	No	**2.00E+04**	**3.2E+09**	5.E-16	7.94E-16	1.607	1.357	2.076
community	GCN2008037	NUVEL-1A	2.1	No	**4.00E+04**	**3.2E+09**	5.E-16	7.43E-16	1.545	1.526	2.084
community	GCN2008038	NUVEL-1A	2.1	No	**8.00E+04**	**3.2E+09**	5.E-16	7.33E-16	1.497	1.723	2.087
community	GCN2008039	NUVEL-1A	2.1	No	**1.60E+05**	**3.2E+09**	5.E-16	7.40E-16	1.487	2.405	2.128
community	GCN2008052	NUVEL-1A	2.1	No	**3.20E+05**	**3.2E+09**	5.E-16	7.88E-16	1.582	6.715	2.159
community	GCN2008099	NUVEL-1A	2.1	No	4.00E+04	4.0E+08	**8.E-16**	6.36E-16	1.756	1.555	1.156
community	GCN2008098	NUVEL-1A	2.1	No	4.00E+04	4.0E+08	**7.E-16**	6.03E-16	1.820	1.641	1.195
community	GCN2008097	NUVEL-1A	2.1	No	4.00E+04	4.0E+08	**6.E-16**	5.70E-16	1.897	1.741	1.294
community	GCN2008013	NUVEL-1A	2.1	No	4.00E+04	4.0E+08	**5.E-16**	5.37E-16	1.992	1.855	1.364
community	GCN2008092	NUVEL-1A	2.1	No	4.00E+04	4.0E+08	**4.E-16**	5.03E-16	2.125	2.001	1.430
community	GCN2008093	NUVEL-1A	2.1	No	4.00E+04	4.0E+08	**3.E-16**	4.71E-16	2.317	2.161	1.506
community	GCN2008095	NUVEL-1A	2.1	No	4.00E+04	4.0E+08	**2.E-16**	4.36E-16	2.642	2.392	1.690
community	GCN2008096	NUVEL-1A	2.1	No	4.00E+04	4.0E+08	**1.E-16**	3.97E-16	3.355	3.089	2.153
community	GCN2008053	**ITRF2000**	2.1	No	2.00E+04	1.6E+09	5.E-16	6.70E-16	1.691	1.581	1.718
community	GCN2008054	**PA_GPS**	2.1	No	2.00E+04	1.6E+09	5.E-16	6.78E-16	1.693	1.584	1.727
community	GCN2008055	**Gaudalupe**	2.1	No	2.00E+04	1.6E+09	5.E-16	6.70E-16	1.698	1.547	1.714
community	GCN2008057	**ITRF2005**	2.1	No	2.00E+04	1.6E+09	5.E-16	6.81E-16	1.695	1.572	1.720
community	GCN2008094	**Plate_frame**	2.1	No	2.00E+04	1.6E+09	5.E-16	6.80E-16	1.692	1.645	1.756
community	GCN2008056	Gaudalupe	**2.2**	No	2.00E+04	1.6E+09	5.E-16	6.70E-16	1.706	1.560	1.707
community	GCN2008068	Gaudalupe	2.2	**Yes**	**1.25E+03**	**8.0E+08**	5.E-16	1.09E-15	2.000	0.990	2.069
community	GCN2008073	Gaudalupe	2.2	Yes	**2.50E+03**	**1.6E+09**	5.E-16	1.15E-15	1.753	0.977	2.331
community	GCN2008067	Gaudalupe	2.2	Yes	**2.50E+03**	**8.0E+08**	5.E-16	9.04E-16	1.905	1.198	1.900
community	GCN2008072	Gaudalupe	2.2	Yes	**2.50E+03**	**4.0E+08**	5.E-16	7.28E-16	2.097	1.426	1.548
community	GSN2008070	Gaudalupe	2.2	Yes	**5.00E+03**	**1.6E+09**	5.E-16	9.75E-16	1.657	1.186	2.195
community	GCN2008065	Gaudalupe	2.2	Yes	**5.00E+03**	**8.0E+08**	5.E-16	7.87E-16	1.812	1.413	1.795
community	GCN2008069	Gaudalupe	2.2	Yes	**5.00E+03**	**4.0E+08**	5.E-16	6.56E-16	1.970	1.585	1.548
community	GCN2008071	Gaudalupe	2.2	Yes	**5.00E+03**	**2.0E+08**	5.E-16	5.71E-16	2.161	1.717	1.332
community	GCN2008075	Gaudalupe	2.2	Yes	**1.00E+04**	**1.6E+09**	5.E-16	8.68E-16	1.571	1.407	2.128
community	GCN2008063	Gaudalupe	2.2	Yes	**1.00E+04**	**8.0E+08**	5.E-16	7.22E-16	1.713	1.584	1.804
community	GCN2008064	Gaudalupe	2.2	Yes	**1.00E+04**	**4.0E+08**	5.E-16	6.23E-16	1.879	1.719	1.527
community	GCM2008076	Gaudalupe	2.2	Yes	**1.00E+04**	**2.0E+08**	5.E-16	5.61E-16	2.068	1.822	1.331
community	GCN2008059	Gaudalupe	2.2	Yes	**2.00E+04**	**1.6E+09**	5.E-16	8.14E-16	1.496	1.600	2.094
community	GCN2008060	Gaudalupe	2.2	Yes	**2.00E+04**	**8.0E+08**	5.E-16	6.99E-17	1.645	1.761	1.798

community	GCN2008061	Gaudalupe	2.2	Yes	**2.00E+04**	**4.0E+08**	5.E-16	6.19E-16	1.819	1.866	1.551
community	GCN2008062	Gaudalupe	2.2	Yes	**2.00E+04**	**2.0E+08**	5.E-16	5.67E-16	2.006	1.972	1.368
community	GCN2008066	Gaudalupe	2.2	Yes	**4.00E+04**	**8.0E+08**	5.E-16	7.03E-16	1.599	2.014	1.798
community	GCN2008074	Gaudalupe	2.2	Yes	**4.00E+04**	**4.0E+08**	5.E-16	6.32E-16	1.774	2.105	1.530
community	GCN2008079	**Plate_frame**	**2.1**	Yes	2.00E+04	8.0E+08	5.E-16	7.06E-16	2.215	1.833	1.811
community	GCN2008077	**Guadalupe**	**2.1**	Yes	2.00E+04	8.0E+08	5.E-16	7.03E-16	1.679	1.765	1.844
community	GCN2008078	**NUVEL-1A**	**2.1**	Yes	2.00E+04	8.0E+08	5.E-16	7.05E-16	1.814	1.736	1.939
community	GCN2008080	**Plate_frame**	**2.2**	Yes	2.00E+04	8.0E+08	5.E-16	7.03E-16	2.168	1.827	1.773
community	GCN2008060	**Guadalupe**	**2.2**	Yes	2.00E+04	8.0E+08	5.E-16	6.99E-17	1.645	1.761	1.798
community	GCN2008081	**NUVEL-1A**	**2.2**	Yes	2.00E+04	8.0E+08	5.E-16	7.01E-16	1.810	1.733	1.893
updated	GCN2008088	**Guadalupe**	**2.2**	Yes	2.00E+04	8.0E+08	5.E-16	7.01E-16	1.638	1.711	1.786
updated	GCN2008089	**NUVEL-1A**	**2.2**	Yes	2.00E+04	8.0E+08	5.E-16	7.02E-16	1.805	1.686	1.862
updated	GCN2008090	**NUVEL-1A**	**2.1**	Yes	2.00E+04	8.0E+08	5.E-16	7.05E-16	1.806	1.683	1.883
updated	GCN2008091	**Guadalupe**	**2.1**	Yes	2.00E+04	8.0E+08	5.E-16	7.03E-16	1.669	1.709	1.841
ad-hoc	GCN2008100	Guadalupe	2.2	Yes	2.00E+04	8.0E+08	5.E-16	7.01E-16	1.622	1.713	1.764
ad-hoc	GCN2008101	Guadalupe	2.2	Yes	2.00E+04	8.0E+08	5.E-16	7.40E-16	1.657	1.596	1.818
ad-hoc	GCN2008102	Guadalupe	2.2	Yes	2.00E+04	8.0E+08	5.E-16	7.02E-16	1.639	1.713	1.776
ad-hoc	GCN2008103	Guadalupe	2.2	Yes	2.00E+04	8.0E+08	5.E-16	7.03E-16	1.641	1.713	1.774

Table 4. Fault offset rates predicted by acceptable community models compared to new geologic offset rates

North Lat., dec. ° Fault, State	Neo-Kinema Train	Offset Type	Community Model Predictions:	New Citation	New geologic offset rate (Slippery, 95% CI) min.	max.	Discrepancy	Updated Models: Prediction:	Discrep.
48.12 Southern Whidbey Island thrust, WA	F2337	T	0.334~0.717	*Kelsey et al.* [2004]	0.080	0.87	0	0.224~0.228	0
47.56 Seattle thrust fault, WA	F1951	T	0.166~0.315	*Johnson et al.* [1999]	0.21	2.9	0	0.215~0.222	0
47.56 Seattle thrust fault, WA	F1951	T	0.166~0.315	*Johnson et al.* [2004]	0.074	0.148	0.018	0.215~0.222	0.067
47.36 Tacoma thrust fault, WA	F3400	T	0	*Johnson et al.* [2004]	0.19	0.23	0.19	0.197	0
47.36 Tacoma thrust fault, WA	F3400	T	0	*Sherrod et al.* [2004]	0.12	4.6	0.12	0.197	0
47.36 Tacoma thrust fault, WA	F3400	T	0	*Sherrod et al.* [2004]	0.026	0.25	0.026	0.197	0
43.00 Red Cone Spring normal fault, OR	F1959	N	0.165	*Bacon et al.* [1999]	0.24	2.1	0.075	0.327	0
42.86 Annie Spring normal fault, OR	F1959	N	0.165	*Bacon et al.* [1999]	0.21	0.39	0.045	0.327	0
42.86 Annie Spring normal fault, OR	F1959	N	0.165	*Bacon et al.* [1999]	0.24	1.7	0.075	0.327	0
42.86 Annie Spring normal fault, OR	F1959	N	0.165	*Bacon et al.* [1999]	0.31	1.9	0.145	0.327	0
42.86 Annie Spring normal fault, OR	F1959	N	0.165	*Bacon et al.* [1999]	0.17	1.5	0.005	0.327	0
42.86 Annie Spring normal fault, OR	F1959	N	0.165	*Bacon et al.* [1999]	0.048	1.7	0	0.327	0
41.44 Quinn R. sec., Santa Rosa Range n.f.,NV-OR	F0676	N	0.3~0.304	*Personius et al.* [2002]	0.063	3.5	0	0.132~0.324	0
41.21 Trinidad thrust fault, off CA-CA	F4019	T	0.364~0.793	*McCrory* [2000] (site 26)	0.53	0.84	0	0.616~0.619	0
41.18 Big Lagoon-Bald Mountain thrust, off OR-CA	F4018	T	0.47~1.93	*McCrory* [2000] (site 25)	0.44	0.70	0	0.87~0.877	0.17
41.02 Trinidad thrust fault, off CA-CA	F4019	T	0.364~0.793	*McCrory* [2000] (site 22)	0.47	0.74	0	0.616~0.619	0
41.02 Trinidad thrust fault, off CA-CA	F4019	T	0.364~0.793	*McCrory* [2000] (site 21)	0.22	1.6	0	0.616~0.619	0
40.98 McKinleyville thrust fault, CA	F4021	T	0.354~0.913	*McCrory* [2000] (site 20)	0.28	2.1	0	0.321~0.329	0
40.97 McKinleyville thrust fault, CA	F4021	T	0.354~0.913	*McCrory* [2000] (site 19)	0.19	0.44	0	0.321~0.329	0
40.95 Mad River thrust fault, CA	F4022	T	0.288~0.411	*McCrory* [2000] (site 18)	0.50	7.8	0.089	-0.675~-0.593	1.093
40.94 Blue Lake thrust fault, CA	F3410	T	0	*McCrory* [2000] (site 17)	0.76	1.2	0.76	0.898~0.9	0
40.88 Mad River thrust fault, CA	F4022	T	0.288~0.411	*McCrory* [2000] (site 15)	0.26	0.42	0	-0.675~-0.593	0.853
40.88 Fickle Hill thrust, off CA-CA	F4020	T	0.291~0.496	*McCrory* [2000] (site 16)	0.36	4.5	0	0.111~0.13	0.23
40.87 McKinleyville thrust fault, CA	F4021	T	0.354~0.913	*McCrory* [2000] (site 14)	0.19	0.34	0.014	0.321~0.329	0
40.81 Fickle Hill thrust, off CA-CA	F4020	T	0.291~0.496	*McCrory* [2000] (site 13)	0.28	0.45	0	0.111~0.13	0.15
40.69 Table Bluff thrust fault, off CA-CA	F4015	T	0.794~2.35	*McCrory* [2000] (site 8)	0.28	0.57	0.224	0.471~0.474	0
40.66 Little Salmon (Onshore) thrust, CA	F4017	T	1~1.45	*McCrory* [2000] (site 7)	0.69	6.9	0	1.14~1.15	0
40.63 Little Salmon (Onshore) thrust, CA	F4017	T	1~1.45	*McCrory* [2000] (site 5)	1.8	2.9	0.35	1.14~1.15	0.65
40.52 Russ thrust fault, off CA-CA	F3409	T	0	*McCrory* [2000] (site 1)	0.28	1.1	0.28	3.3~3.51	2.2
40.52 Russ thrust fault, off CA-CA	F3409	T	0	*McCrory* [2000] (site 1)	0.12	3.1	0.12	3.3~3.51	0.2
40.95 East Humboldt Range normal fault, NV	F0512	N	0.294	*Wesnousky & Willoughby* [2003]	0.053	0.21	0.084	0.24	0.03
40.82 Independence Valley normal fault, NV	F2138	N	0.18~0.182	*Wesnousky et al.* [2005]	0.014	0.20	0	0.087	0
40.76 Grass Valley normal fault, NV	F2132	N	0.181~0.186	*Wesnousky et al.* [2005]	0.017	0.31	0	0.13	0
40.75 Wasatch normal fault, UT	F0505	D	0.616~0.626	*Armstrong et al.* [2004]	0.51	1.1	0	1.01	0
40.64 Buena Vista (Beachfront) normal fault, NV	F2102	N	0.305~0.335	*Hanks & Wallace* [1985]	0.015	0.31	0	0.176~0.177	0

40.49 Western Shoshone Range normal fault, NV	F2170	N	0.296~0.488	*Wesnousky et al.* [2005]	0.028	0.23	0.066	0.144~0.146	0
40.47 Western Humboldt Range normal fault, NV	F0665	N	0.305~0.333	*Wesnousky et al.* [2005]	0.016	0.26	0.045	0.15~0.151	0
40.44 Dry Hills(?) normal fault, NV	F1659	N	0.155~0.181	*Wesnousky et al.* [2005]	0.0061	0.19	0	0.062	0
40.38 Stansbury normal fault, UT	F0514	N	0.001~0.014	*Swan et al.* [2004]	0.002	0.71	0	0.427~0.429	0
40.25 Crescent normal fault, NV	F0511	N	-0.582~-0.02	*Friedrich et al.* [2004]	0.21	1.1	0.23	0.203~0.208	0.002
40.20 Granite Springs Valley normal fault, NV	F0664	N	0.001~0.009	*Wesnousky et al.* [2005]	0.13	1.0	0.121	0.462~0.467	0
40.15 Beowawe-Malpais normal fault, NV	F1660	N	0.138~0.181	*Wesnousky et al.* [2005]	0.0035	0.67	0	0.299~0.3	0
40.05 Honey Lake dextral fault, CA	F4014	R	1.42~1.97	*Faulds et al.* [2005]	1.2	4.5	0	1.21~1.25	0
39.92 Warm Springs Valley dextral fault, CA-NV	F1953	R	0~0.001	*Faulds et al.* [2005]	1.2	4.5	1.199	0.901~1.42	0
39.90 Honey Lake dextral fault, NV	F2225	R	1.85~2.79	*Faulds et al.* [2005]	1.2	4.5	0	1.22~1.26	0
39.90 Pyramid Lake dextral fault, NV	F1952	R	2.22~3.05	*Faulds et al.* [2005]	0.60	2.9	0	2.26~2.35	0
39.83 Bradys normal fault, NV	F3401	N	0	*Wesnousky et al.* [2005]	0.015	0.38	0.015	0.148~0.149	0
39.69 Pyramid Lake fault, NV	F1952	R	2.22~3.05	*Briggs & Wesnousky* [2004]	2.3	68	0	2.26~2.35	0
39.68 Dixie Valley normal fault, NV	F0524	N	0.275	*Bell & Katzer* [1990]	0.032	0.25	0.025	0.275	0.025
39.68 Dixie Valley normal fault, NV	F0524	N	0.275	*Bell & Katzer* [1990]	0.14	0.63	0	0.275	0
39.41 Rainbow Mountain normal fault, NV	F0667	N	0.214~0.222	*Bell et al.* [2004]	0.037	0.45	0	0.207	0
39.41 Rainbow Mountain normal fault, NV	F0667	N	0.214~0.222	*Caskey et al.* [2004]	0.031	0.41	0	0.207	0
39.33 Fourmile Flat normal fault, NV	F3402	N	0	*Bell et al.* [2004]	0.066	0.69	0.066	0.371	0
39.33 Fourmile Flat normal fault, NV	F3402	N	0	*Caskey et al.* [2004]	0.059	0.70	0.059	0.371	0
40.31 West Mercur normal fault, UT	F0602	N	0.269~0.322	*Mattson & Bruhn* [2001]	0.029	0.14	0.129	0.091	0
39.27 Fairview Peak normal fault, NV	F2128	N	0.065~0.069	*Bell et al.* [2004]	0.029	0.20	0	0.068	0
39.26 Sand Springs normal fault, NV	F2167	N	0.158~0.181	*Bell et al.* [2004]	0.18	0.72	0	0.45~0.452	0
39.15 Carson Range normal fault, NV	F2107	N	0.184~0.232	*Ramelli et al.* [1999]	0.88	15	0.648	2.92~2.93	0
38.40 Monte Cristo Valley dextral fault, NV	F2149	R	-0.89~-0.718	*Bell et al.* [1999]	0.053	0.54	0.771	0.187~0.202	0
37.38 Deep Springs normal fault, CA	F4051	N	0.166~0.194	*Lee et al.* [2001a]	0.22	0.24	0.026	0.805~0.808	0.565
37.38 Deep Springs normal fault, CA	F4051	N	0.166~0.194	*Lee et al.* [2001a]	0.84	0.88	0.646	0.805~0.808	0.032
37.20 Owens Valley dextral/normal fault, CA	F4064	N	0	*Clark* [1979]	0.14	1.8	0.14	0.242	0
37.07 Owens Valley dextral/normal fault, CA	F4064	N	0	*Martel et al.* [1987]	0.21	0.29	0.21	0.242	0
36.88 Death Valley dextral fault, NV-CA	F4046	R	2.29~2.84	*Frankel et al.* [2007]	3.3	5.3	0.46	2.55~2.59	0.71
36.65 Independence normal fault, CA	F4065	N	0.191~0.318	*Le et al.* [2007] (Qf1)	0.15	0.39	0	0.313	0
36.65 Independence normal fault, CA	F4065	N	0.191~0.318	*Le et al.* [2007] (Qf2b)	0.14	0.47	0	0.313	0
36.65 Independence normal fault, CA	F4065	N	0.191~0.318	*Le et al.* [2007] (Qf3a)	0.23	0.63	0	0.313	0
36.63 Owens Valley dextral/normal fault, CA	F4064	R	1.44~2.18	*Lee et al.* [2001b]	0.63	5.3	0	1.91~1.92	0
36.62 Owens Valley dextral/normal fault, CA	F4064	N	0	*Bacon & Pezzopane* [2007]	0.017	0.32	0.017	0.242	0
36.20 Toroweap normal fault, AZ	F1262	N	0.093~0.096	*Fenton et al.* [2001]	0.099	0.14	0.003	0.101	0
36.20 Toroweap normal fault, AZ	F1262	N	0.093~0.096	*Fenton et al.* [2001]	0.10	0.16	0.004	0.101	0
36.20 Toroweap normal fault, AZ	F1262	N	0.093~0.096	*Fenton et al.* [2001]	0.047	0.089	0.004	0.101	0.012
36.20 Toroweap normal fault, AZ	F1262	N	0.093~0.096	*Fenton et al.* [2001]	0.019	0.13	0	0.101	0
36.20 Toroweap normal fault, AZ	F1262	N	0.093~0.096	*Fenton et al.* [2001]	0.082	0.30	0	0.101	0
36.20 Toroweap normal fault, AZ	F1262	N	0.093~0.096	*Fenton et al.* [2001]	0.0085	0.64	0	0.101	0

36.20 Toroweap normal fault, AZ	F1262	N	0.093~0.096	*Pederson et al.* [2002]	0.085	0.10	0	0.101	0.001
36.20 Hurricane normal fault, AZ	F0492	N	0.444~0.453	*Fenton et al.* [2001]	0.044	0.092	0.352	0.074	0
36.20 Hurricane normal fault, AZ	F0492	N	0.444~0.453	*Fenton et al.* [2001]	0.045	0.13	0.314	0.074	0
36.20 Hurricane normal fault, AZ	F0492	N	0.444~0.453	*Fenton et al.* [2001]	0.017	0.17	0.274	0.074	0
36.20 Hurricane normal fault, AZ	F0492	N	0.444~0.453	*Fenton et al.* [2001]	0.017	0.31	0.134	0.074	0
36.20 Hurricane normal fault, AZ	F0492	N	0.444~0.453	*Fenton et al.* [2001]	0.039	0.18	0.264	0.074	0
36.20 Hurricane normal fault, AZ	F0492	N	0.444~0.453	*Fenton et al.* [2001]	0.0041	0.38	0.064	0.074	0
36.15 So Sierra Nevada normal fault, CA	F4063	N	0.165~0.197	*St.-Amand & Roquemore* [1979]	0.28	0.97	0.083	0.48~0.482	0
35.77 Stateline dextral fault, NV-CA	F1850	R	-0.228~0.671	*Guest et al.* [2007]	1.7	2.9	1.029	-0.178~0.059	1.641
35.70 Searles Valley detachment, CA	F4145	D	0.126~0.23	*Numelin et al.* [2007]	0.056	0.58	0	1.05~1.12	0.47
35.55 Garlock (Central) sinistral fault, CA	F4341	L	1.95~3.5	*McGill & Sieh* [1993]	6.2	35	2.7	3.66~3.83	2.37
35.55 Garlock (Central) sinistral fault, CA	F4341	L	1.95~3.5	*McGill & Sieh* [1993]	5.0	108	1.5	3.66~3.83	1.17
35.36 Blackwater dextral fault, CA	F4087	R	1.59~2.14	*Oskin & Iriondo* [2004]	0.026	0.29	1.3	1.67~1.78	1.38
35.19 Blackwater dextral fault, CA	F4087	R	1.59~2.14	*Oskin & Iriondo* [2004]	0.44	0.52	1.07	1.67~1.78	1.15
34.64 Lenwood dextral fault, CA	F4085	R	1.77~3.08	*Oskin et al.* [2006]	1.1	2.4	0	2.42~2.55	0.02
34.73 Calico-Hidalgo dextral fault, CA	F4088	R	2.29~3.57	*Oskin et al.* [2007] (unit B)	0.95	1.9	0.39	2.03~2.12	0.13
34.73 Calico-Hidalgo dextral fault, CA	F4088	R	2.29~3.57	*Oskin et al.* [2007] (unit K)	1.5	2.2	0.09	2.03~2.12	0
34.71 Big Pine (Central), CA	F4192	T	0	*Onderdonk et al.* [2005]	0.33	4.1	0.33	0.391~0.521	0
34.50 San Andreas (Mojave S), CA	F4301	R	16.2~17.4	*Matmon et al.* [2005] (fan #5)	28	70	10.6	17.3~17.7	10.3
34.50 San Andreas (Mojave S), CA	F4301	R	16.2~17.4	*Matmon et al.* [2005] (fan #4)	21	U	3.6	17.3~17.7	3.3
34.50 San Andreas (Mojave S), CA	F4301	R	16.2~17.4	*Matmon et al.* [2005] (fan #3)	16	U	0	17.3~17.7	0
34.50 San Andreas (Mojave S), CA	F4301	R	16.2~17.4	*Matmon et al.* [2005] (fan #1)	43	83	25.6	17.3~17.7	25.3
34.50 San Andreas (Mojave S), CA	F4301	R	16.2~17.4	*Matmon et al.* [2005] (fan #0)	21	78	3.6	17.3~17.7	3.3
34.46 San Andreas (Mojave S), CA	F4301	R	16.2~17.4	*Sieh* [1984]	1.1	18	0	17.3~17.7	0
34.44 San Andreas (Mojave S), CA	F4301	R	16.2~17.4	*Weldon et al.* [2008]	5.9	36	0	17.3~17.7	0
34.44 San Andreas (Mojave S), CA	F4301	R	16.2~17.4	*Weldon et al.* [2008]	11	57	0	17.3~17.7	0
34.37 San Andreas (Mojave S), CA	F4301	R	16.2~17.4	*Weldon et al.* [2002]	15	43	0	17.3~17.7	0
34.30 North Frontal (East) thrust fault, CA	F4083	T	0.122~0.514	*Spotila & Sieh* [2000]	0.80	2.1	0.286	0.562~0.699	0.101
34.30 North Frontal (West) thrust fault, CA	F4082	T	0.193~0.319	*Spotila & Sieh* [2000]	0.80	2.1	0.481	0.556~0.569	0.231
34.19 San Andreas (San Bernardino N) fault, CA	F4282	R	18.9~20.6	*McGill et al.* [2008]	7.2	20	0	16.5~16.9	0
34.19 San Andreas (San Bernardino N) fault, CA	F4282	R	18.9~20.6	*McGill et al.* [2008]	13	18	0.9	16.5~16.9	0
34.12 San Andreas (San Bernardino S) fault, CA	F4283	R	11.6~15.4	*McGill et al.* [2008]	8.1	21.7	0	13.3~14	0
34.10 Hollywood thrust fault, CA	F4108	T	0.196~0.584	*Dolan et al.* [1997]	0.19	0.44	0	0.309~0.31	0
34.10 Hollywood thrust fault, CA	F4108	T	0.196~0.584	*Dolan et al.* [1997]	0.082	2.6	0	0.309~0.31	0
34.03 Santa Cruz Island sinistral fault, CA	F4111	L	0.597~1.93	*Pinter et al.* [1998]	0.64	1.3	0	0.859~0.914	0
34.03 Santa Cruz Island thrust fault, CA	F4111	T	1.07~1.6	*Pinter et al.* [1998]	0.079	0.57	0.5	0.921~1.29	0.351
34.00 Channel Islands thrust fault, offshore CA	F4129	P	-0.918~0.728	*Pinter et al.* [2003]	1.1	2.1	0.372	2.29~2.37	0.19
34.00 Channel Islands thrust fault, offshore CA	F4129	P	-0.918~0.728	*Chaytor et al.* [2008]	2.5	7.5	1.772	2.29~2.37	0.13
33.96 Puente Hills thrust (Los Angeles segment), CA	F4241	T	0.235~0.365	*Shaw et al.* [2002]	0.36	0.41	0	0.403	0
33.92 Puente Hills thrust (Santa Fe Springs seg.), CA	F4242	T	-0.124~0.005	*Shaw et al.* [2002]	0.26	0.30	0.255	0.521	0.221

33.92 Puente Hills thrust (Santa Fe Springs seg.), CA	F4242	T	-0.124~0.005	Dolan et al. [2003]	0.39	0.73	0.385	0.521	0
33.92 Puente Hills thrust (Santa Fe Springs seg.), CA	F4242	T	-0.124~0.005	*Myers et al.* [2003]	0.48	1.4	0.475	0.521	0
33.92 Puente Hills thrust (Santa Fe Springs seg.), CA	F4242	T	-0.124~0.005	*Myers et al.* [2003]	0.42	0.57	0.415	0.521	0
33.87 Puente Hills thrust (Coyote Hills seg.), CA	F4243	T	-0.062~0.143	*Shaw et al.* [2002]	0.56	0.63	0.417	0.567	0
33.87 Puente Hills thrust (Coyote Hills seg.), CA	F4243	T	-0.062~0.143	*Myers et al.* [2003]	0.48	1.4	0.337	0.567	0
33.87 Puente Hills thrust (Coyote Hills seg.), CA	F4243	T	-0.062~0.143	Myers et al. [2003]	0.36	0.50	0.217	0.567	0.067
33.85 Compton blind thrust fault, CA	F4184	P	0.847~1.562	*Dooling et al.* [2008]	1.8	29	0.238	1.14~1.87	0
33.85 Compton blind thrust fault, CA	F4184	P	0.847~1.562	*Dooling et al.* [2008]	1.3	2.7	0	1.14~1.87	0
33.79 San Andreas (Coachella) rev fault, CA	F4295	R	14.8~17.5	*Behr et al.* [2008]	12	21	0	17~17.9	0
32.90 Imperial dextral fault, CA	F4097	R	19.4~33.5	*Meltzner & Rockwell* [2008]	2.1	34	0	26.6~32.5	0
32.80 Elsinore (Coyote Mt.) dextral fault, CA	F4103	R	0.911~2.22	*Fletcher et al.* [2008]	0.30	1.9	0	1.46~1.5	0

.